UNCERTAINTY QUANTIFICATION FOR FREQUENCY STABILITY OF RENEWABLE PENETRATED POWER SYSTEMS

WANG ZHAOYUAN

PhD

The Hong Kong Polytechnic University

2025

The Hong Kong Polytechnic University

Department of Electrical and Electronic Engineering

Uncertainty Quantification for Frequency Stability of Renewable Penetrated Power Systems

Wang Zhaoyuan

A thesis submitted in partial fulfilment of the requirements for
the degree of Doctor of Philosophy

August 2024

CERTIFICATE OF ORIGINALITY

I hereby declare that this thesis is my own work and that, to the best of my knowledge and belief, it reproduces no material previously published or written, nor material that has been accepted for the award of any other degree or diploma, except where due acknowledgement has been made in the text.

____________________ (Signed)

____Wang Zhaoyuan____ (Name of student)

Abstract

In recent years, with the wide utilization of renewable energies, conventional power systems are undergoing the transformation into renewable penetrated power systems. However, the high penetration of renewable energy generations (RPGs) greatly threatens the frequency stability of modern power systems since the integration of RPGs introduces uncertainties into systems and decreases system inertia. Therefore, uncertainty quantification (UQ) methods for frequency stability of renewable penetrated power systems are urgently needed.

In this thesis, firstly, methods for probabilistic frequency stability analysis (PFSA) considering the dynamics of RPGs with different control strategies are proposed. Based on the system frequency response (SFR) model, the frequency response affected by different control strategies of RPGs is analyzed, which reveals the necessity of considering the dynamics of RPGs in PFSA. Moreover, a multi-interval sensitivity (MIS) method is proposed to reduce the simulation time of PFSA, thereby improving efficiency. And then, a multi-element low-rank approximation (MELRA) method is proposed to conduct uncertainty propagation analysis (UPA) while considering the frequency response characteristics, thereby increasing the accuracy of PFSA. Additionally, based on the Gaussian mixture model (GMM), the limitation of moment-based UPA methods is discussed by investigating the relationship between moments

and probability distributions of uncertainties.

Secondly, to tackle the heterogeneity and interactions of wind power generations (WPGs), i.e., wake effects (WEs) in wind farms (WFs), an analytical WE model suitable for PFSA is proposed, which considers multiple factors, including terrain, wind direction, and time delay of wind flow, and thus can reflect the WEs in WFs more realistically. Moreover, a multiple output Gaussian process regression (MOGPR) for PFSA considering the WEs in WFs is proposed, where the implicit relationship among system frequency response and area-level frequency responses is utilized so that the accuracy of PFSA is improved. Furthermore, the impact of terrain, wind direction, and WF layout on PFSA is investigated based on the proposed WE model and MOGPR.

Thirdly, to quantify the frequency response trajectory affected by uncertainties more efficiently, a generic multi-output polynomial chaos expansion (GMPCE) based on multi-task Elastic Net is proposed. GMPCE has multiple outputs, the sparse structure, and polynomial chaos bases suitable for independent uncertainties with arbitrary probability distributions. Thus, it is suitable for large-scale uncertainties, avoids the curse of dimensionality, and can quantify the system frequency response at each time point simultaneously. Also, a generic transformation method based on independent component analysis (ICA) is proposed, which can transform the uncertainties with complicated correlations into independent ones and thus broadens the application of proposed GMPCE.

Finally, to tackle slow timescale characterizations of uncertainties (STCUs) and fast timescale characterizations of uncertainties (FTCUs) simultaneously, the FTCU

transformation method based on Karhunen-Loève expansion (KLE) is proposed, which enables STCUs and FTCUs to be formulated by probability distribution methods in a unified form. Moreover, a scalable polynomial chaos expansion (PCE) method is proposed to improve the efficiency of UPA of power system frequency stability considering STCUs and FTCUs. And then, a comprehensive UQ framework based on the proposed FTCU transformation method and scalable PCE is proposed, where frequency stability indices, frequency response trajectories, and the sensitivity between stability indices and uncertainties are quantified. These results will provide constructive guidance for system operators to ensure the frequency stability of renewable penetrated power systems.

List of Publications

Journal Papers

1. **Z. Wang**, S. Bu, Z. Qi, C. K. Hung, C. Y. Chung, "Comprehensive Uncertainty Quantification for Renewable Penetrated Power System Dynamics Considering Different Timescale Characterizations of Uncertainties," *Energy*. (Under review)
2. **Z. Wang**, S. Bu, J. Wen, C. Huang, "Uncertainty Modeling in Modern Power Systems: A Review," *International Journal of Electrical Power and Energy Systems*. (Accepted)
3. **Z. Wang**, S. Bu, "Probabilistic Frequency Stability Analysis Considering Dynamics of Wind Power Generation with Different Control Strategies," *IEEE Transactions on Power Systems*, vol. 39, no. 5, pp. 6412-6425, Sept. 2024.
4. **Z. Wang**, S. Bu, "Probabilistic Analysis of Small-Signal Stability of Power Systems Affected by Wind Power Generation Uncertainty Considering Wake Effect," *IEEE Transactions on Power Systems*, vol. 40, no. 2, pp. 1955-1968, Mar. 2025.
5. **Z. Wang**, S. Bu, "Probabilistic Analysis of Power System Frequency Stability Considering Wake Effects of Wind Farms," *IEEE Transactions on Power Systems*, 2025, Early access.

6. **Z. Wang**, S. Bu, "Generic Multi-Output Spectral Representation Method for Uncertainty Propagation Analysis of Power System Dynamics," *Journal of Modern Power Systems and Clean Energy*, 2025, Early access.
7. **Z. Wang**, S. Bu, "Design and Defense of Modal Resonance-Oriented Cyber-Attack Against Wide-Area Damping Control," *IEEE Transactions on Smart Grid*, vol. 15, no. 2, pp. 2164-2178, Mar. 2024.
8. D. Wang, Z. Guan, J. Tian, C. Mao, Y. Yang, and **Z. Wang**, "A Hybrid Redundancy Scheme for Medium-Voltage Three-Phase Cascaded H-Bridge Electronic Power Transformer," *IET Power Electronics*, vol. 15, no. 9, pp. 841-854, Jul. 2022.
9. I. Zografopoulos, A. Srivastava, C. Konstantinou, J. Zhao, A. A. Jahromi, A. Chawla, B. Nguyen, S. Bu, C. Li, F. Teng, G. Preetham, J. Ospina, M. A. Aftab, M. Arani, O. Sen, P. Moutis, P. Ge, Q. Guo, S. Sahoo, S. Lakshminarayana, T. Vu, and **Z. Wang**, "Cyber-Physical Interdependence for Power System Operation and Control," *IEEE Transactions on Smart Grid*, 2025, Early access.

Conference Papers

1. **Z. Wang**, S. Bu, "Probabilistic Analysis of Converter-Driven Stability of Power Systems Based on Generalized Polynomial Chaos Expansion," in *IEEE Power & Energy Society General Meeting*, Seattle, WA, USA, 2024.
2. **Z. Wang**, S. Bu, "Design and Analysis of Modal Resonance-Oriented Cyber-Attack Against Wide-Area Damping Control," in *The 12th IET International*

Conference on Advances in Power System Control, Operation and Management, Hong Kong, China, 2022, pp. 164-169.

3. **Z. Wang**, S. Bu, R. Wang, X. Zhou, “Data-Driven Defense Strategy of Modal Resonance-Oriented Cyber-Attack Against Wide-Area Damping Control,” in *IEEE Power & Energy Society General Meeting*, 2025. (Under review)
4. Z. Hu, **Z. Wang**, Z. Zhu, Z. Li, S. Bu, and K. W. Chan, “Dispatch of Virtual Inertia and Damping via Deep Reinforcement Learning for Improving System Frequency Stability,” in *IEEE Power & Energy Society General Meeting*, Seattle, WA, USA, 2024.

Technical Report

1. A. A. Jahromi, A. Srivastava, A. Chawla, B. Nguyen, B. Tan, S. Bu, C. Li, C. Konstantinou, F. Teng, G. Preetham, I. Zografopoulos, J. Ospina, J. Zhao, L. Vu, L. Xu, M. A. Aftab, M. Arani, Ö. Sen, P. Moutis, P. Ge, Q. Guo, S. Sahoo, S. Lakshminarayana, S. Rath, T. Vu, W. Zhu, and **Z. Wang**, “Cyber-Physical Interdependence for Power System Operation and Control,” IEEE PES, Piscataway, NJ, USA, Rep. PES-TR119, 2023.

Acknowledgements

As time goes by, my PhD period is nearing the end. Looking back the past three years at The Hong Kong Polytechnic University, I really appreciate every person in my life.

First of all, I would like to express the sincerest appreciation to my supervisor, Dr. Siqi Bu. I am greatly grateful to him for providing me with an opportunity to study at The Hong Kong Polytechnic University. Every achievement of my research in my PhD period is inseparable from his patient guidance, encouragement, and support. And his broad knowledge and personality really motivate me.

Meanwhile, I would like to thank every member in Dr. Bu's research group: Dr. Jianqiang Luo, Dr. Qian Hu, Dr. Jiaxin Wen, Dr. Yong Hu, Mr. Ruoheng Wang, Ms. Jiangfeng Zhang, Ms. Chaoyun Wang, Mr. Chao Huang, Ms. Xianyu Zhou, Mr. Chao Lei, Mr. Qifan Chen, Mr. Runzhuo Ma, Mr. Yitao Cheng, Ms. Meng Liu, for the help in both research and daily life. Wish them a bright future.

Moreover, I would like to appreciate my families. Their selfless and consistent support is my biggest motivation. Also, I am very grateful to my friends. Their companionship significantly encourages me.

Last but not least, I would like to thank The Hong Kong Polytechnic University. Our school provides a wonderful environment and sufficient funding support, which ensures that I can concentrate on my research. Also, I would like to appreciate the State Grid Jiangsu Electric Power Company in China for the kindly support. Additionally, I am very grateful to the reviewers, whose comments are helpful and greatly improve the thesis quality.

Table of Contents

List of Figures, Tables, and Abbreviations

List of Figures

List of Tables

List of Abbreviations

AE	Absolute error
AGC	Automatic generation control
ANOVA	Analysis of variance
CBM	Cumulant-based method
CFD	Computational fluid dynamics
CGCE	Cumulant-based Gram-Charlier expansion
FN	Frequency nadir
FSI	First-Order sensitivity index
FTCU	Fast timescale characterization of uncertainty
FV	Frequency vertex
GMM	Gaussian mixed model
GMPCE	Generic multi-output polynomial chaos expansion
GP	Gaussian process
GPR	Gaussian process regression
GSA	Global sensitivity analysis
GSC	Grid side converter
ICA	Independent component analysis
KDE	Kernel density estimation
KLE	Karhunen-Loève expansion
LAR	Least angle regression
LHS	Latin hypercube sampling
LOO	Leave-One-Out
LRA	Low-rank approximation
LSA	Local sensitivity analysis
MAE	Mean absolute error
MAPE	Mean absolute percentage error
MCS	Monte Carlo simulation

MELRA	Multi-Element low-rank approximation
MIS	Multi-Interval sensitivity
MLR	Multiple linear regression
MOGPR	Multiple output Gaussian process regression
MPPT	Maximum power point tracking
MSC	Machine side converter
PCE	Polynomial chaos expansion
PDF	Probability density function
PEM	Point estimation method
PFSA	Probabilistic frequency stability analysis
PMSG	Permanent magnet synchronous generator
PV	Photovoltaic
QMCS	Quasi Monte Carlo simulation
RAM	Risk assessment matrix
RoCoF	Rate of change of frequency
RMSE	Root-Mean square error
RPG	Renewable power generation
SDE	Stochastic differential equation
SFR	System frequency response
SG	Synchronous generator
STCU	Slow timescale characterization of uncertainty
Std.	Standard deviation
UPA	Uncertainty propagation analysis
UQ	Uncertainty quantification
VSG	Virtual synchronous generator
WE	Wake effect
WF	Wind farm
WPG	Wind power generation
WS	Worst scenario

WT	Wind turbine

Chapter 1 Introduction

1.1 Background

In recent years, sustainable development and environmental protection have been concerned worldwide. Many countries have issued relevant policies to promote renewable energies [1]. For example, in 2019, Britain promised to develop a power system with zero or nearly zero carbon dioxide emission in 2035 by legislation [2]. In 2021, China promised to achieve peak carbon dioxide emission in 2030 and carbon neutrality in 2060 in the report on the work of the government [3]. Fig. 1.1 shows countries with policies for promoting renewable power generations (RPGs) and restricting the utilization of fossil fuels.

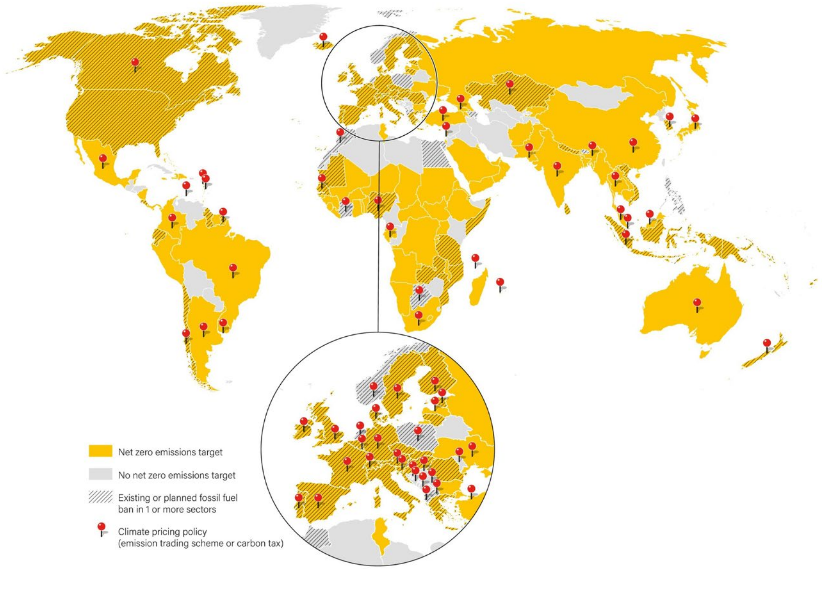

Fig. 1.1 Countries with climate change policies by 2022 [4].

Meanwhile, with the growth of power demand, the utilization of RPGs in power systems has developed rapidly. Since 2014, the increased installed generation capacity of wind power and photovoltaic (PV) in the world has exceeded that of fossil fuels. It is expected that in 2025, RPGs will be the largest source of power generation. And in 2028, RPGs are expected to account for over 42% of global power generation. The share growth of RPGs from 2000 to 2028 is presented in Fig. 1.2. Therefore, the traditional power systems are undergoing a tremendous transformation into modern power systems with high penetration of RPGs.

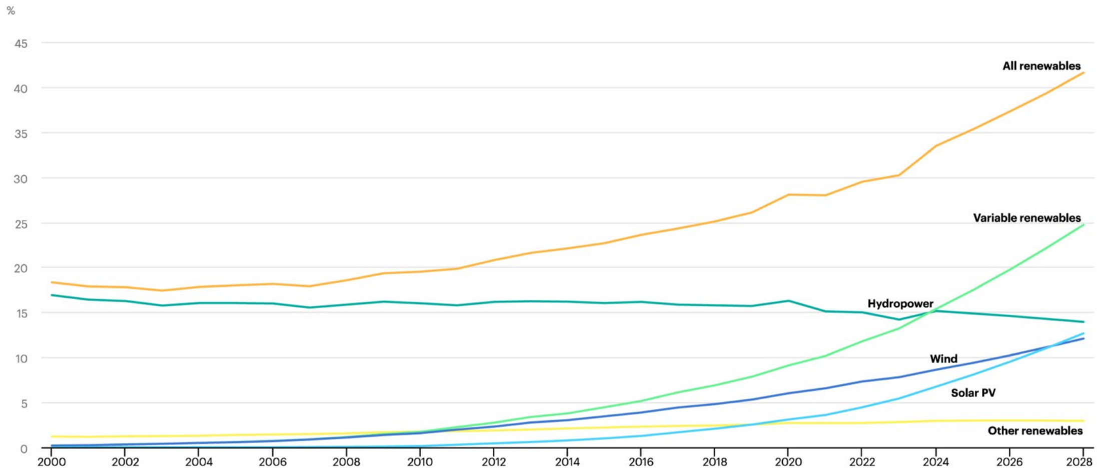

Fig. 1.2 RPG share from 2000 to 2028 [5].

However, the utilization of RPGs is a double-edged sword for modern power systems. On the one hand, it accelerates the decarbonization of power systems. On the other hand, it poses a huge threat to system stability, including frequency stability [6]. In the research area of power system stability, frequency stability refers to the ability of power systems to maintain the frequency, i.e., synchronism, and mitigate the frequency deviation [7, 8]. Hence, the frequency response, including the rate of change of frequency (RoCoF) and the frequency nadir/vertex (FN/FV), are the main frequency stability indices [7, 9]. Also, RPGs dominated by wind power generations (WPGs) and PVs have the characteristics of intermittent and fluctuation due to the change of weather conditions. After a large quantity of RPGs is integrated into power systems, numerous uncertainties will be injected into systems, which will cause the power imbalance between the power generation and power demand, thereby contributing to the fluctuation of frequency and the degradation of frequency stability [7]. One of the most serious frequency stability incidents induced by RPGs happened in London in 2019. The sudden generation reduction of wind power caused by extreme weather contributes to the outage of approximately 1 million customers [10]. Moreover, RPGs with conventional control schemes do not provide any inertia or frequency response like traditional synchronous generators, and their integration has significantly reduced the power system inertia, thereby further degrading the frequency stability [11].

In light of the randomness and low inertia caused by the integration of PRGs into power systems, developing effective methods to quantify the impact of RPG uncertainties is an essential task to ensure the frequency stability of power systems, which is worthy of investigation.

1.2 Literature Review

In terms of uncertainty quantification (UQ) for power system stability, two timescale characterizations of uncertainties are typically concerned: 1) slow timescale characterization of uncertainty (STCU), and 2) fast timescale characterization of uncertainty (FTCU). STCUs mainly focus on the uncertainty sources varying slowly and infrequently with time, and the fast time-varying properties of them are usually ignored to reduce computational complexity. Thus, they are characterized as the randomness of steady-state operating points. By comparison, FTCUs focus on fast time-varying properties of uncertainty sources varying rapidly and frequently during the concerned time period. Moreover, the comprehensive UQ usually contains three tasks: 1) uncertainty modeling, i.e., characterizing the randomness or fluctuation of uncertainties; 2) uncertainty propagation analysis (UPA), i.e., quantifying the relationship between uncertainties and concerned system outputs; 3) uncertainty sensitivity analysis, i.e., identifying the uncertainties significantly affecting concerned system outputs. In the following, existing studies on UQ for power system stability are summarized according to different timescale characterizations of uncertainties, including studies on different UQ tasks.

1.2.1 Uncertainty Quantification for Power System Stability with Slow Timescale Characterization of Uncertainty

Regarding the modeling of STCU of RPGs, different models have been proposed. These models characterize the relationship between the output power of RPGs and weather conditions, e.g., wind speed and solar irradiance. And the uncertainties of weather conditions are described by different probability distributions or historical data. Since there are various types of probability distribution functions with simple forms, probability distribution methods are widely applied in power system stability to model the possible values of uncertainties at the specific time point [6, 7]. And power system stability considering STCUs is commonly called probabilistic power system stability. To further improve the precision of probability distribution methods in modeling uncertainties, the Gaussian mixed model (GMM) [12, 13] and kernel density estimation (KDE) [14] are proposed to model uncertainties with complex probability distributions, especially when probability density functions (PDFs) have multiple peaks. Furthermore, to characterize uncertainties with spatial correlations, the Copula functions are proposed [15]. Additionally, to adequately characterize the uncertainties in specific scenarios, some empirical PDFs are developed. Typical PDF developing methods include forming a versatile PDF [16] and introducing the truncated interval [17].

Models characterizing the relationship between RPG outputs and weather conditions can be summarized as two types, i.e., simplified RPG models and detailed RPG models. The simplified RPG models usually utilize the simplified maximum power point tracking (MPPT) functions to calculate the RPG outputs under different weather conditions [18]. Since the calculation complexity is significantly reduced, these simplified RPG models are widely adopted in the probabilistic power flow [19], economical operation [20], and probabilistic stability analysis [6, 7, 21-26]. For probabilistic power flow and economical operation, applying the simplified RPG models is relevantly reasonable since these issues commonly focus on the steady state of power systems. However, for probabilistic stability analysis, the above models are oversimplified since the dynamics of RPGs are ignored. Although some researchers have tried to use detailed RPG models in probabilistic stability analysis [27-29], the studies have focused on small-signal stability and voltage stability issues rather than frequency stability. Moreover, apart from the conventional grid-following control strategy [30-33], to mitigate the negative impact of low inertia on system stability caused by the large-scale integration of RPGs, control strategies providing inertia have been proposed, such as virtual synchronous generator (VSG) [34-45], which is also treated as a type of grid-forming control strategies. Since different control strategies of RPGs have distinct dynamics and provide diverse inertia, the impacts on frequency stability are different, which is worthy of being investigated.

Additionally, some RPGs have their unique characteristics. For example, in a wind farm (WF), wind turbines (WTs) at the wind downstream position are affected by the wake of upstream WTs, resulting in the deficit of downstream wind speed, i.e., wake effects (WEs). However, existing studies on probabilistic frequency stability affected by WPG uncertainties ignore the WEs of WFs. Thus, it is worth investigating whether this model simplification is reasonable and whether it will contribute to the inaccurate results of probabilistic frequency stability analysis (PFSA). Moreover, to characterize the WEs of WFs, different models have been proposed, which can be mainly divided into numerical WE models and analytical WE models. Numerical WE models are based on computational fluid dynamics (CFD) [46-48], the results of which usually have high accuracy. However, the computation of these models costs an enormous amount of time, which are not suitable for probabilistic stability analysis. By comparison, the significant merit of analytical WE models is that the computational time is quite limited. Among the analytical WE models widely applied, the Jensen WE model is based on the principle of conservation of mass [49-51], while the Frandsen WE model is based on the principle of conservation of mass and momentum [52]. However, these two WE models assume that the wind speed at the same streamwise section in the wake region is identical, which is not in line with actual WEs. To overcome the above shortcoming, the Gaussian WE model is proposed, where the Gaussian shape is applied to depict the wind speed deficit [53]. Also, some improved analytical WE models have been proposed to consider the impact of different factors on WEs, including the wind direction [54-58], single complex terrain [54, 59], and the time delay of wind flow [60]. However, these existing studies only consider the above factors partly rather than entirely and only consider one type of complex terrain rather than multiple types. Moreover, most of the existing analytical WE models considering different factors are based on the Jensen WE model [50, 54-59], the accuracy of which is limited. Thus, a WE model suitable for PFSA and comprehensively considering the multiple factors affecting the WEs of WFs with high accuracy is required.

Regarding UPA, many review papers have summarized the typical methods [7, 61-76]. For UPA methods suitable for STCUs, they can be classified as numerical methods, analytical methods, and approximation methods. Among the numerical UPA methods, Monte Carlo simulation (MCS) is one of the representative methods [18], the results of which are commonly treated as the baseline of other methods. Moreover, improved MCS methods have been proposed for different purposes, for example, sequential MCS suitable for chronological data [77], Markov Chain MCS and quasi MCS (QMCS) aiming at improving the sampling efficiency [7]. Also, other numerical methods, represented by Latin hypercube sampling (LHS) [78], have been proposed to improve the sampling efficiency. However, at least thousands of sampling data are required for numerical methods, which indicates their time-consuming characteristic.

By comparison, analytical UPA methods significantly reduce the computation time. In analytical UPA methods, convolution methods can only handle the independent uncertainties, unscented transformation can only derive the mean and variance of the concerned system outputs, and Taylor series expansion requires the derivative operation with respect to concerned system outputs, which leads to the limited application of these methods in power systems [61, 79]. By comparison, moment-based methods, including point estimation methods (PEMs) and cumulant-based methods (CBMs), are relatively widely applied in probabilistic stability analysis of power systems, including transient stability [7], small-signal stability [27-29, 80-82], voltage stability [83], and frequency stability [21]. Both of them adopt the moments of uncertainties to obtain those of concerned system outputs and utilize series expansion to calculate the PDFs. The differences are that PEMs adopt central moments, while CBMs adopt cumulants, and the required sampling data of CBMs are usually less than those of PEMs [84]. However, CBMs are effective only when there is an approximately proportional relationship between concerned system outputs and uncertainties. Whether the above relationship between frequency stability indices and uncertainties of RPGs exists when considering the dynamics of RPGs requires to be studied. Also, according to the forms of series expansion, uncertainties with close moments should have similar shapes of PDFs.

However, it should be discussed whether there are situations violating the above relationship, which may affect the calculation accuracy of stability analysis. Thus, the effectiveness of conventional CBMs in analyzing frequency stability considering the dynamics of RPGs is undetermined and should be investigated.

Recently, the emerging approximation UPA methods have found a balance between efficiency and accuracy, which are the focused methods and mainly include polynomial chaos expansion (PCE) methods, low-rank approximation (LRA) methods, and Gaussian process regression (GPR) methods. PCE is formed by the superposition of orthogonal polynomials related to probability distributions of uncertainties, which has been widely applied in power flow [85-96] and adopted in voltage stability [14] and transient stability [97-99] recently. However, the relationship between the number of undetermined coefficients and that of uncertainties is factorial, leading to the curse of dimensionality when considering numerous uncertainties. Apart from PCE, LRA is also based on orthogonal polynomials. The relationship between the number of undetermined coefficients and that of uncertainties is linear [100], indicating that LRA is suitable for large-scale UPA. Some researchers have used LRA in probabilistic power flow [101, 102]. However, to the best of our knowledge, there has been no attempt to use LRA in PFSA. Additionally, the explicit correlation expression of uncertainties is required for PCE and LRA, as well as analytical UPA methods, and the complicated correlations of realistic data of RPG uncertainties and WEs cannot be characterized as expected. Thus, they are not suitable for probabilistic stability analysis considering complicated correlations. By comparison, GPR only requires sampling points of uncertainties, which has been applied in voltage stability [78] and transient stability [103]. However, to the best of our knowledge, there has been no attempt at PFSA by applying GPR. Moreover, approximation UPA methods in the existing studies are generic frameworks, which means the accuracy of specific issues is reduced due to the ignorance of the characteristics of concerned outputs. Thus, it is necessary to consider the frequency characteristics when designing the UPA method for the PFSA. Also, both the system frequency and area-level frequency are concerned in PFSA, and there is an implicit relationship among the system and area-level frequency responses. However, existing approximation UPA methods can only analyze the probabilistic stability of system and area-level frequency responses individually, the implicit relationship will be overlooked. Therefore, to improve analysis accuracy, UPA methods considering the relationship among the frequency responses is required. Furthermore, existing approximation UPA methods only have one output, which means that if system response trajectories are needed to be quantified, they can only quantify the system response at each time point separately. This indicates that the number of constructed UPA models equals the concerned system response duration divided by the step length, which is cumbersome and time-consuming. Thus, UPA methods with multiple outputs are needed to improve efficiency. Additionally, recently, neural networks have been applied to conduct UPA. In [104], gated recurrent units are used to analyze the transient stability affected by trip uncertainties. Authors in [105] have proposed a multi-stability analysis method based on graph neural networks for power systems affected by WPG and trip uncertainties. In [106], the graph neural network and the physics-informed neural network are combined to analyze the transient stability affected by WPG and trip uncertainties. And authors in [107] have combined the physics-informed neural network and the deep Koopman operator to investigate the transient stability. However, though neural network-based methods can tackle complicated issues, the training of them requires massive simulations and thus is time-consuming.

Regarding the STCU sensitivity analysis methods, they can be classified as local sensitivity analysis (LSA) methods and global sensitivity analysis (GSA) methods. LSA methods are only valid for a small region of variations and thus have limited applications [108]. By comparison, GSA methods analyze the impact of uncertainties in a full region of variations and consider the nonlinear relation, which is receiving increasing concerns. In [109], the factors of voltage stability are investigated based on GSA under the framework of analysis of variance (ANOVA). Besides, authors in [15] have studied the voltage and transient stability affected by RPG uncertainties based on GSA. However, GSA usually requires results for MCS-based UPA methods, which indicates it is time-consuming. To improve the efficiency of uncertainty sensitivity analysis, approximation UPA methods have been adopted in GSA, which significantly reduce the calculation time [110, 111]. Additionally, in probabilistic stability analysis, the stability indices, system response trajectories, and the sensitivity between stability indices and uncertainties play different roles. Specifically, stability indices indicate the instability probability of systems, system response trajectories describe system states at different time points, and the sensitivity between stability indices and uncertainties identifies the uncertainties significantly affecting the system stability. However, there has been no comprehensive framework for power system stability affected by uncertainties containing all the indices mentioned above.

1.2.2 Uncertainty Quantification for Power System Stability with Fast Timescale Characterization of Uncertainty

Regarding the modeling of FTCU, FTCUs are usually formulated as stochastic processes, and thus power system stability affected by FTCUs is usually called stochastic power system stability. Continuous FTCUs are usually characterized by the continuous Wiener process [112, 113]. And discrete FTCUs are typically modeled as the jumping compound Poisson process [114]. Since the dynamic response of the power system is normally modeled as the differential equations, after FTCUs modeled by stochastic processes are introduced, the differential equations of power systems will transform into stochastic differential equations (SDEs) [115]. Authors in [116] have proposed a systematic method for modeling stochastic power systems with SDEs. Power systems affected by FTCUs of loads and RPGs are formulated by SDEs in [117]. In [118], the FTCUs of transmission lines and loads are considered, and power systems under these FTCUs are formulated as SDEs. In [119], SDEs are used to model power systems with FTCUs of WPGs. Authors in [120] have adopted SDEs to model power systems with FTCUs of loads and WPGs. Moreover, apart from the research area of stochastic stability analysis of power systems affected by FTCUs of loads and WPGs, SDEs are also used in the modeling of power systems affected by FTCUs of PVs and electricity prices for investigating optimal control [121-123] and optimal market participation [124].

Regarding dynamic UPA methods, one of the most common methods is MCS, where a large number of simulations are conducted to obtain system responses [125, 126]. Some studies conduct UPA by analyzing the mean value and variance of state variables in the system differential equations [112, 127]. In [113], the stochastic stability is analyzed by calculating the mean value of the small-signal stability indices. Authors in [99] have applied the PCE to quantify the relationship between FTCUs and transient stability indices. However, the proposed method in [99] is only applicable to continuous stochastic processes modeled by the Wiener process and is not applicable to discrete FTCUs. Thus, time-saving dynamic UPA methods for stochastic stability of power systems are lacking. Also, there is a lack of uncertainty sensitivity analysis methods for FTCUs.

Moreover, the specific choice of the timescale characterization of uncertainties is based on focused tasks and nature of uncertainty sources. Only using STCUs to model uncertainties will completely ignore the fast time-varying properties of some uncertainties, resulting in inaccurate UPA results. And only adopting FTCUs will increase unnecessary computational costs due to their complicated forms, thereby decreasing UPA efficiency. However, since STCUs and FTCUs are based on different methods and have different forms, general models suitable for STCUs and FTCUs are required to conduct UQ. Additionally, apart from the time-consuming MCS, no UPA methods are suitable for simultaneously investigating STCUs and FTCUs. Although authors in [99] have attempted to use the approximation UPA method to deal with

FTCUs, which greatly reduces the time cost and has the potential to be extended to deal with STCUs and FTCUs, the proposed method is only suitable for one type of FTCUs and thus not generic. Thus, the time-saving UPA method can tackle STCUs and FTCUs is needed. And since the outputs of UPA methods are the inputs of uncertainty sensitivity analysis methods, they need to match with each other. Therefore, effective uncertainty sensitivity analysis methods suitable for STCUs and FTCUs are also lacking.

1.2.3 Limitation Summary of Existing Studies on Uncertainty Quantification for Frequency Stability of Power Systems

In view of the aforementioned background, the limitations of existing studies on UQ methods for frequency stability of renewable penetrated power systems can be summarized as follows, which are the major foci and also the issues to be tackled in this thesis.

1) RPGs are usually simplified in UQ of PFSA, where different control strategies and dynamics are ignored. The rationality of simplification should be discussed, and the impact of different control strategies on probabilistic frequency stability needs to be investigated.

2) There is a lack of UQ methods for frequency stability with a balance between accuracy and efficiency.

3) Time-saving UQ methods for frequency stability suitable for large-scale uncertainties are lacking.

4) Existing UQ methods for probabilistic stability are too generic, which means that frequency characteristics are not utilized in the methods, and thus the accuracy of them is limited.

5) The heterogeneity and interactions of RPG uncertainties are ignored in existing studies for UQ of PFSA, which will contribute to inaccurate UQ results.

6) Existing approximation UQ methods for probabilistic stability ignore the relationship among multiple concerned stability indices and thus have limited accuracy.

7). There is a lack of approximation UQ methods for probabilistic stability with multi-output structure to improve UQ efficiency.

8) Existing time-saving UQ methods for frequency stability cannot tackle uncertainties with complicated correlations.

9) STCUs and FTCUs may be simultaneously used in UQ of power system frequency stability. However, they cannot be simultaneously dealt with by existing methods effectively.

10) Stability indices, system response trajectories, and the sensitivity between stability indices and uncertainties are all concerned in UQ. However, existing UQ methods for frequency stability do not consider them comprehensively.

1.3 Primary Contributions

Considering the limitations of existing studies summarized in Chapter 1.2.3, this thesis proposes a series of UQ methods for power system frequency stability, the contributions of which are summarized as follows.

1) Considering Limitation 1, the necessity of considering the dynamics of RPGs in PFSA is revealed by investigating the differences between considering and ignoring the dynamics of RPGs with different control strategies, i.e., the conventional grid-following control and VSG-based grid-forming control. The main difference is that the existence of RPG dynamics leads to the unfixed occurrence time of frequency stability indices, which increases the difficulty in analyzing frequency stability. (In Chapter 2)

2) Considering Limitation 2, 3, and 4, a multi-interval sensitivity (MIS) method for calculating frequency response is proposed, which greatly reduces the calculation time and can be applied to calculate both the system frequency and the area-level frequency. Moreover, a multi-element LRA (MELRA) method is proposed for UPA, which has quite a few outstanding advantages: (1) It considers different types of frequency response trends, thereby improving the analysis accuracy for the LRA-based methods; (2) The construction of polynomial bases in MELRA is suitable for arbitrary distributions unlike other LRA-based methods; (3) Compared with PCE, as another orthogonal polynomial-based method, the number of unknown coefficients of the proposed method has a linear relationship with the number of uncertainties, rather than a factorial relationship, so that it is more suitable for large-scale UPA. (In Chapter 2)

3) Considering Limitation 5, the necessity of considering the WEs of WFs in PFSA is revealed based on the proposed WE model, which is ignored in the existing studies. This model possesses many merits: (1) It only brings a slight increase in terms of the computational time in PFSA; (2) Based on the Gaussian WE model, it comprehensively

considers multiple types of terrain, the wind direction, and the time delay of wind flow, which can be applied to study the impact of different factors on probabilistic frequency stability; (3) It can be easily integrated into the frequency response models of power systems ignoring WEs without any modifications. Thus, it is very suitable for PFSA and realistically reflects the WEs in WFs. (In Chapter 3)

4) Considering Limitation 2, 3, and 6, a multiple output GPR (MOGPR) is proposed to analyze the probabilistic stability of system frequency and area-level frequency simultaneously and consider the relationship among them, which improves the analysis accuracy and efficiency. Furthermore, since GPR-based methods only require the sampling points of uncertainties, both MOGPR and GPR are suitable for the correlation caused by WEs. (In Chapter 3)

5) Considering Limitation 2, 3, 7, and 8, a generic multi-output PCE (GMPCE) is proposed to deal with correlated uncertainties that cannot be accurately characterized by standard PDFs and to quantify the system frequency response at each time point simultaneously. Moreover, the proposed GMPCE has other merits, including being applicable to independent uncertainties with arbitrary probability distributions and having sparse structure, thereby avoiding the curse of dimensionality. (In Chapter 4)

6) Considering Limitation 9, FTCUs formulated by stochastic processes are innovatively approximated by the superposition of a finite number of STCUs formulated by probability distribution methods, which clearly reveals the relationship between STCUs and FTCUs and effectively transforms STCUs and FTCUs into a general form by only using probability distribution methods. (In Chapter 5)

7) Considering Limitation 2, 3, 9, and 10, a generic UQ method is proposed based on the developed scalable PCE, which comprehensively integrates the modeling of STCU and FTCU, UPA, and sensitivity analysis in a time-saving and effective manner and analyzes stability indices, system response trajectories, and the sensitivity between stability indices and uncertainties. In the scalable PCE, the construction of polynomial chaos basis of uncertainties is based on the properties of orthogonal polynomials and thus suitable for arbitrary PDFs. Moreover, sparse methods are applied to avoid the curse of dimensionality. (In Chapter 5)

1.4 Thesis Layout

This thesis consists of six chapters. The remaining chapters are organized as follows.

Chapter 2-Chapter 4 focus on frequency stability affected by STCUs, i.e., PFSA. Specifically, in Chapter 2, the necessity of considering the dynamics of RPGs with different control strategies in PFSA is discussed. Moreover, the time-saving MIS method for calculating the system and area-level frequency responses is proposed. And the MELRA method is proposed to improve the accuracy of PFSA considering the dynamics of RPGs.

Chapter 3 proposes a WE model of WF considering multiple factors to improve the accuracy of uncertainty modeling. Also, MOGPR for PFSA is proposed to improve accuracy and efficiency, which considers the relationship among stability indices of the system and area-level frequency responses.

Chapter 4 proposes a generic uncertainty transformation method, which can tackle uncertainties with complicated correlations. Meanwhile, GMPCE is designed to improve the efficiency in quantifying the system frequency response trajectories affected by uncertainties.

Chapter 5 focuses on the frequency stability affected by STCUs and FTCUs. A comprehensive UQ framework is proposed, where STCUs and FTCUs are formulated and transformed in a generic form. And the frequency stability indices, frequency response trajectories, and the sensitivity between frequency stability indices are quantified based on the proposed scalable PCE in a time-saving manner.

Chapter 6 draws conclusions and makes suggestions for future research.

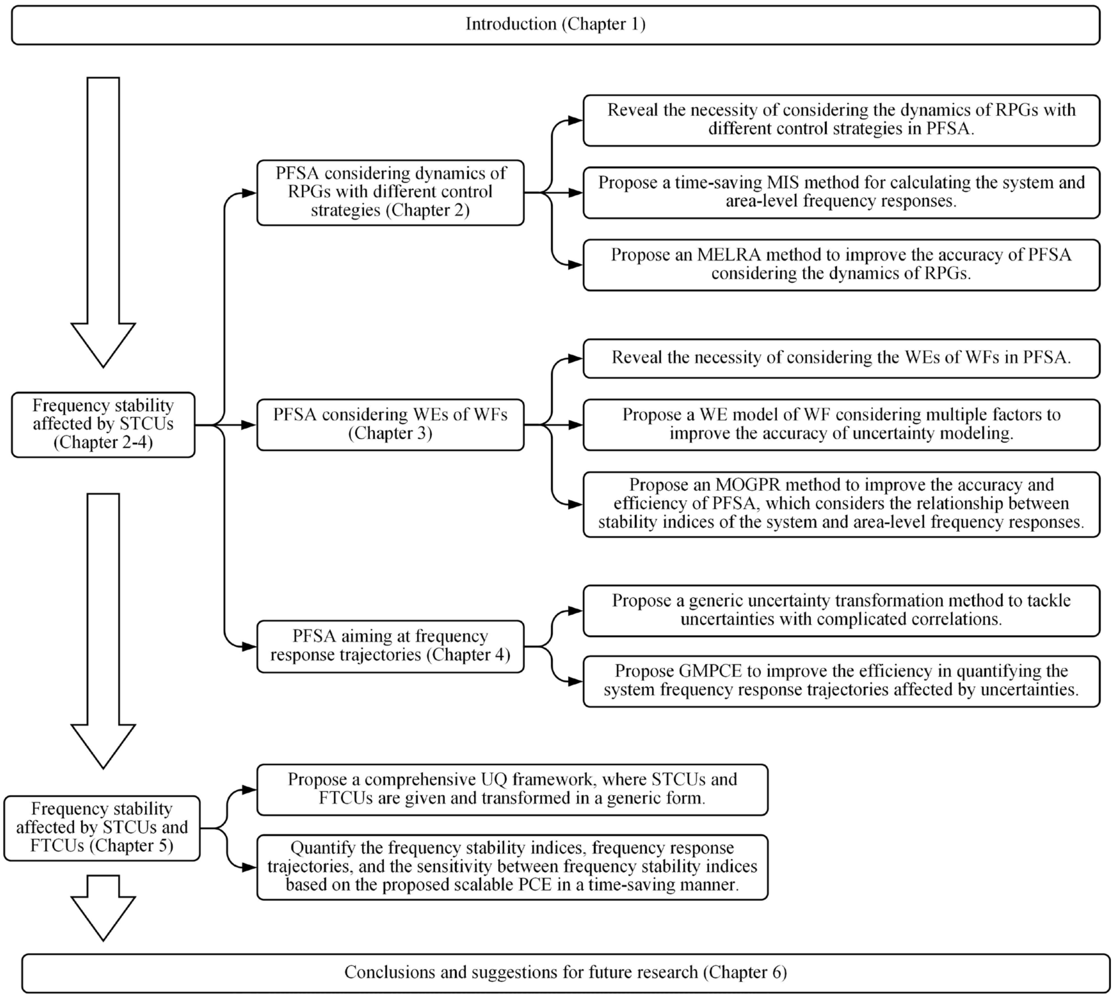

Fig. 1.3 Illustration of thesis layout.

Chapter 2 Probabilistic Frequency Stability Analysis Considering Dynamics of Renewable Power Generations with Different Control Strategies

2.1 Introduction

As stated in Chapter 1.2.3, most existing studies on PFSA ignore the dynamics of RPGs and thus result in inaccurate analysis results, especially when the fast frequency response of RPGs is expected. To overcome this limitation, this chapter proposes PFSA methods that consider the dynamics of RPGs with different control strategies. The proposed methods include MIS and MELRA for saving the simulation time and improving the accuracy. Also, the limitations of moment-based UPA methods are analyzed.

2.2 Multi-Interval Sensitivity for Frequency Response Considering Dynamics of Renewable Power Generations with Different Control Strategies

2.2.1 Control Strategies of Wind Power Generations

In this chapter, WPGs are selected as the example RPGs. Two typical control strategies of WPGs are considered in this chapter, including the conventional grid-following control [32] and VSG-based grid-forming control [39], as examples. The grid-following control strategy makes the phase angle of the bus connecting the WPG follow the phase angle of the external grid voltage through a phase-locked loop and controls the output current. By comparison, the grid-forming control strategy controls the voltage of the bus connecting the WPG and contributes to the forming of a voltage-source grid [128]. However, the following proposed method is not limited to the example control strategies and uncertainties of WPGs. Commonly, power electronic-interfaced WPG consists of three parts: the permanent magnet synchronous generator (PMSG), the machine side converter (MSC), and the grid side converter (GSC) [39, 129], which is illustrated in Fig. 2.1. It should be noted that only the control strategy of converters is considered in converter modeling. And phenomena related to electromagnetic transient are ignored to reduce the computational complexity since the timescale concerned in frequency stability is different from that concerned in electromagnetic transient.

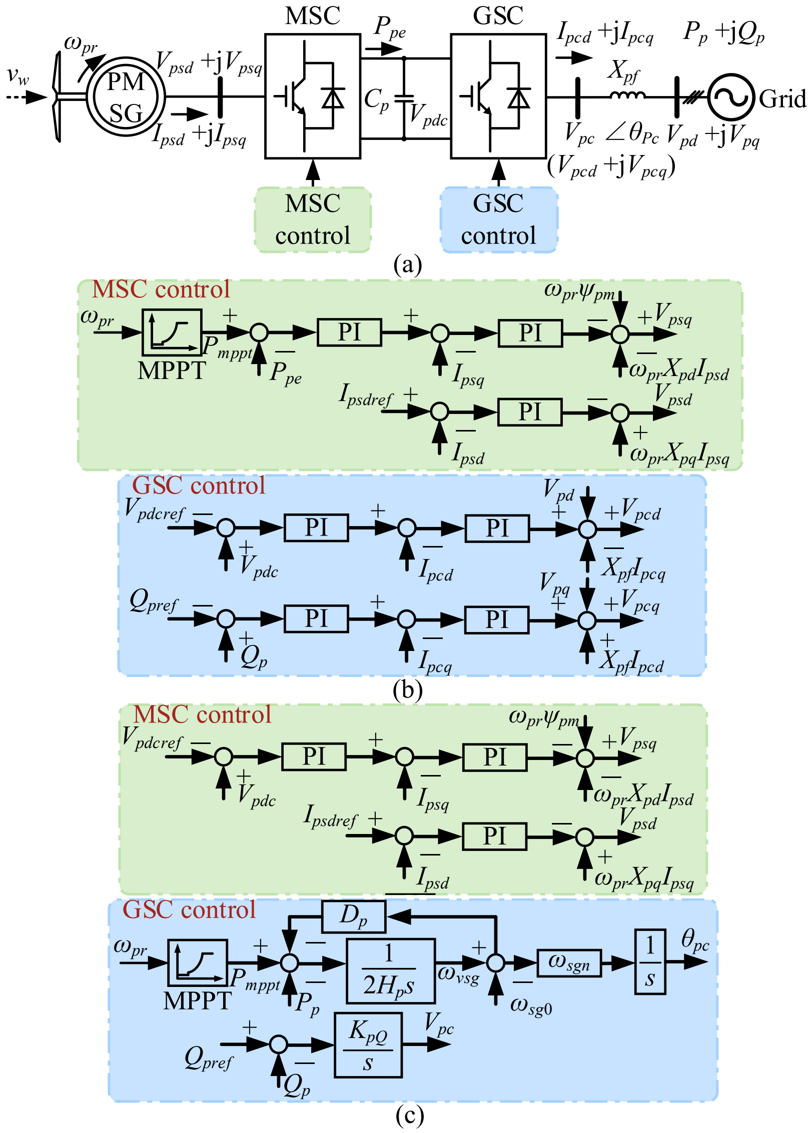

Fig. 2.1 Configuration of grid-connected WPG: (a) Physical structure; (b) Conventional grid-following control; (c) VSG-based grid-forming control.

The mechanical power P_{pm} extracted by WPG from wind can be expressed by [130]

$$P_{pm} = \varpi \pi R_p^2 C_w(\lambda, \beta) v_w^3 / 2 \tag{2.1}$$

where ϖ is the air density. R_p denotes the radius of turbine. v_w represents the wind speed. $C_w\left(\lambda, \beta\right)$ is the wind energy utilization coefficient with respect to the tip speed ratio λ and the pitch angle β, there is

$$C_w(\lambda,\beta) = 0.5176(116/\lambda_i - 0.4\beta - 5)e^{-21/\lambda_i} + 0.0068\lambda \tag{2.2}$$

where $\lambda = \omega_{pr} R_p / v_w$, and ω_{pr} is the rotor speed of WPG. $1/\lambda_i = 1/(\lambda + 0.08\beta) - 0.035/(\beta^3 + 1)$.

The motion equation of the rotor of PMSG can be expressed as [33]

$$J_{pr} d\omega_{pr} / dt = T_{pm} - T_{pe} \tag{2.3}$$

where J_{pr} is the constant of inertia of the rotor. $T_{pm} = P_{pm} / \omega_{pr}$ denotes the mechanical torque. $T_{pm} = P_{pm} / \omega_{pr}$ is the electromagnetic torque.

The reference signal of active power affected by wind speed variation is calculated based on the MPPT strategy, which can be expressed as [130]

$$P_{mppt} = \begin{cases} 0 & , v_w < v_{ci} \text{ or } v_w \geq v_{co} \\ k_{mppt}\omega_{pr}^3 & , v_{ci} \leq v_w \leq v_{rat} \\ P_{rat} & , v_{rat} < v_w < v_{co} \end{cases} \tag{2.1}$$

where v_{ci}, v_{co}, and v_{rat} are the cut-in, furling, and rated wind speed, respectively. P_{rat} denotes the rated output power of WPG. k_{mppt} is the coefficient of MPPT. P_{mppt} is the MPPT reference signal.

Thus, the variation of wind speed will affect the MPPT reference signal P_{mppt}. And then, the actual output of WPG P_p will change. Finally, due to the power imbalance between the generation and loads, the frequency will be affected. Also, from Fig. 2.1 (b) and Fig. 2.1(c), the main difference between these two strategies in frequency response is that for the VSG-based grid-forming control strategy, there is a signal of virtual rotor speed for mimicking the rotor dynamics of the synchronous generator (SG), thereby providing inertia support to the system and governing the output power of WPGs. By comparison, the conventional grid-following control cannot provide inertia support.

2.2.2 Frequency Response Analysis Considering Dynamics of Wind Power Generation with Different Control Strategies based on System Frequency Response Model

The aggregated system frequency response (SFR) model [109, 131] is applied to analyze the system frequency response, which reflects the average frequency response of all generators after a disturbance of load-generation unbalance. And the system frequency of the power system is usually regarded as the frequency of an equivalent generator, i.e., the center of inertia, that can reflect the average behavior of all the generators within the system [132]. The dynamics of WPGs are modeled as first-order transfer functions [133], where the equivalent time constants of different control strategies are different. And the inertia provided by VSG control is added to the system inertia [134], while the conventional grid-following control strategy cannot provide the inertia. The modified aggregated SFR model is shown in Fig. 2.2.

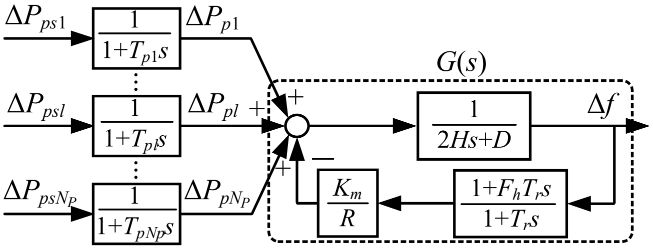

Fig. 2.2 Aggregated SFR model considering dynamics of WPGs and different control strategies.

In Fig. 2.2, K_m, R, F_h, T_r denote the aggregated gain of governors, governor speed regulation, high-pressure turbine fraction, and reheat time constant, respectively. D is the load damping factor. T_{pl} is the time constant of the dynamic response of the *l*-th WPG. ΔP_{pl} represents the *l*-th WPG output deviation after and before wind speed changes. Moreover, system inertia H can be derived as

$$H = (\sum_{c=1}^{N_S} H_{sc}S_{sc} + \sum_{c=1}^{N_V} H_{pc}S_{pc}) / S_{sys} \tag{2.2}$$

where N_S is the number of SGs. H_{sc} and S_{sc} denote the inertia and the rated apparent power of *c*-th SG. N_V is the number of WPGs with the VSG control. H_{Vc} and S_{Vc} denote the inertia and the rated apparent power of *c*-th WPG with the VSG control. S_{sys} is the system installed generation capacity without WPGs with grid-following control.

The frequency response without the WPG dynamics $G(s)$ is

$$G(s) = \frac{\dfrac{1}{2Hs+D}}{1+\dfrac{K_m(1+F_hT_rs)}{(2Hs+D)R(1+T_rs)}} = \frac{R\omega_n^2}{DR+K_m}\frac{1+T_rs}{s^2+2\varsigma\omega_n s+\omega_n^2} \tag{2.3}$$

where $\omega_n^2 = \dfrac{DR+K_m}{2HRT_r}$, $\varsigma = \dfrac{2HR+DRT_r+K_mF_hT_r}{2(DR+K_m)}\omega_n$.

Thus, the system frequency response Δf considering the output variation of WPGs in the *s*-domain can be derived as

$$\Delta f(s) = G(s)\sum_{l=1}^{N_P}\frac{1}{1+T_{pl}s}\Delta P_{psl}(s). \tag{2.4}$$

Since the dynamics are considered as first-order transfer functions, $\Delta P_{psl}(s)$ can be treated as a step signal from 0 to steady-state deviation of active power ΔP_{psl}.

Substituting (2.6) into (2.7), $\Delta f(s)$ can be transformed into

$$\Delta f(s) = \sum_{l=1}^{N_P}\frac{\Delta P_{psl}R\omega_n^2}{DR+K_m}\frac{1+T_rs}{(s^2+2\varsigma\omega_n s+\omega_n^2)(1+T_{pl}s)s}. \tag{2.5}$$

The partial fraction expansion of (2.8) can be written as

$$\Delta f(s)=\sum_{l=1}^{N_P}\frac{\Delta P_{psl}R\omega_n^2}{DR+K_m}\left(\frac{\eta_{1l}s+\eta_{2l}}{s^2+2\varsigma\omega_n s+\omega_n^2}+\frac{\eta_{3l}}{1+T_{pl}s}+\frac{\eta_4}{s}\right) \tag{2.6}$$

where η_{1l}, η_{2l}, η_{3l}, and η_4 are the undetermined coefficients of partial fraction expansion corresponding to the l-th WPG, which have no physical meaning and are introduced for simplifying the form of the following equations.

Transforming (2.8) into a common denominator and comparing it with (2.9), η_{1l}, η_{2l}, η_{3l}, and η_4 can be derived as

$$\begin{bmatrix}\eta_{1l}\\ \eta_{2l}\\ \eta_{3l}\\ \eta_4\end{bmatrix}=\begin{bmatrix}T_{pl} & 0 & 1 & T_{pl}\\ 1 & T_{pl} & 2\varsigma\omega_n & 1+2T_{pl}\varsigma\omega\\ 0 & 1 & \omega_n^2 & 2\varsigma\omega_n+T_{pl}\omega_n^2\\ 0 & 0 & 0 & \omega_n^2\end{bmatrix}^{-1}\begin{bmatrix}0\\ 0\\ T_r\\ 1\end{bmatrix}. \tag{2.7}$$

Transforming (2.9) from the s-domain to the time domain, the system frequency response in the time domain $\Delta f(t)$ is

$$\begin{aligned}\Delta f(t)&=\sum_{l=1}^{N_P}[\kappa_{1l}e^{-\varsigma\omega_n t}\sin(\omega_r t+\varphi_l)+\kappa_{2l}e^{-\frac{1}{T_{pl}}t}+\kappa_3]\Delta P_{psl}\\ &\doteq\sum_{l=1}^{N_P}C_l(t)\Delta P_{psl}\end{aligned} \tag{2.8}$$

where $\kappa_{1l}=\dfrac{R\omega_n^2\eta_{1l}\sqrt{(\eta_{2l}/\eta_{1l}-\varsigma\omega_n)^2+(1-\varsigma^2)\omega_n^2}}{(DR+K_m)\sqrt{1-\varsigma^2}\,\omega_n}$, $\omega_r=\sqrt{1-\varsigma^2}\,\omega_n$, $\varphi_l=\arctan\dfrac{\sqrt{1-\varsigma^2}\,\omega_n\eta_{1l}}{\eta_{2l}-\varsigma\omega_n\eta_{1l}}$, $\kappa_{2l}=\dfrac{R\omega_n^2\eta_{3l}}{(DR+K_m)T_{pl}}$, $\kappa_3=\dfrac{R\omega_n^2\eta_4}{DR+K_m}$.

Moreover, it should be noted that the above relationship is not only suitable for the frequency response considering the dynamics of WPGs with conventional grid-following control and VSG-based grid-forming control, but also suitable for more general scenarios, for example, considering the droop control of RPGs and uncertainties of loads and the power loss caused by contingencies. The droop control can be equivalent to an addition of the first-order negative-feedback transfer function in $G(s)$ [134]. And the variation of load and the power loss caused by contingencies can be equivalent to the addition of disturbance [132]. After the similar derivation presented above, the relationship in (2.11) is still valid, and just the form of $C_l(t)$ becomes more complicated.

Comparing (2.11) with the frequency response without the dynamics and different control strategies of WPGs in [131], the most significant difference is the introduction of the second term in (2.11), and the forms of the rest two items in (2.11) have the similar forms of those without the dynamics and different control strategies of WPGs. This indicates that RoCoF no longer occurs at the time when wind speed changes. Thus, to obtain frequency stability indices, the occurrence time of frequency stability indices should be derived firstly, where the derivative of frequency equaling to 0 should be solved. However, due to the introduction of the second term of (2.11), it becomes a transcendental equation without an explicit solution [135]. Thus, the closed-form relationship between frequency stability indices, i.e., RoCoF and FN/FV, and ΔP_{psl} cannot be derived.

The disappearance of the closed-form relationship brings difficulties in quantifying frequency stability indices under uncertainties. Since the second term of (2.11) is the main difference between the frequency with and without dynamics of WPGs, its response trend can greatly affect $\Delta f(t)$. To analyze the response trend of the second term of (2.11), ΔP_{ps1}, ΔP_{ps2}, $\cdots$, ΔP_{psN_P} are divided into two groups: $\Delta P_{ps.} \geq 0$ and $\Delta P_{ps.} < 0$. Applying the aggregated model of the WPG [136], the second term of (2.11) can be transformed into

$$\sum_{l=1}^{N_P} \kappa_{2l} e^{-\frac{1}{T_{pl}}t} \Delta P_{psl} = e^{-\frac{1}{T_{p+}}t} \sum_{l_+=1}^{N_{P+}} \kappa_{2l+} \Delta P_{psl+} + e^{-\frac{1}{T_{p-}}t} \sum_{l_-=1}^{N_{P-}} \kappa_{2l-} \Delta P_{psl-} \tag{2.9}$$

where l_+ and l_- are the indexes of $\Delta P_{ps.} \geq 0$ and $\Delta P_{ps.} < 0$, respectively. N_{P+} and N_{P-} denote the numbers of WPGs with $\Delta P_{ps.} \geq 0$ and $\Delta P_{ps.} < 0$, separately.

$$T_{p+} = \frac{\sum_{l_+=1}^{N_{P+}} T_{pl+} \kappa_{2l+} \Delta P_{psl+}}{\sum_{l_+=1}^{N_{P+}} \kappa_{2l+} \Delta P_{psl+}}, \quad T_{p-} = \frac{\sum_{l_-=1}^{N_{P-}} T_{pl-} \kappa_{2l-} \Delta P_{psl-}}{\sum_{l-=1}^{N_{P-}} \kappa_{2l-} \Delta P_{psl-}}.$$

If parameters in Fig. 2.2 are selected as reasonable values [132], κ_{2l} will be negative. The derivative of (2.12) indicates that, if all $\Delta P_{ps.} \geq 0$, (2.12) is monotonically increasing with t; if all $\Delta P_{ps.} < 0$, (2.12) is monotonically decreasing; if part of $\Delta P_{ps.} \geq 0$ and the rest of $\Delta P_{ps.} < 0$, there are situations that the derivative of (2.12) crosses through zero. Thus, the second term of (2.11) has 4 possible types of response trends, which contributes to 4 types of response trends of $\Delta f(t)$. Therefore, $\Delta P_{ps.}$ is divided into 4 elements, i.e., 1) all $\Delta P_{ps.} \geq 0$, 2) all $\Delta P_{ps.} < 0$, 3) $\sum_{l_+=1}^{N_{P+}} \Delta P_{psl+} \geq \sum_{l_-=1}^{N_{P-}} |\Delta P_{psl-}|$, and 4) $\sum_{l_+=1}^{N_{P+}} \Delta P_{psl+} < \sum_{l_-=1}^{N_{P-}} |\Delta P_{psl-}|$, corresponding to different response trends.

2.2.3 Multi-Interval Sensitivity for System Frequency Response

According to (2.11), based on the SFR model illustrated in Fig. 2.2, the explicit solution of FN/FV and RoCoF no longer exists after considering the dynamics of WPGs, which challenges the existing methods of probabilistic frequency stability analysis. And the relationship between the deviation of system frequency from the base frequency $\Delta f(t)$ and the steady-state output deviation of the l-th WPG after and before wind speed changes ΔP_{psl} can be expressed as:

$$\Delta f(t)=\sum_{l=1}^{N_P} C_l(t)\Delta P_{psl} \tag{2.10}$$

where N_P is the number of WPGs. $C_l(t)$ denotes the time-varying sensitivity.

Motivated by (2.13), if the time-varying sensitivity $C_l(t)$ can be derived, frequency response $\Delta f(t)$ with any combinations of ΔP_{ps1}, ΔP_{ps2}, $\cdots$, ΔP_{psN_P} can be calculated. This will greatly reduce the simulation number of the detailed system model in probabilistic frequency analysis. However, different from the SFR model presented in Fig. 2.2, as a simplified model, where $C_l(t)$ is fixed, for the actual system, $C_l(t)$ may be unfixed due to the complicated interaction and the existence of nonlinear blocks. Thus, to approximate the unfixed $C_l(t)$ and reflect the nonlinearity of the actual system, MIS is proposed. The core of MIS is to divide ΔP_{psl} into multiple intervals with respect to $C_l(t)$, suppose the sensitivity between $\Delta f(t)$ and ΔP_{psl} in each interval is fixed, and calculate the sensitivity in each interval to approximate the unfixed $C_l(t)$.

The calculation of interval sensitivity $C_{l,q}(t)$ in q-th interval with respect to $\Delta P_{psl,q}$ can be summarized as follows.

1) Divide the range of ΔP_{psl} into N_I intervals. The midpoint of q-th interval is $\Delta P_{psl,q}$.

2) Conduct the simulation at $\Delta P_{psl}=\Delta P_{psl,q}$ and other $\Delta P_{ps1}=\Delta P_{ps2}=\cdots=\Delta P_{psN_P}=0$ to calculate sensitivity $C_{l,q}(t)$ in q-th interval with

respect to $\Delta P_{psl,q}$ as

$$C_{l,q}(t) = \Delta f_{l,q}(t) / \Delta P_{psl,q} \tag{2.11}$$

where $\Delta f_{l,q}(t)$ is the frequency response when the system is only under the variation of wind speed in the l-th WPG without the variation of wind speed in other WPGs.

3) Repeat Step 1)-Step 2) to calculate all sensitivities with respect to ΔP_{ps1}, ΔP_{ps2}, $\cdots$, ΔP_{psN_P}.

4) Based on (2.15), generate the sampling data for the UPA.

$$\Delta f(t) \approx \sum_{l=1}^{N_P} \sum_{q=1}^{N_I} C_{l,q}(t) I_{l,q} \Delta P_{psl} \tag{2.12}$$

where $I_{l,q} = \begin{cases} 1, \Delta P_{psl} \text{ in } q\text{-th interval} \\ 0, \quad\quad \text{otherwise} \end{cases}$.

The interval splitting of ΔP_{psl} and the calculation of $C_l(t)$ are presented in Fig. 2.3, which are the illustrations of Step 1) and Step 2) of MIS, respectively.

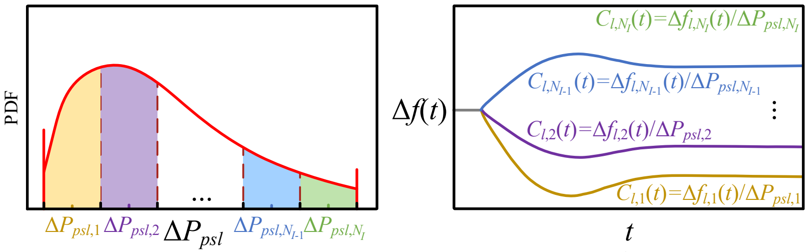

(a) (b)

Fig. 2.3 (a) Interval splitting of ΔP_{psl} (Step 1)); (b) Calculation of $C_l(t)$ (Step 2)).

2.2.4 Multi-Interval Sensitivity for Area-Level Frequency Response

In power systems, when there is an active power disturbance, the disturbance will be shared by every generator. Thus, ΔP_{psl} allocated to u-th SGs or WPGs with VSG control $\Delta P_{tl,u}$ can be depicted as [22]

$$\Delta P_{tl,u} = B_{l,u}\Delta P_{psl} \tag{2.13}$$

where $B_{l,u}$ is the distribution coefficient, which is only determined by system parameters and not affected by ΔP_{psl} [22]. And the area-level center of inertia is aggregated by the generators within the area. The area-level frequency is calculated by aggregating the generator frequency within the area, where the inertia ratio between the generator and the area center of inertia is the aggregation weight [22, 24, 132]. Thus, the frequency $\Delta f^{(a)}(t)$ of the a-th area can be calculated as

$$\Delta f^{(a)}(t) = \sum_{u=1}^{N_a} H_u^{(a)} \Delta f_u^{(a)}(t) / \sum_{u=1}^{N_a} H_u^{(a)} \tag{2.14}$$

where N_a is the number of generators in the a-th area. $H_u^{(a)}$ and $\Delta f_u^{(a)}(t)$ denote the inertia and frequency of u-th generator in the a-th area, respectively.

Since $\Delta f_u^{(a)}(t)$ and ΔP_{psl} has the similar relationship presented in (2.13), substituting (2.13) and (2.16) into (2.17), the area-level frequency response can be derived as

$$\Delta f^{(a)}(t) = \sum_{u=1}^{N_a} [H_u^{(a)} \sum_{l=1}^{N_P} C_l(t) B_{l,u} \Delta P_{psl}] / \sum_{u=1}^{N_a} H_u^{(a)}. \tag{2.15}$$

Similarly, MIS can be applied to approximate the sensitivity $C_l(t)$ in (2.18). Thus, the approximated area-level frequency response $\Delta f^{(a)}(t)$ based on MIS can be derived as

$$\Delta f^{(a)}(t) \approx \sum_{u=1}^{N_a} [H_u^{(a)} \sum_{l=1}^{N_P} \sum_{q=1}^{N_I} C_{l,q}(t) I_{l,q} B_{l,u} \Delta P_{psl}] / \sum_{u=1}^{N_a} H_u^{(a)}. \tag{2.16}$$

It should be noted that in the actual system, where the inter-area oscillation is considered, $C_l(t)$ may be unfixed. And the introduction of the multi-interval in the proposed MIS is to cope with the scenario that $C_l(t)$ is unfixed due to the complicated interaction and nonlinearity. Thus, the proposed MIS with the form of (2.19) is effective when considering inter-area oscillation. The procedure of area-level frequency calculation considering output variations of WPGs is illustrated in Fig. 2.4.

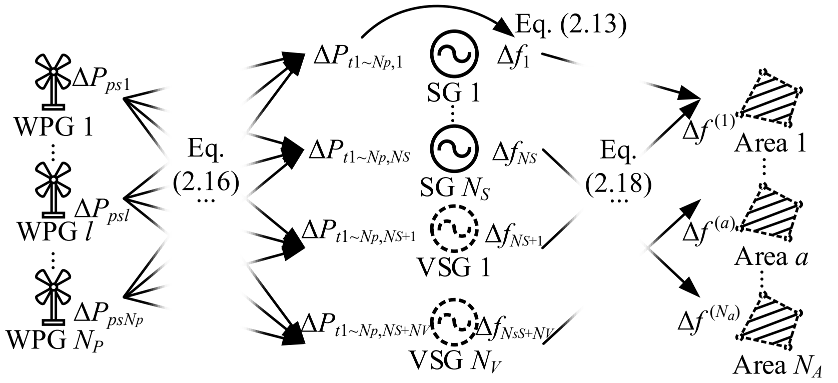

Fig. 2.4 Area-level frequency calculation considering output variation of WPGs.

2.3 Multi-Element Low-Rank Approximation for Probabilistic Frequency Stability Analysis

2.3.1 Uncertainty Modeling of Wind Power Generation

Uncertainties of WPGs are characterized by the PDFs of wind speed variation, and the steady-state active power after the fluctuation of wind speed is calculated based on the MPPT strategy [130]. The PDF $p_{Cop}(.)$ of uncertainties $\xi_{c1}, \xi_{c2}, \cdots, \xi_{cN_C}$ with correlation is modeled by the Copula function as [109]

$$
\begin{aligned}
&p_{Cop}(\xi_{c1}, \xi_{c2}, \cdots, \xi_{cN_C}) \\
&= \frac{\partial^{N_c} \psi_{\boldsymbol{\rho}_{\xi c1\sim NC}}(\psi^{-1}(\xi_{c1}), \psi^{-1}(\xi_{c2}), \cdots, \psi^{-1}(\xi_{cN_C}))}{\partial P(\xi_{c1}) \partial P(\xi_{c2}) \cdots \partial P(\xi_{cN_C})} \prod_{x=1}^{N_C} p(\xi_{cx})
\end{aligned}
\tag{2.17}
$$

where N_C is the number of wind speed with correlation. $\boldsymbol{\rho}_{\xi c1\sim NC}$ denotes the correlation matrix of $\xi_{c1}, \xi_{c2}, \cdots, \xi_{cN_C}$. $P(.)$ is the integral of $p.(\cdot)$. $p(.)$ denotes the PDF. $\psi(.)$ is the generator function of Copula, selected as the Gaussian function.

Since the input uncertainties of LRA-based methods are required to be uncorrelated, $\xi_{c1}, \xi_{c2}, \cdots, \xi_{cN_C}$ should be transformed into uncorrelated ones $\xi_1, \xi_2, \cdots, \xi_{N_C}$, where Cholesky decomposition is adopted [109].

$$\boldsymbol{\xi} = \boldsymbol{C}^{-1}\boldsymbol{\xi_c} \tag{2.18}$$

where $\xi_{c1}, \xi_{c2}, \cdots, \xi_{cN_C}$ and $\xi_1, \xi_2, \cdots, \xi_{N_C}$ are the elements of $\boldsymbol{\xi_c}$ and $\boldsymbol{\xi}$, respectively. $\boldsymbol{C}$ is the Cholesky decomposition matrix, which can be calculated from $\boldsymbol{\rho}_{\xi c1\sim NC} = \boldsymbol{C}\boldsymbol{C}^T$.

2.3.2 Multi-Element Low-Rank Approximation

LRA-based UPA methods apply a series of orthogonal polynomials corresponding to the PDFs of uncertainty $\boldsymbol{\xi}$ to approximate the relationship $M(\boldsymbol{\xi})$ between the concerned output y and $\boldsymbol{\xi}$. In this chapter, $\boldsymbol{\xi}$ refers to the uncertainty of WPGs and y stands for frequency stability indices.

$$y = M(\boldsymbol{\xi}) \approx \hat{y} = \hat{M}(\boldsymbol{\xi}) = \sum_{i=1}^{N_R} b_i w_i(\boldsymbol{\xi}) \tag{2.19}$$

where N_R is the rank, which is the number of rank-one function $w_i(\boldsymbol{\xi})$. b_i denotes the *i*-th normalizing weighting coefficient. Superscript ^ is the approximated value or function from UPA methods. $w_i(\boldsymbol{\xi})$ represents *i*-th rank-one function of $\boldsymbol{\xi}$, which has the following form.

$$w_i(\boldsymbol{\xi}) = \prod_{j=1}^{N_U} \left(\sum_{k=0}^{N_D} z_{k,i}^{(j)} \phi_k(\xi_j)\right) \tag{2.20}$$

where N_U is the number of uncertainties. $\phi_k(\xi_j)$ denotes the k-th degree univariate polynomial basis of ξ_j. N_D is the maximum degree of $\phi_k(\xi_j)$. $z_{k,i}^{(j)}$ represents the coefficient of k-th degree univariate polynomial of ξ_j in the i-th rank-one component. Thus, the main work of constructing the LRA model is to determine b_i, $z_{k,i}^{(j)}$, and $\phi_k(\xi_j)$.

1) Multi-Element Decomposition

Based on the analysis in Chapter 2.2.2, the frequency response has different possible trends when considering the dynamics of WPGs. Thus, MELRA is proposed aiming at suitable for the concerned output with multiple response trends. In this chapter, the elements in MELRA correspond to the elements of WPG outputs divided in Chapter 2.2.2.

The random space $\boldsymbol{\Omega}$ formed by the value range of uncertainty $\boldsymbol{\xi}$ is divided into N_E elements as

$$\boldsymbol{\Omega} = \bigcup_{n=1}^{N_E} \boldsymbol{\Omega}_n, \boldsymbol{\Omega}_{\bar{n}} \bigcap \boldsymbol{\Omega}_n = \varnothing, \bar{n} \neq n \tag{2.21}$$

where $\boldsymbol{\Omega}_n$ is the n-th element of $\boldsymbol{\Omega}$.

The indicator function $F_{\boldsymbol{\Omega}_n}$ is defined as

$$F_{\boldsymbol{\Omega}_n} = \begin{cases} 1, \text{ if } \boldsymbol{\xi} \in \boldsymbol{\Omega}_n \\ 0, \text{otherwise} \end{cases}. \tag{2.22}$$

Thus, the probability $\Pr(F_{\boldsymbol{\Omega}_n})$ of $\boldsymbol{\xi}$ in $\boldsymbol{\Omega}_n$ can be calculated as:

$$\Pr(F_{\boldsymbol{\Omega}_n}) = \int_{\xi \in \boldsymbol{\Omega}_n} \prod_{j=1}^{N_U} p(\xi_j) d\xi. \tag{2.23}$$

After considering multiple elements, the form in (2.22) is transformed into

$$\hat{y} = \hat{M}(\xi) = \sum_{n=1}^{N_E} \{F_{\Omega_n} \sum_{i=1}^{N_R} [b_{i,n} \prod_{j=1}^{N_U} (\sum_{k=0}^{N_D} z_{k,i,n}^{(j)} \phi_{k,n}(\xi_j))]\}. \tag{2.24}$$

It should be noted that the summation form of different elements is not the aggregation of distinct potential trends of frequency response but the combination of separate elements of random space, i.e., random subspaces, into a whole random space with a concise form. And each sampled data of uncertainties only corresponds to one trend of frequency response.

2) Construction of Polynomial Bases for Arbitrary Distributions

The conventional construction of polynomial bases is based on the Askey scheme [97], which is only suitable for several typical PDFs. However, Weibull distribution is not included in the Askey scheme, which is usually applied to model the uncertainty of wind speed. Thus, a generic construction principle of polynomial bases for arbitrary distributions based on the orthogonality of polynomial bases is proposed.

The polynomial basis $\phi_k(\xi_j)$ can be described as

$$\phi_k(\xi_j) = \sum_{g=0}^{k} \alpha_g \xi_j^g \tag{2.25}$$

where α_g is the coefficient of the g-th power of ξ_j.

According to the orthogonality, there is:

$$\int \phi_v(\xi_j)\phi_k(\xi_j)p(\xi_j)d\xi_j = 0, 0 \le v < k. \tag{2.26}$$

Substituting $v = 0, 1, 2, \cdots, k-1$ into (2.29) in turns, $\alpha_0, \alpha_1, \cdots, \alpha_{k-1}$ can be calculated orderly.

The above procedure can be summarized as:

$$[\alpha_0, \alpha_1, \cdots, \alpha_{k-1}]^T = \mathbf{\Theta}^{-1}[\chi_1, \chi_2, \cdots, \chi_k]^T \tag{2.27}$$

where $\boldsymbol{\Theta} = (\theta_{vs})_{k\times k}$. $\theta_{vs} = \int p(\xi_j)\xi_j^{v+s-2}d\xi_j, 1 \le v, s \le k$. $\chi_v = -\int p(\xi_j)\xi_j^{v+k+1}d\xi_j, 1 \le v \le k$.

3) Computation of Undetermined Coefficients

Firstly, LHS [103] is conducted to acquire a set of samples $\boldsymbol{\xi}_{(1\sim N_L)}$ and the corresponding $y_{(1\sim N_L)}$, where N_L is the number of sampled data.

During the computation of undetermined coefficients b_i and $z_{k,i}^{(j)}$, the correction step and updating step are conducted in turns and stopped until the number of iterations is greater than the threshold of iteration number or the error $\| y_{(1\sim N_L)} - \hat{y}_{(1\sim N_L)} \|^2$ is smaller than the error threshold. In the *r*-th correction step, a new $w_r(\boldsymbol{\xi})$ is determined. And in the *r*-th updating step, $b_1, b_2, \cdots, b_r$ are updated.

Correction Step: The objective of the *r*-th correction step is to find new $w_r(\boldsymbol{\xi})$ and minimize the residual error between sampled data and the outputs of the current LRA model, which can be described as

$$w_r(\boldsymbol{\xi}) = \arg\min_{\omega\in W} \| y_{(1\sim N_L)} - \hat{M}_{r-1}(\boldsymbol{\xi}_{(1\sim N_L)}) - \omega(\boldsymbol{\xi}_{(1\sim N_L)}) \|^2 \tag{2.28}$$

where W is the space of rank-one function ω. $\hat{M}_{r-1}(.)$ is the LRA model with $r-1$ rank. To solve (2.31), alternated least-square minimization is applied [100].

Updating Step: After the *r*-th correction step, b_r corresponding to $w_r(\boldsymbol{\xi})$ needs to be calculated. Also, $b_1, b_2, \cdots, b_{r-1}$ should be updated. $b_1, b_2, \cdots, b_r$ are the elements of $\boldsymbol{b}_r$, and the determination of $\boldsymbol{b}_r$ can be achieved by solving the following optimization problem

$$\boldsymbol{b}_r = \arg\min_{\beta\in\Re^r} \| y_{(1\sim N_L)} - \sum_{i=1}^{r} \beta_i w_i(\boldsymbol{\xi}_{(1\sim N_L)}) \|^2 . \tag{2.29}$$

4) Selection of Optimal Number of Rank and Degree

To select the optimal numbers of ranks and degrees, the leave-one-out (LOO) error e_{LOO} is introduced. The error of all $\hat{M}(\xi)$ satisfying $N_R \le N_{R\max}$ and $N_D \le N_{D\max}$ is calculated, where $N_{R\max}$ and $N_{D\max}$ are the maximum of available N_R and N_D, respectively. N_R and N_D corresponding to the lowest ε_{LOO} are chosen as the optimal numbers of ranks and degrees. ε_{LOO} can be calculated as [102]:

$$\varepsilon_{LOO} = \sum_{h=1}^{N_L} (\frac{y_{(h)} - \hat{y}_{(h)}}{1-\lambda_h})^2 / \sum_{h=1}^{N_L} (y_{(h)} - \mathbf{E}(y_{(1\sim N_L)}))^2 \tag{2.30}$$

where λ_h is the *h*-th element of $\boldsymbol{\lambda} = diag(\Lambda(\Lambda^T\Lambda)^{-1}\Lambda^T)$. $w_i(\xi)$ is the *i*-th element of Λ. $\mathbf{E}(.)$ is the expectation operator.

To ensure the accuracy of the model, ε_{LOO} of the model corresponding to the optimal numbers of ranks and degrees is required to be lower than the preset $\varepsilon_{LOO\max}$; otherwise $N_{R\max}$ and $N_{D\max}$ will be increased to select the numbers of ranks and degrees meeting the error requirement.

Finally, the estimated PDF $\hat{p}(\hat{y})$ of $\hat{y}$ can be calculated based on KDE

$$\hat{p}(\hat{y}) = \sum_{u=1}^{N_K} p_K((\hat{y} - \hat{y}_{(u)}) / \delta_K) / (N_K \delta_K) \tag{2.31}$$

where N_K is the sample number of KDE. $p_K(.)$ represents the kernel function, chosen as the Gaussian kernel. δ_K is the bandwidth of KDE.

Based on Chapter 2.2 and Chapter 2.3, the overall procedure of the proposed PFSA based on MIS-MELRA can be summarized in Fig. 2.5.

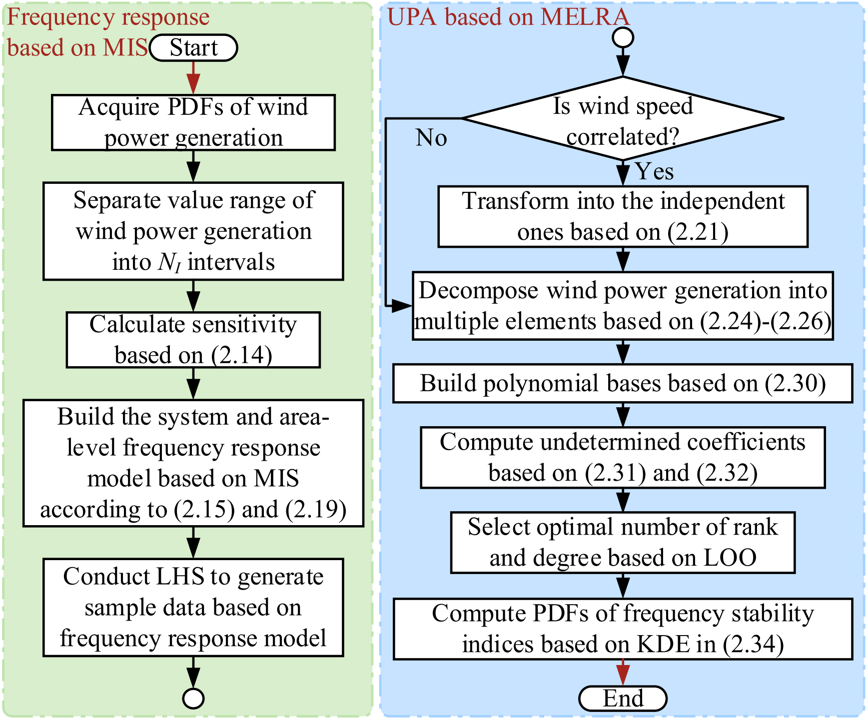

Fig. 2.5 Overall procedure of proposed PFSA based on MIS-MELRA.

2.4 Discussion on Superiority of LRA-based Uncertainty Propagation Analysis Methods

2.4.1 Limitation of Moment-Based Uncertainty Propagation Analysis Methods

Moment-based UPA methods (e.g., CBMs, PEMs) adopt limited moments to obtain PDFs of uncertainties based on series expansion. However, normally, limited moments of uncertainties can only reflect finite characteristics of uncertainties, while PDFs contain more detailed characteristics. Due to the unequal quantity of characteristics reflected by PDFs and limited moments, the effectiveness of moment-based UPA methods is worth discussing. Since GMM can describe arbitrary PDFs [137], it is applied to discuss the above issue in this chapter.

GMM can be modeled as

$$p_G(\xi) = \sum_{m=1}^{N_G} \omega_{Gm} Gau(\xi \mid \mu_{Gm}, \sigma_{Gm}) \tag{2.32}$$

$$\sum_{m=1}^{N_G} \omega_{Gm} = 1, \omega_{Gm} \geq 0, \sigma_{Gm} > 0 \tag{2.33}$$

where ξ is the uncertainty. $p_G(\xi)$ denotes the PDF of ξ modeled by GMM. ω_{Gm}, μ_{Gm}, and σ_{Gm} represent the weight coefficient, the mean, and the standard deviation of m-th Gaussian component, respectively.

The d-th order origin moment of GMM o_{Gd} can be calculated as

$$o_{Gd} = \sum_{m=1}^{N_G} \omega_{Gm} \sum_{e=0}^{d} \frac{d!}{2^{(d-e)/2} e![(d-e)/2]!} \mu_{Gm}^{e} \sigma_{Gm}^{d-e} \tag{2.34}$$

where $d-e$ is even.

Thus, the estimation of the actual PDF $p(\xi)$ based on moments and GMM can be transformed into the following nonlinear optimization problem.

$$\begin{gathered} \boldsymbol{\omega_G}, \boldsymbol{\mu_G}, \boldsymbol{\sigma_G} = \arg\min \sum_{d=1}^{N_O} (o_{Gd} - o_d)^2 \\ s.t. (2.36) \end{gathered} \tag{2.35}$$

where ω_{Gm}, μ_{Gm}, and σ_{Gm} are the m-th elements of $\boldsymbol{\omega_G}$, $\boldsymbol{\mu_G}$, and $\boldsymbol{\sigma_G}$. o_d is the d-th order origin moment of $p(\xi)$. N_O is the considered number of moments.

Also, the estimation of the actual PDF $p(\xi)$ based on the shape difference of PDFs and GMM can be transformed into

$$\begin{gathered} \boldsymbol{\omega_G}, \boldsymbol{\mu_G}, \boldsymbol{\sigma_G} = \arg\min \| p_G(\xi) - p(\xi) \|^2 \\ s.t. (2.36) \end{gathered} . \tag{2.36}$$

Due to the utilization of series expansion in moment-based UPA methods, if the limited moments of uncertainties are close, the shapes of expanded PDFs will also be similar. If the above relationship truly exists, within moment errors, all the feasible solutions of (2.38) should converge around the actual values, and the shapes of corresponding PDFs should be similar. To verify the existence of the above relationship, we take the standard Gaussian distribution as an example. To visualize the results in 3D space, the number of parameters should be reduced to 3. Thus, N_G is selected as 2, $o_{G1} = o_1$, and $\sigma_{G1} = \sigma_{G2}$. Parameters satisfying the first 5-order origin moments $(o_{Gd} - o_d)^2 \leq 0.05$ are drawn in Fig. 2.6(a). Among the results, two PDFs with close moments are presented in Fig. 2.6(b) as examples. The origin moments of PDFs in Fig. 2.6(b) are presented in Table 2.1.

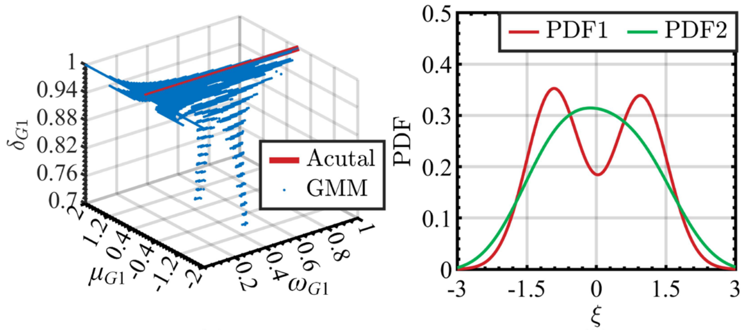

(a) (b)

Fig. 2.6 Estimation results of GMM: (a) Feasible values satisfying the requirement of moment error; (b) PDFs with close moments.

Table 2.1 Comparison of origin moments

	Order of moment				
	1st	2nd	3rd	4th	5th
PDF1	0	1.2219	0.0333	2.9120	0
PDF2	0	1.2211	0.0338	2.9242	0

From Fig. 2.6(a), the possible values are distributed and do not converge around the actual values. This indicates that the possible shapes of GMM are diverse, which can be further confirmed based on the results in Fig. 2.6(b) and Table 2.1. From Fig. 2.6(b) and Table 2.1, the moments of PDF1 and PDF2 are very close. However, the shapes of PDF1 and PDF2 are quite different. This indicates that there is a possibility that PDFs with close moments may have very different shapes. Moreover, the moment-based methods calculate the moments first and then apply the derived moments to calculate PDFs. Thus, even if the limited moments calculated by moment-based methods are within an acceptable error range, the PDFs generated by moment-based methods are not reliable and may be quite different from the actual PDFs.

To further investigate the relationship between the moment and shape differences of PDFs, the values of GMM coefficients are traversed. And the scatter figure about the moment difference and shape difference is presented in Fig. 2.7.

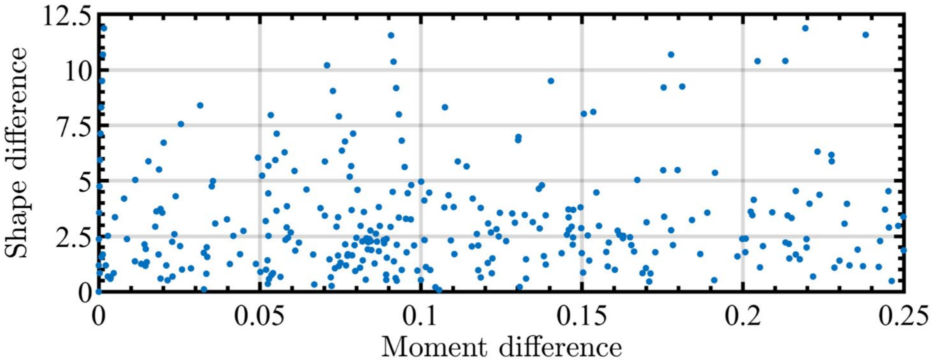

Fig. 2.7 Relationship between moment difference and shape difference.

In Fig. 2.7, data are scattered, and there is no obvious approximately linear relationship between the moment difference and the shape difference of PDF, which indicates that the moments of PDFs with similar shapes may be greatly different, while the shapes of PDFs with similar moments may also differ significantly. The results suggest that the UPA methods based on finite moments have limitations to some extent.

Since the finite moments do not fully reflect the statistical characteristics of uncertainties, and even if the accurate results of moments can be obtained, the accuracy of PDFs cannot be guaranteed.

2.4.2 Connections and Differences between LRA and PCE

LRA and PCE are both surrogate models based on polynomial bases. The construction of polynomial bases is the same. However, the differences of the forms between LRA and PCE result in LRA being more suitable for propagation analysis on numerous uncertainties. $\hat{M}_E(\xi)$ of conventional PCE can be described as:

$$\hat{M}_E(\xi) = \sum_{i=0}^{N_{PCE}-1} \gamma_i \phi_{i_1}(\xi_1) \otimes \phi_{i_2}(\xi_2) \otimes \cdots \otimes \phi_{i_{N_U}}(\xi_{N_U}),\ \{i_j \mid \sum_{j=1}^{N_U} i_j \le N_D\} \tag{2.37}$$

where N_{PCE} is the number of undetermined coefficients γ_i. $\otimes$ denotes the tensor product.

By comparison, (2.22) is the tensor-product form, whereas (2.40) is the expanded form. Thus, the number of undetermined coefficients of LRA N_{LRA} is much smaller than that of PCE N_{PCE} when considering numerous uncertainties since N_R and N_D are normally small. Based on (2.41), the increase of N_{LRA} and N_{PCE} with the rise of N_U is illustrated in Fig. 2.8(a) when $N_D = 3$. From Fig. 2.8(a) N_{LRA} rises linearly with the increase of N_U, where the curse of dimensionality is avoided.

$$\begin{cases} N_{LRA} = N_R(N_D N_U + 1) \\ N_{PCE} = (N_U + N_D)!/(N_U!N_D!) \end{cases}. \tag{2.38}$$

Furthermore, under the same N_D, more high-order cross terms of polynomial bases are considered in LRA, which contributes to the better performance of LRA in the approximation of high-order nonlinear relationships. The order combinations of polynomials are presented in Fig. 2.8(b) when $N_D = 3$, $N_U = 3$.

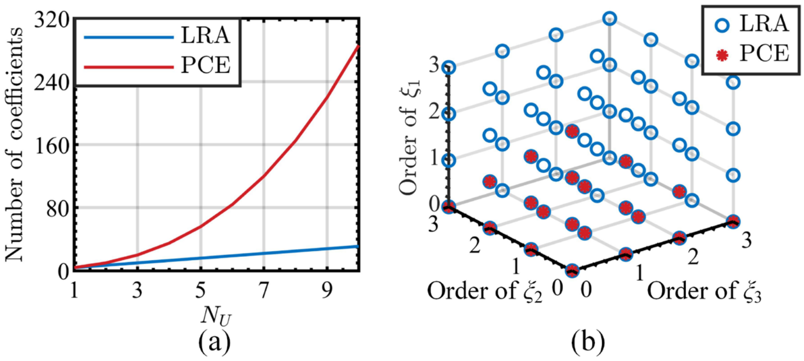

(a)
(b)

Fig. 2.8 Differences between LRA and PCE: (a) Number of undetermined coefficients corresponding to N_U; (b) Order combinations of polynomials.

2.5 Case Study

2.5.1 Case 1: IEEE 68-Bus Benchmark System

1) Example System

Numerous results are conducted in the IEEE 68-bus benchmark system [22] based on the detailed models of WPGs illustrated in Chapter 2.2.1 and the power system. The full-order governor model with a limiter is applied [132]. The system is divided into 5 areas based on the geographical location [138]. The parameters of different control strategies refer to [30, 39]. The line diagram and the parameters of uncertainties are presented in Fig. 2.9 and Table 2.2, respectively. It should be noted that the sudden changes of wind speeds are regarded as uncertainties, which is a relatively common phenomenon in reality. And to ensure that the uncertainty settings in case studies are similar to the actual situation, the random degree of wind speed change in case studies is set to a similar level of the measurement in [139].

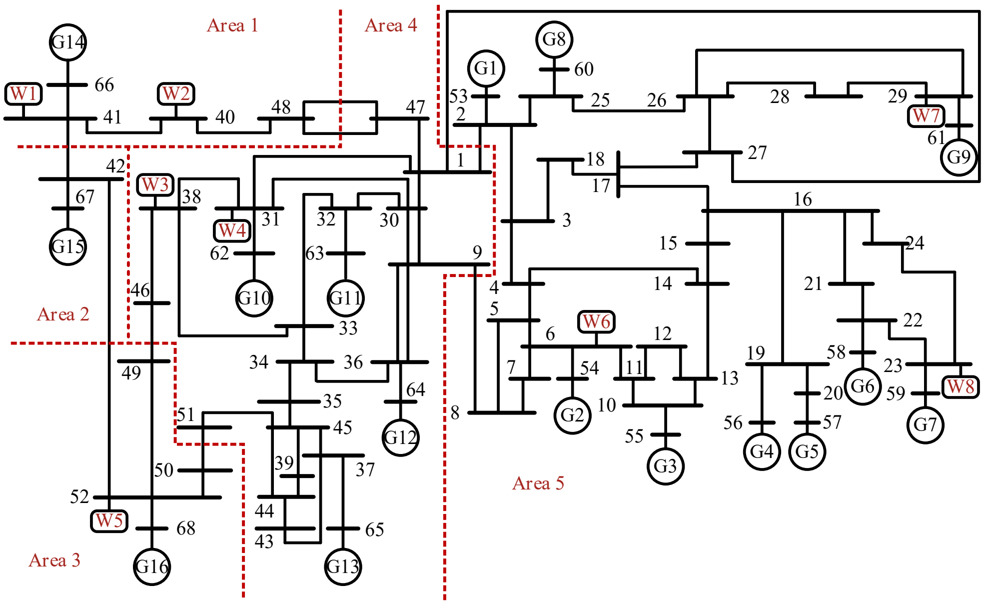

Fig. 2.9 Line diagram of IEEE 68-bus system with uncertainties.

Table 2.2 Parameters of uncertainties in Case 1

WPG No.	Control strategy	Parameters
W1, 2	Normal, VSG	$Weibull(2.5, 4.5, 4),\ \rho_{\xi_c} = 0.7$
W3, 4	Normal, VSG	$Weibull(2, 5, 3.5),\ \rho_{\xi_c} = 0.5$
W5, 6	Normal, VSG	$Weibull(2.5, 2.4, 4)$
W7, 8	Normal, VSG	$Weibull(2, 3, 3.5)$

2) Validation of Probabilistic Frequency Stability Analysis

The performance of the proposed MIS is verified first. Sensitivity analysis of calculation error of FN/FV and RoCoF based on MIS with respect to N_I is conducted, where mean absolute percentage error (MAPE) [111] is selected as the evaluation indicator. The results of sensitivity analysis are presented in Fig. 2.10(a), where the MAPE units of FN/FV and RoCoF are 10^{-1}% and %, respectively.

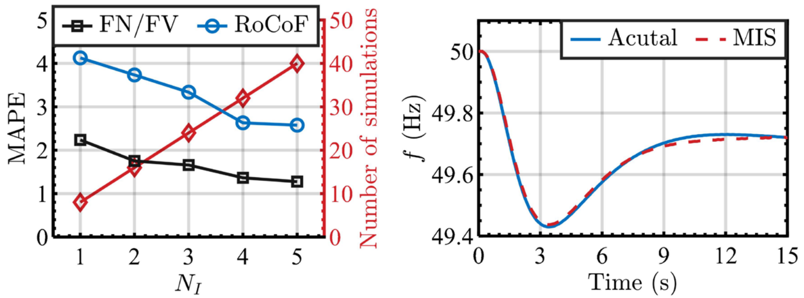

(a) (b)

Fig. 2.10 Performance of MIS: (a) Sensitivity analysis of N_I; (b) Comparison of actual system frequency response and that calculated by MIS when N_I=2.

From Fig. 2.10, both the MAPE of FN/FV and that of RoCoF are small when N_I is set as different values. Moreover, MAPEs of FN/FV and RoCoF decrease with the increase of N_I. The results of the sensitivity analysis demonstrate the high accuracy of the proposed MIS. Also, though the larger value selection of N_I will obtain more accurate results, the number of simulations will linearly increase with N_I simultaneously. Thus, a relatively small value selection of N_I will utilize the advantage of MIS in reducing the number of simulations more sufficiently. And N_I is selected as 2 not 1 in the following case studies for enabling the MIS to characterize the nonlinear relationship between the frequency response and the output power of WPGs. Moreover, the actual system frequency response and that calculated by MIS when N_I=2 are drawn in Fig. 2.10(b), where all wind speeds change to 6m/s as an example. Two frequency trajectories almost overlap, which illustrates that setting N_I as 2 can serve the purpose of accurate calculation.

The performance of the proposed MIS-MELRA is compared with cumulant-based Gram-Charlier expansion [27] (CGCE), PCE, and LRA. The expansion order of CGCE is selected as 8 [27]. The expansion order of PCE is chosen as 4 [97]. The rank and degree of LRA are 1 and 4, respectively [102]. The parameters of MIS-MELRA are set as: $N_{R\max}=2$, $N_{D\max}=4$, and $\varepsilon_{LOO\max}=10^{-3}$. The number of sampling data of PCE, LRA, and MIS-MELRA is 200 [100]. MCS considering the dynamics of WPGs (denoted as MCS-DR) is conducted 5000 times [21], and the results are regarded as the baseline. Also, MCS without the dynamics of WPGs (denoted as MCS-NDR) is carried out. The simulation time t_S, method execution time t_M, and total time t_T of different methods are presented in Table 2.3.

Table 2.3 Time comparison of different methods in analyzing FN/FV and RoCoF in Case 1

Time Index	t_S (s)	t_M (s)	t_T (s)
MCS-NDR	42889.01	-	42889.01
MCS-DR	44256.15	-	44256.15
CGCE	70.65	0.72	71.37
PCE	1770.15	1.49	1771.64
LRA		0.66	1770.81
MIS-MELRA	146.65	4.80	151.45

From Table 2.3, since the detailed model of WPGs is not considered in MCS-NDR, t_T of MCS-NDR is less than that of MCS-DR, but both of them are time-consuming. Besides, from the perspective of t_M, CGCE is the fastest, while MIS-MELRA takes the longest time due to the more complex calculation process. However, t_M only takes a small amount of t_T, which mainly depends on t_S. By comparison, CGCE only needs N_U simulations, leading to it being the most time-saving method. Although PCE, LRA, and MIS-MELRA need 200 simulations, only the $N_I N_U$ simulations of the actual system are conducted to obtain (2.15) in MIS-MELRA. And most simulations are carried out based on (2.15), which makes MIS-MELRA save much t_S compared with other surrogate models.

Furthermore, the PDF results of FN/FV and RoCoF are presented in Fig. 2.11, respectively. The shape differences of the corresponding PDFs are illustrated in Table 2.4. The shape difference is defined as the Euclidean distance between the actual PDF $p(y)$ and the estimated PDF $\hat{p}(\hat{y})$ same as (2.39), i.e., $\|p(y)-\hat{p}(\hat{y})\|$. For saving space, only the results of Area 1, Area 2, and system are presented. $d_{\cdot}$ is the shape difference of PDF. The FN/FV and RoCoF of frequency in Area a are denoted as F_{Aa} and R_{Aa}, respectively. The FN/FV and RoCoF of system frequency are denoted as F_{sys} and R_{sys}.

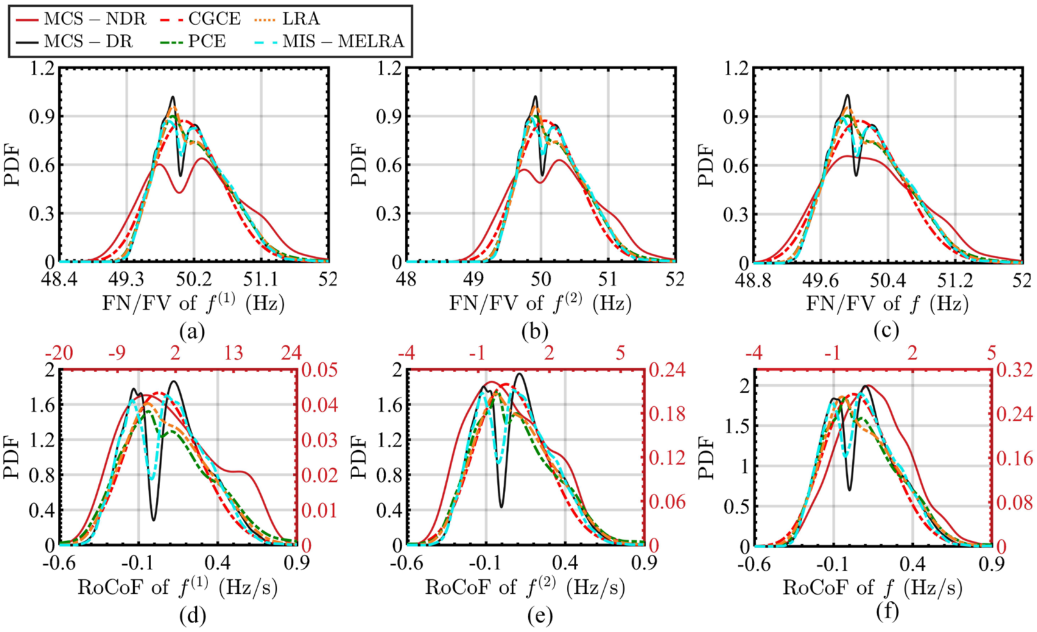

Fig. 2.11 PDF of FN/FV and RoCoF in Case 1: (a) FN/FV of Area 1; (b) FN/FV of Area 2; (c) FN/FV of system; (d) RoCoF of Area 1; (e) RoCoF of Area 2; (f) RoCoF of system.

Table 2.4 Performance of different methods in analyzing FN/FV and RoCoF in Case 1

Shape difference	$d_{F_{A1}}$	$d_{F_{A2}}$	$d_{F_{sys}}$	$d_{R_{A1}}$	$d_{R_{A2}}$	$d_{R_{sys}}$
CGCE	2.07	2.06	2.06	8.13	7.25	5.83
PCE	1.53	1.52	1.50	8.08	7.19	5.82
LRA	1.52	1.51	1.50	8.11	7.20	5.88
MIS-MELRA	0.93	0.95	0.96	4.01	3.73	3.27

As presented in Fig. 2.11, there are two peaks of FN/FV and RoCoF PDFs based on the results of MCS-DR. By comparison, shapes of PDFs of FN/FV and RoCoF under MCS-NDR are approximated one-peak and have fatter tails. The reason is that when ignoring the dynamics of WPGs, the injected power from WPGs will not change gradually but suddenly, leading to a bigger deviation of frequency, FN/FV, and RoCoF. Moreover, when ignoring the dynamics of WPGs, if the sum of the steady-state output power of WPGs after the variation of wind speed is close to 0, the deviation of frequency will also be close to 0. However, since WPGs have different dynamics, the sum of the output power of WPGs is not close to 0 from the moment when wind speed changes to the end of the dynamic process, which contributes to the occurrence of two peaks in the PDFs of FN/FV and RoCoF. This indicates the necessity of considering the dynamics of WPGs in PFSA.

Furthermore, from Fig. 2.11 and Table 2.4, compared with PDFs of other methods, the PDFs from MIS-MELRA have the highest similarity with the PDFs from MCS-DR in both FN/FV and RoCoF. After MIS-MELRA, the performance of LRA is slightly better than that of PCE. The performance of CGCE is the worst since CGCE is based on the premise that there is a proportional relationship between ΔP_{psl} and FN/FV or RoCoF, which does not exist based on the analysis in Chapter 2.2.2.

Moreover, a risk assessment matrix (RAM) can be formed based on the results in Fig. 2.11 to calculate the occurrence probability of the frequency instability risk, which are presented in Table 2.5 and Table 2.6, where ‘Red’, ‘Yellow’, and ‘Green’ region represent ‘High Risk’, ‘Medium Risk’, and ‘Low Risk’, separately [21]. The classification criterion used in Table 2.5 and Table 2.6 is according to the operational limit and statutory limit of frequency stability indices in the industry standard [140]. Results listed in the row of ‘MCS-DR’ are the occurrence probability of the frequency instability risk, while results listed in the row of rest methods are the absolute errors (AEs) between the occurrence probability calculated by different methods and that from MCS-DR. The mean absolute errors (MAEs) of different methods are shown in the last column to present the overall accuracy of different methods. The units of results shown in Table 2.5 and Table 2.6 are %.

Table 2.5 RAM in analyzing FN/FV in Case 1

FN/FV (Hz)		<49.5	49.5~49.8	49.8~50.2	50.2~50.5	>50.5	MAE
Area 1	MCS-DR	3.41	18.15	32.04	21.57	24.82	-
	CGCE	3.94	1.29	1.30	0.01	3.94	2.10
	PCE	0.86	0.88	0.68	1.29	0.63	0.87
	LRA	0.61	1.36	1.25	1.07	0.57	0.97
	MIS-MELRA	0.19	0.35	0.44	0.15	0.43	0.31
Area 2	MCS-DR	3.39	18.13	32.11	21.56	24.80	-
	CGCE	3.95	1.59	1.58	0.01	3.93	2.21
	PCE	0.87	0.88	0.64	1.26	0.63	0.87
	LRA	0.61	1.34	1.21	1.05	0.57	0.96
	MIS-MELRA	0.18	0.28	0.54	0.19	0.44	0.33
System	MCS-DR	3.34	18.06	32.26	21.59	24.74	-
	CGCE	4.01	1.53	1.41	0.03	3.86	2.16
	PCE	0.85	0.82	0.59	1.23	0.61	0.82
	LRA	0.65	1.31	1.11	1.02	0.57	0.93
	MIS-MELRA	0.18	0.26	0.55	0.20	0.44	0.33

Table 2.6 RAM in analyzing RoCoF in Case 1

RoCoF (Hz/s)		<-0.5	-0.5~-0.4	-0.4~0.4	0.4~0.5	>0.5	MAE
Area 1	MCS-DR	0.00	0.36	88.82	6.03	4.79	-
	CGCE	0.28	0.71	2.17	1.71	1.46	1.26
	PCE	0.81	1.03	5.32	0.25	3.24	2.13
	LRA	0.10	0.55	1.67	0.06	1.08	0.69
	MIS-MELRA	0.00	0.08	1.13	0.07	0.97	0.45
Area 2	MCS-DR	0.00	0.14	90.26	5.66	3.95	-
	CGCE	0.14	0.67	2.37	1.83	1.36	1.27
	PCE	0.37	0.46	3.12	0.41	1.90	1.25
	LRA	0.03	0.33	1.19	0.01	0.83	0.47
	MIS-MELRA	0.00	0.01	0.95	0.13	0.81	0.38
System	MCS-DR	0.00	0.06	91.43	5.24	3.27	-
	CGCE	0.09	0.57	2.09	1.65	1.10	1.10
	PCE	0.01	0.19	2.34	0.61	1.53	0.94
	LRA	0.02	0.24	1.48	0.15	1.07	0.59
	MIS-MELRA	0.00	0.02	0.86	0.13	0.71	0.34

From Table 2.5 and Table 2.6, the estimation error of MIS-MELRA is not the smallest at all levels. The reason is that the inaccuracy of other methods is mainly presented in the estimation of PDF at the middle region, while there are the stability ranges of frequency indices located at the tail of PDFs, which weakens the negative impact of the PDF estimation error on frequency stability risk assessment. Thus, it should be acknowledged that there exists a small possibility that the estimation error of MELRA may be slightly greater than those of other methods when the stability level of frequency indices is located at the tail of PDFs, and the interval of stability level is narrow, for example, 50.2~50.5Hz of FN/FV and 0.4~0.5Hz/s of RoCoF. However, even in this scenario, the AEs of MIS-MELRA are still small, with the maximal AE of 0.20%. And in the rest scenarios, the estimation errors of MELRA are the smallest. Moreover, from the perspective of overall accuracy, MIS-MELRA presents the highest accuracy in the risk assessment of both FN/FV and RoCoF with the maximal MAE of 0.45%. After MIS-MELRA, the accuracy of LRA is better than that of PCE, with the maximal MAE of 0.97% and 2.13%, respectively. And CGCE has the highest estimation errors. Additionally, it should be noted that a relatively high error of probabilistic frequency stability analysis may result in a conservative stability enhancement strategy, thereby increasing the reserve cost. Thus, estimation errors are expected to be as small as possible. Although all methods compared in the case studies have errors, according to the existing studies [21-24], the AE in estimating RAM is generally lower than 5%. By comparison, the estimation error of MIS-MELRA is lower than it, the accuracy of which is acceptable.

2.5.2 Case 2: Industrial Provincial Large-Scale Power System

To verify the performance of the proposed MIS-MELRA in the industrial large-scale power system, a practical provincial system at the East China is adopted. The practical system is divided into 2 areas according to the geographical location of power grids of 2 provinces, including 1958 buses, 840 loads, 56 SGs, 3260 branches, and 14 WPGs according to actual real-world data. The uncertainty parameters of WPGs and the structure diagram of the system are presented in Table 2.7 and Fig. 2.12, respectively.

Table 2.7 Parameters of uncertainties in Case 2

WPG No.	Control strategy	Parameters
W1, 2	Normal	*Weibull*(2.5, 4.5, 4), $\rho_{\xi_c}=0.7$
W3, 4	Normal	*Weibull*(2, 3, 3.5), $\rho_{\xi_c}=0.5$
W5, 6	VSG	*Weibull*(2.5, 4.5, 4), $\rho_{\xi_c}=0.7$
W7, 8	VSG	*Weibull*(2, 3, 3.5), $\rho_{\xi_c}=0.5$
W9, 10	Normal, VSG	*Weibull*(1.5, 2, 4)
W11, 12	Normal, VSG	*Weibull*(2, 5, 5)
W13, 14	Normal, VSG	*Weibull*(1.5, 3.5, 5)

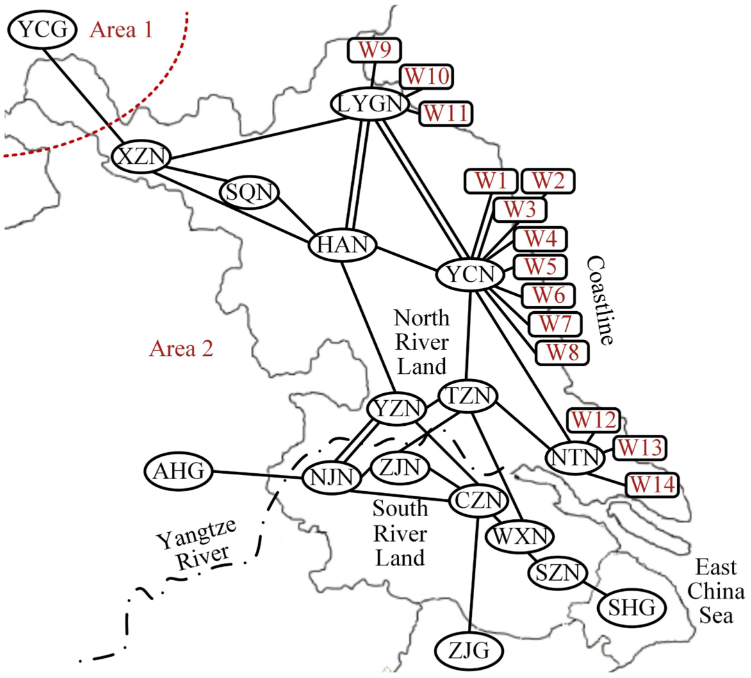

Fig. 2.12 Structure diagram of provincial large-scale power system.

The performance of the proposed MIS-MELRA is compared with CGCE, PCE with the sparse method and hyperbolic truncation (denoted as SPCE) [141], and LRA since conventional PCE encounters the curse of dimensionality in Case 2 due to the increase of uncertainty number compared with Case 1. Parameters are set to be the same as those in Case 1. The time costs of different methods in analyzing the frequency stability indices are compared in Table 2.8.

Table 2.8 Time comparison of different methods in analyzing FN/FV and RoCoF in Case 2

Time Index	t_S (s)	t_M (s)	t_T (s)
MCS-NDR	142537.66	-	142537.66
MCS-DR	150672.40	-	150672.40
CGCE	421.12	0.92	422.04
SPCE	6024.84	1.90	6026.74
LRA		0.74	6025.58
MIS-MELRA	850.93	4.83	855.76

In Table 2.8, the time costs of methods are similar to the results in Case 1. More specifically, CGCE is the most time-saving method. MIS-MELRA is the second. And due to the introduction of MIS, much simulation time is reduced in MIS-MELRA compared with LRA and SPCE. Moreover, t_M does not experience a significant increase with the rise of the uncertainty number. The results demonstrate the time-saving advantage of LRA-based methods in large-scale UPA. Additionally, it should be noted that there is an approximately proportional relationship between t_T of MIS-MELRA and N_U since $t_S \approx t_{SS} N_I N_U$ accounts for the major proportion of t_T, where t_{SS} is the time cost of a single simulation of the actual system. Thus, MIS-MELRA will cost more time than SPCE and LRA when $N_U > 100$. However, $N_U > 100$ is not common in the existing studies on probabilistic frequency stability analysis since it is a common practice that uncertainties are aggregated to reduce system complexity [6, 21-24]. Also, MIS for reducing the time cost and MELRA for improving the accuracy are separate methods. Even if $N_U > 100$, MELRA can be used individually to analyze probabilistic frequency stability with higher accuracy and almost the same time cost of SPCE and LRA.

Next, the PDFs of frequency stability indices are shown in Fig. 2.13. The shape differences of the corresponding PDFs are displayed in Table 2.9. Also, the RAM is formed based on the results in Fig. 2.13, presented in Table 2.10. Since the risk probability of RoCoF in the range of -0.4~0.4Hz/s is 100%, only the RAM of FN/FV is presented for saving space.

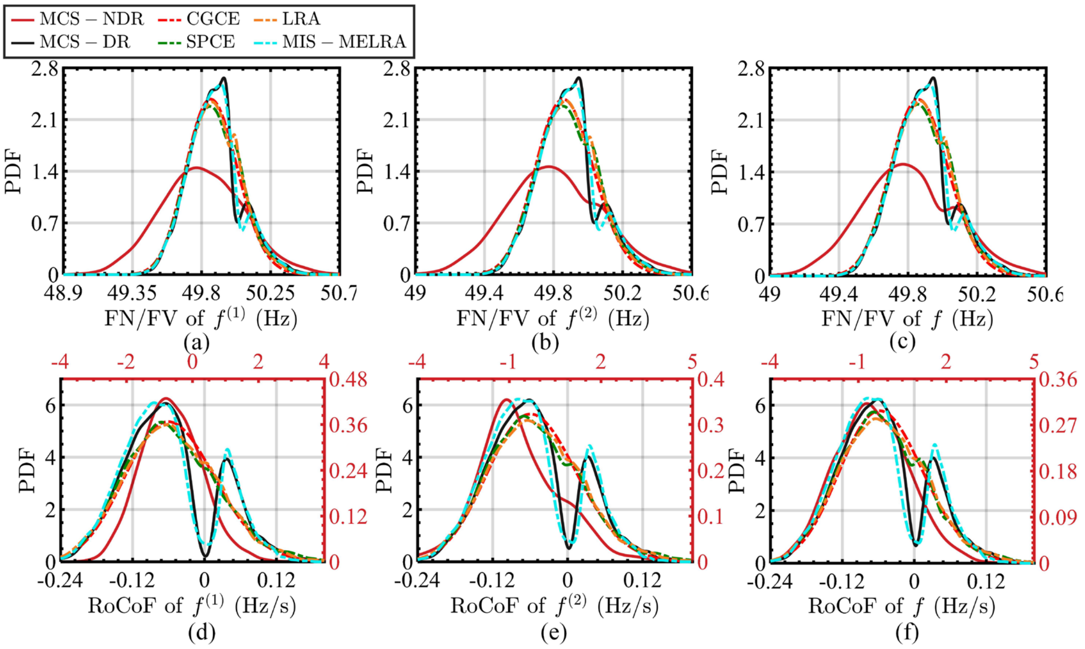

Fig. 2.13 PDF of FN/FV and RoCoF in Case 2: (a) FN/FV of Area 1; (b) FN/FV of Area 2; (c) FN/FV of system; (d) RoCoF of Area 1; (e) RoCoF of Area 2; (f) RoCoF of system.

Table 2.9 Performance of different methods in analyzing FN/FV and RoCoF in Case 2

Shape difference	$d_{F_{A1}}$	$d_{F_{A2}}$	$d_{F_{sys}}$	$d_{R_{A1}}$	$d_{R_{A2}}$	$d_{R_{sys}}$
CGCE	3.83	3.87	3.85	17.12	14.53	13.85
SPCE	3.64	3.77	3.66	10.03	8.47	8.10
LRA	3.60	3.41	3.41	10.56	9.07	8.45
MIS-MELRA	1.51	1.54	1.53	3.46	4.19	4.48

Table 2.10 RAM in analyzing FN/FV in Case 2

FN/FV (Hz)		<49.5	49.5~49.8	49.8~50.2	50.2~50.5	>50.5	MAE
Area 1	MCS-DR	0.53	31.16	63.62	4.62	0.08	-
	CGCE	0.38	1.86	0.45	1.73	0.06	0.90
	SPCE	0.20	0.86	0.24	0.77	0.05	0.42
	LRA	0.14	0.12	0.70	0.90	0.05	0.38
	MIS-MELRA	0.07	0.11	0.24	0.11	0.04	0.11
Area 2	MCS-DR	0.53	31.14	63.63	4.62	0.08	-
	CGCE	0.43	2.44	0.99	1.82	0.06	1.15
	SPCE	0.22	1.11	0.46	0.81	0.05	0.53
	LRA	0.11	0.13	0.74	0.93	0.05	0.39
	MIS-MELRA	0.07	0.02	0.16	0.12	0.04	0.08
System	MCS-DR	0.53	31.13	63.64	4.62	0.08	-
	CGCE	0.40	2.02	0.62	1.74	0.06	0.97
	SPCE	0.16	0.99	0.26	0.84	0.05	0.46
	LRA	0.11	0.14	0.74	0.92	0.05	0.39
	MIS-MELRA	0.07	0.05	0.18	0.11	0.04	0.09

From Fig. 2.13, there are significant differences between the PDFs obtained by MCS-NDR in both FN/FV and RoCoF and those from MCS-DR. Also, the PDFs calculated by MIS-MELRA have the highest similarity with the PDFs from MCS-DR in both FN/FV and RoCoF. After MIS-MELRA, the accuracy degrees of estimated

PDFs from SPCE and LRA are similar, and that of CGCE is the worst. Moreover, owing to the high PDF similarity, MIS-MELRA has the lowest estimation errors at all levels of frequency risk in RAM, as illustrated in Table 2.10. Regarding the overall accuracy, the maximal MAE of MIS-MELRA is 0.11%. By comparison, those of LRA, SPCE, and CGCE are 0.39%, 0.53%, and 1.15%, separately. Thus, the results indicate the high accuracy advantage of the proposed MIS-MELRA in large-scale UPA.

2.6 Summary

This chapter proposes methods of PFSA that consider the dynamics of RPGs with different control strategies. Firstly, the MIS method is proposed to simulate the frequency response, thereby significantly saving the simulation time. Then, the MELRA method for UPA suitable for large-scale uncertainty analysis is proposed. And the introduction of multi-element effectively improves the accuracy. In addition, by applying the GMM, the limitations of moment-based UPA methods are discussed, demonstrating the comparative superiority of the proposed method. Also, the necessity of considering the dynamics of RPGs in PFSA is revealed by analyzing the differences between frequency responses with and without dynamics of RPGs using different control strategies. The results of case studies demonstrate the effectiveness of the proposed methods.

Chapter 3 Probabilistic Frequency Stability Analysis Considering Wake Effects of Wind Farms

3.1 Introduction

Most existing studies on probabilistic frequency stability affected by WPG uncertainties ignore the heterogeneity and interactions of WTs inside WFs, i.e., WEs, which will lead to inaccurate results. This chapter proposes a method of PFSA considering the WEs of WFs. Also, an analytical WE model considering different factors and suitable for PFSA is proposed. Moreover, the impact of different factors on WEs and probabilistic frequency stability is studied.

3.2 Wake Effect Model of Wind Farm Considering Multiple Factors for Frequency Response

3.2.1 Wake Effect Model of Wind Farm Considering Multiple Factors

1) Basic WE Model

The WE of WT based on Gaussian WE model is shown in Fig. 3.1.

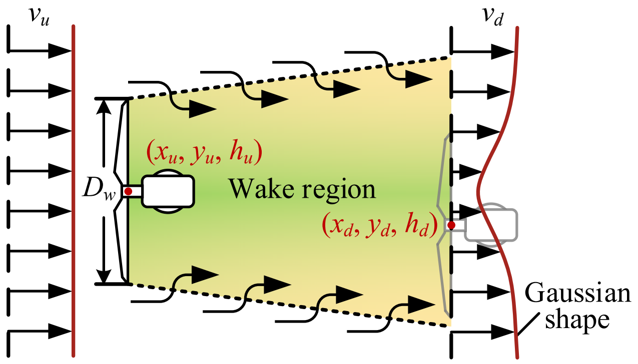

Fig. 3.1 WE of WT based on Gaussian WE model.

In Fig. 3.1, v_u is the incoming upstream wind speed. v_d is the downstream wind speed in the wind direction, which is lower than v_u due to the WE of WT. (x_u, y_u, h_u) and (x_d, y_d, h_d) are the positions of the upstream and indicated downstream WTs separately. D_w is the diameter of the upstream WT blade.

According to the mass and momentum conservation, there is

$$\int \rho v_u (v_u - v_d) dS = C_T \rho S_w v_u^2 / 2 \tag{3.1}$$

where ρ is the air density. S denotes the cross-sectional area of the wake. C_T is the thrust coefficient of the WT. S_w denotes the area swept by the WT blades, which has the following relationship with the cross-sectional area of the wake just after the initial wake expansion S_0 [53]

$$S_w = \alpha S_0 \tag{3.2}$$

where $\alpha = (1 + \sqrt{1 - C_T}) / (2\sqrt{1 - C_T})$.

The Gaussian WE model assumes that the wind speed deficit has a Gaussian shape [53]. Thus, the normalized downstream wind speed deficit d_w can be expressed as

$$d_w = (v_u - v_d) / v_u = g(x_d - x_u) e^{-\lambda} \tag{3.3}$$

where $\lambda = [(y_d - y_u)^2 + (h_d - h_u)^2] / (2D_w^2 \sigma_w^2)$. σ_w denotes the width of the wake.

$g(.)$ is the function of wind speed deficit at each downstream location at the center of the wake.

Thus, the downstream wind speed v_d can be expressed as

$$v_d = [1 - g(x_d - x_u)e^{-\lambda}]v_u. \tag{3.4}$$

Substituting (3.4) into (3.1), there is

$$8(\sigma_w / D_w)^2 g(x_d - x_u)^2 - 16(\sigma_w / D_w)^2 g(x_d - x_u) + C_T = 0. \tag{3.5}$$

Solving (3.5) and taking the solution in line with the actual situation, $g(.)$ can be derived as

$$g(x_d - x_u) = 1 - \sqrt{1 - C_T / [8(\sigma_w / D_w)^2]}. \tag{3.6}$$

Usually, the wake region is regarded as the linear expansion. Thus, σ_w / D_w can be expressed as

$$\sigma_w / D_w = k_w (x_d - x_u) + \varepsilon_w \tag{3.7}$$

where k_w is the wake region growth rate. $\varepsilon_w = 0.25\sqrt{\alpha}$ [53].

Substituting (3.6) and (3.7) into (3.4), v_d can be derived as

$$v_d = [1 - (1 - \sqrt{1 - C_T / \{8[k_w (x_d - x_u) + \varepsilon_w]^2\}})e^{-\lambda}]v_u. \tag{3.8}$$

2) Considering Terrain

In the basic Gaussian WE model, the impact of terrain is ignored. According to the Lissaman model [59], the nature wind speed varies at different heights, which can be described as

$$v'_{dn} / v_u = (h_d / h_u)^{\gamma} \tag{3.9}$$

where v'_{dn} is the nature wind speed at height h_d ignoring the terrain. γ is the coefficient of wind speed variation with height.

Also, according to the lossless Bernoulli equation, the relationship between the wind speed deficits corresponding to different wind speeds can be described as [54]

$$d_w / d_{wn} = (v'_{dn} / v_u)^2 \tag{3.10}$$

where d_{wn} is the normalized wind speed deficit corresponding to v'_{dn}.

Moreover, after considering the airflow of different terrains, the nature wind speed v_{dn} at height h_d can be expressed as [142]

$$v_{dn} = (1 + c_1 H / L e^{-c_2 h_d / L}) v'_{dn} \tag{3.11}$$

where H and L are the height and length of the terrain, separately. c_1 and c_2 are the airflow coefficients of different terrains.

Apart from the flat terrain, three complex terrains are included in this WE model, which can be formulated as [142]

$$h_c = \begin{cases} H / (1 + x_c^2 / L^2), \text{ Ridge} \\ He^{-\ln 2[x_c^2 + y_c^2]/L^2}, \text{Circular hill} \\ H[1 + \cos(\pi \sqrt{x_c^2 + y_c^2} / (2L))] / 2, \text{ Rolling terrain} \end{cases} \tag{3.12}$$

where (x_c, y_c, h_c) is a relative position from the terrain center.

Substituting (3.9)-(3.12) into (3.8), the WE considering the terrain can be expressed as

$$\begin{aligned} v_d = {} & [1 - (1 - \sqrt{1 - C_T / \{8[k_w(x_d - x_u) + \varepsilon_w]^2\}}) \cdot \\ & e^{-\lambda} (h_u / h_d)^{2\gamma}](h_d / h_u)^{\gamma} v_u . \end{aligned} \tag{3.13}$$

3) Considering Wind Direction

When the wind direction changes, the relative position of the WT changes, and the original upstream WT may become a downstream WT. Therefore, it is necessary to convert the relative position of the WT from its geographical location to its relative position along the wind direction. Assume that the angle between the wind direction and the positive direction of the x-axis on the x-y plane is θ_{xy}, and the angle between the wind direction and the positive direction of the y-axis on the y-h plane is θ_{yh}. The conversion between the position of WTs in the wind speed coordinate system $(x_{\cdot w}, y_{\cdot w}, h_{\cdot w})$ and the position in the geographic coordinate system $(x_{\cdot}, y_{\cdot}, h_{\cdot})$ is [50]

$$(x_{\cdot w}, y_{\cdot w}, h_{\cdot w}) = (x_{\cdot}, y_{\cdot}, h_{\cdot}) T_{yh} T_{xy} \tag{3.14}$$

where $T_{yh} = \begin{bmatrix} 1 & 0 & 0 \\ 0 & \cos\theta_{yh} & -\sin\theta_{yh} \\ 0 & \sin\theta_{yh} & \cos\theta_{yh} \end{bmatrix}$. $T_{xy} = \begin{bmatrix} \cos\theta_{xy} & -\sin\theta_{xy} & 0 \\ \sin\theta_{xy} & \cos\theta_{xy} & 0 \\ 0 & 0 & 1 \end{bmatrix}$.

Substituting (3.14) into (3.13), the WE considering the wind direction can be derived as

$$\begin{aligned} v_d = {} & [1 - (1 - \sqrt{1 - C_T / \{8[k_w(x_{dw} - x_{uw}) + \varepsilon_w]^2\}}) \cdot \\ & e^{-\lambda_w} (h_u / h_d)^{2\gamma}](h_d / h_u)^{\gamma} v_u \end{aligned} \tag{3.15}$$

where λ_w is λ calculated in the wind speed coordinate system.

4) Considering WEs of Multiple Upstream Wind Turbines

The above WE model only considers the WE of one upstream WT on the wind speed of downstream WT. In reality, all upstream WTs affect the downstream wind speed, and the downstream wind speed deficit is the superposition of the WEs of all upstream WTs, which can be described as [55]

$$v_d = v_{dn}\left(1 - \sqrt{\sum_{j=1}^{N_u} d_{wj}^2}\right) \tag{3.16}$$

where N_u is the number of upstream WTs.

Substituting (3.15) into (3.16), the WEs considering multiple upstream WTs can be derived as

$$v_d = v_{dn} - \sqrt{\sum_{j=1}^{N_u} \begin{array}{l} \{[(1-\sqrt{1-C_T / \{8[k_w(x_{dw}-x_{uwj})+\varepsilon_w]^2\}})\cdot \\ e^{-\lambda_{wj}}(h_{uj}/h_d)^{2\gamma}](h_d/h_{uj})^{\gamma} v_{uj}\}^2 \end{array}} \tag{3.17}$$

where λ_{wj} is the λ_w of j-th upstream WT.

5) Considering Time Delay of Wind Flow

Since WFs usually cover large geographic areas, it may take an unignorable time period for the wind to pass through WFs. If there is a wind speed change at time t from the upstream position, the downstream wind speed $v_d(t)$ will change correspondingly after a time delay τ rather than simultaneously. Thus, $v_d(t)$ is calculated based on the wind speed at $t-\tau$, and the time delay can be determined by the integral of the downstream distance divided by the wind speed, i.e., $\tau = \int_0^{x_{dw}} 1/v_d dx$ [50]. Thus, after considering the time delay of wind flow and WEs, the wind speed can be expressed as

$$v_d(t) = v_{dn}(t-\tau) - \sqrt{\sum_{j=1}^{N_u} \begin{array}{l} \{[(1-\sqrt{1-C_T / \{8[k_w(x_{dw}-x_{uwj})+\varepsilon_w]^2\}})\cdot \\ e^{-\lambda_{wj}}(\frac{h_{uj}}{h_d})^{2\gamma}](\frac{h_d}{h_{uj}})^{\gamma} v_{uj}(t-\tau)\}^2 \end{array}} . \tag{3.18}$$

3.2.2 System and Area-Level Frequency Response

In this chapter, WTs adopt PMSGs as examples. The power electronic-interfaced PMSG includes three parts: the PMSG, the MSC, and the GSC [33], as presented in Fig. 3.2(a). MSC and GSC controllers are shown in Fig. 3.2(b), where the droop control is flexibly equipped as the additional frequency regulation control for WTs. Also, the primary frequency regulation for SGs and automatic generation control (AGC) are considered [143], as shown in Fig. 3.2(c). The area-level frequency is determined by the frequency of SGs within the area, which can be calculated as [22]

$$f_{ai} = \sum_{q=1}^{N_g} H_{sq} f_{sq} / \sum_{q=1}^{N_g} H_{sq} \tag{3.19}$$

where f_{ai} is the frequency of the i-th area. N_g denotes the number of SGs in the i-th area. H_{sq} and f_{sq} are the inertia and frequency of the q-th SG, respectively.

From Fig. 3.2, the variation of nature wind speed will change the received wind speed of WTs in WFs in different degrees due to WEs, which will lead to the output power variations of WTs according to MPPT. Thus, the power imbalance will occur and result in the speed regulation of SGs, thereby affecting the frequency. Similarly, the system frequency f_{sys} is determined by the area-level frequency, which can be calculated as

$$f_{sys} = \sum_{i=1}^{N_a} H_{ai} f_{ai} / \sum_{i=1}^{N_a} H_{ai} \tag{3.20}$$

where N_a denotes the number of areas. H_{ai} and f_{ai} are the inertia and frequency of the i-th area respectively.

Additionally, from Fig. 3.2, the proposed WE model and the frequency response of power systems are calculated individually, where the WE model outputs are the inputs of the power system model. Thus, this WE model can be easily integrated into PFSA without any modifications to the power system model ignoring WEs.

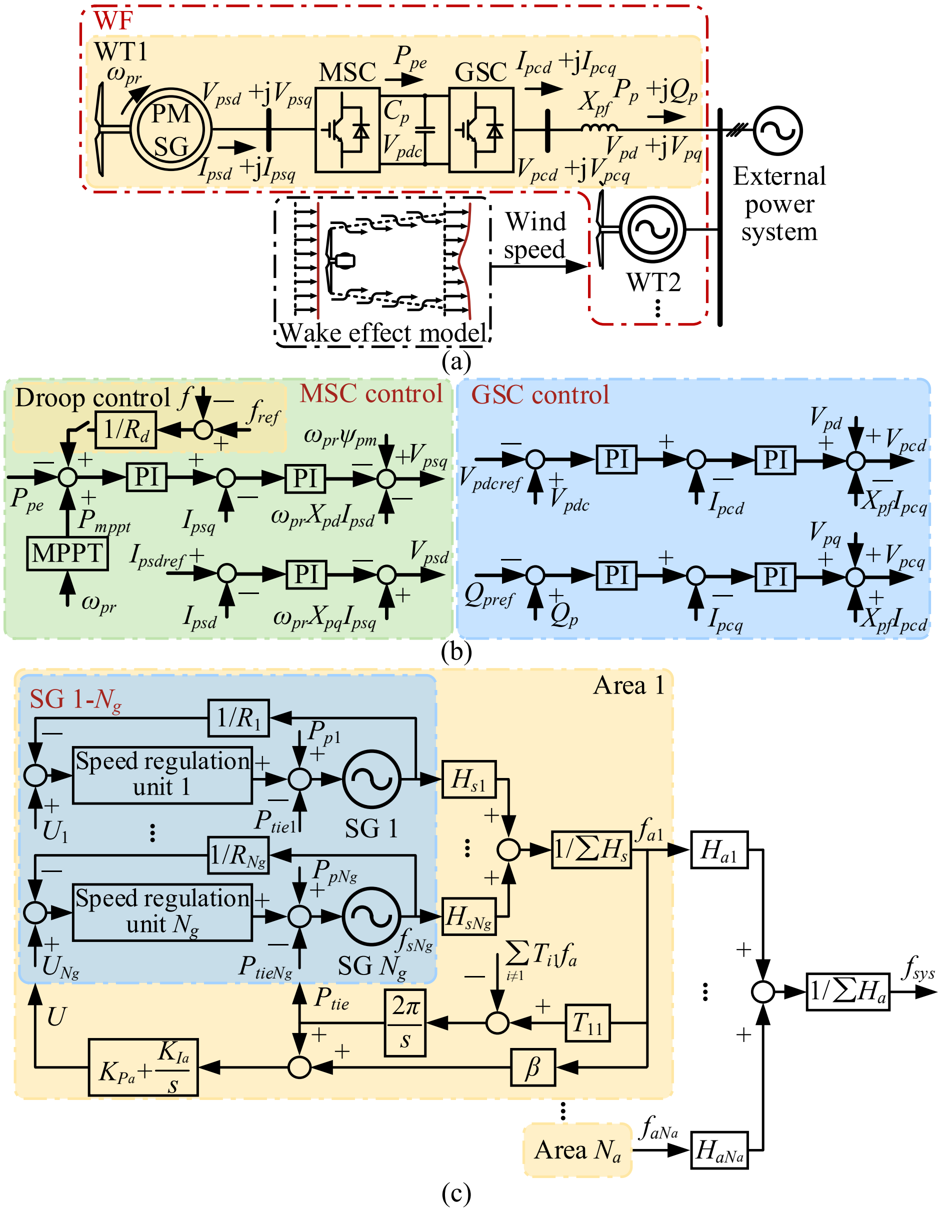

Fig. 3.2 (a) WF model; (b) Control strategy of WT; (c) System and area-level frequency response.

3.3 Multiple Output Gaussian Process Regression for Probabilistic Frequency Stability Analysis

3.3.1 Multiple Output Gaussian Process Regression

GPR-based UPA adopts a reduced model $\mathcal{M}(.)$ to describe the relationship between the uncertainties $\boldsymbol{\xi} = \{\xi_{lr}\}$ and the concerned system response $\boldsymbol{z} = \{z_{br}\}$, where ξ_{lr} is the r-th sampling point of l-th uncertainty, and z_{br} is the r-th observation point of b-th output, where $b = 1$ in conventional GPR. In this chapter, $\boldsymbol{\xi}$ is the wind speed, and $\boldsymbol{z}$ is the frequency stability index.

$$\boldsymbol{z} \approx \hat{\boldsymbol{z}} = \mathcal{M}(\boldsymbol{\xi}) + \boldsymbol{\varepsilon} \tag{3.21}$$

where superscript ^ denotes the estimated output by GPR-based method. $\boldsymbol{\varepsilon}$ is the error from the observation of $\boldsymbol{z}$, which follows Gaussian distribution $\boldsymbol{\varepsilon} \sim \mathcal{N}(\mathbf{0}, \sigma_{\varepsilon}^{2}\boldsymbol{I})$ with the standard deviation of σ_{ε}. $\boldsymbol{I}$ is the identity matrix. $\mathcal{M}(\boldsymbol{\xi})$ is the Gaussian process (GP) defined by the mean m and the covariance kernel function $\Bbbk(\boldsymbol{\xi}, \boldsymbol{\xi}; \boldsymbol{\theta})$ as [103]

$$\mathcal{M}(\boldsymbol{\xi}) \sim \mathcal{GP}(m, \Bbbk(\boldsymbol{\xi}, \boldsymbol{\xi}; \boldsymbol{\theta})) \tag{3.22}$$

where $\boldsymbol{\theta}$ are the parameters of the kernel function.

It should be noted that GP is used to characterize the sampling points of uncertainties and the observation points of the corresponding frequency stability index rather than uncertainties and corresponding frequency stability index themselves. Thus, GPR does not require that uncertainties and corresponding frequency stability index have to follow Gaussian distributions and is suitable for arbitrary distributions. It can be seen in (3.21) that conventional GPR has only one output. However, both system frequency and area-level frequency are concerned and need to be analyzed in probabilistic frequency stability. If conventional GPR is applied to analyze them, multiple GPR models will be built, which is time-consuming. Moreover, there are implicit relationships among system and area-level frequency responses. One of the obvious relationships is that the system frequency is the weighted average of area-level frequency, as shown in (3.20). However, building individual GPR models will not consider these relationships and may lead to inaccurate PFSA results. Thus, to quantify the probabilistic system frequency and area-level frequency simultaneously and characterize the implicit relationships among them, thereby improving accuracy and efficiency, MOGPR suitable for PFSA is designed.

1) Model Construction of MOGPR

Motivated by the combination relationship of frequency presented in (3.20), N_o outputs $\boldsymbol{\mathcal{M}}(\xi) = [\mathcal{M}_1(\xi), \cdots, \mathcal{M}_{N_o}(\xi)]^T$ are designed similarly to be formed by the combination of N_l latent factors $\boldsymbol{u}(\xi) = [u_1(\xi), \cdots, u_{N_l}(\xi)]^T \sim \mathcal{GP}(\boldsymbol{m}, \boldsymbol{k}(\xi, \xi; \boldsymbol{\theta}))$ modeled by GP as [144]

$$\begin{bmatrix} \mathcal{M}_1(\xi) \\ \vdots \\ \mathcal{M}_{N_o}(\xi) \end{bmatrix} = \begin{bmatrix} a_{11} & \cdots & a_{1N_l} \\ \vdots & \ddots & \vdots \\ a_{N_o 1} & \cdots & a_{N_o N_l} \end{bmatrix} \begin{bmatrix} u_1(\xi) \\ \vdots \\ u_{N_l}(\xi) \end{bmatrix} \tag{3.23}$$

where $a_\cdot$ is the element of coefficient matrix $\boldsymbol{A}$.

From (3.23), the connection of all outputs is established by the introduction of $\boldsymbol{u}(\xi)$, and the implicit relationship among outputs is reflected in $\boldsymbol{A}$. Thus, the proposed MOGPR for PFSA can reflect the relationship between the system frequency and the area-level frequency. Applying $\boldsymbol{a_n} = [a_{1n}, \cdots, a_{N_o n}]^T$ to represent the n-th column vector of $\boldsymbol{A}$, the covariance of outputs can be calculated as

$$\begin{aligned} \boldsymbol{C}(\xi, \xi) &= \mathbf{E}[\boldsymbol{\mathcal{M}}(\xi)\boldsymbol{\mathcal{M}}(\xi)^T] - \mathbf{E}[\boldsymbol{\mathcal{M}}(\xi)]\mathbf{E}^T[\boldsymbol{\mathcal{M}}(\xi)] \\ &= \sum_{n=1}^{N_l} \boldsymbol{a_n a_n^T} \otimes \{\mathbf{E}[u_n(\xi)u_n(\xi)] - \mathbf{E}[u_n(\xi)]\mathbf{E}[u_n(\xi)]\} \\ &= \boldsymbol{A}\boldsymbol{A}^T \otimes \boldsymbol{k}(\xi, \xi; \boldsymbol{\theta}) \end{aligned} \tag{3.24}$$

Thus, the joint prior distribution of the observed system outputs $\boldsymbol{Z}_s$ corresponding to the sampling points of uncertainties ξ_s and $\mathcal{M}(\xi_e)$ corresponding to the points of uncertainties to be analyzed ξ_e is

$$\begin{bmatrix} \boldsymbol{Z}_s \\ \mathcal{M}(\xi_e) \end{bmatrix} \sim \mathcal{N}\left(\begin{bmatrix} \boldsymbol{m}_s \\ \boldsymbol{m}_e \end{bmatrix}, \begin{bmatrix} AA^T \otimes \mathcal{K}_{ss} + \sigma_\varepsilon^2 \boldsymbol{I} & AA^T \otimes \mathcal{K}_{se} \\ AA^T \otimes \mathcal{K}_{es} & AA^T \otimes \mathcal{K}_{ee} \end{bmatrix} \right) \tag{3.25}$$

where $\boldsymbol{m}_s$ and $\boldsymbol{m}_e$ are the means corresponding to $\mathcal{M}(\xi_s)$ and $\mathcal{M}(\xi_e)$ respectively. $\mathcal{K}_{se}$ denotes $k(\xi_s, \xi_e; \boldsymbol{\theta})$.

Thus, the posterior mean $\boldsymbol{m}_{pe}$ and covariance $\mathcal{K}_{pee}$ of $\mathcal{M}(\xi_e)$ can be derived as

$$\begin{cases} \boldsymbol{m}_{pe} = \boldsymbol{m}_e + (AA^T \otimes \mathcal{K}_{es}) \cdot \\ \qquad (AA^T \otimes \mathcal{K}_{ee} + \sigma_\varepsilon^2 \boldsymbol{I})^{-1} (\boldsymbol{Z}_s - \boldsymbol{m}_s) \\ \mathcal{K}_{pee} = \mathcal{K}_{ee} - (AA^T \otimes \mathcal{K}_{es}) \cdot \\ \qquad (AA^T \otimes \mathcal{K}_{ee} + \sigma_\varepsilon^2 \boldsymbol{I})^{-1} (AA^T \otimes \mathcal{K}_{se}) \end{cases} . \tag{3.26}$$

2) Calculation of Undetermined Coefficients

According to (3.26), $\boldsymbol{\theta}$ and A are undetermined, which need to be calculated.

According to the Bayesian theorem, there is

$$p(\boldsymbol{\theta}, A \mid \boldsymbol{Z}_s, \xi_s) = p(\boldsymbol{Z}_s \mid \xi_s, \boldsymbol{\theta}, A) p(\boldsymbol{\theta}, A) / p(\boldsymbol{Z}_s \mid \xi_s) \tag{3.27}$$

where $p(\boldsymbol{\theta}, A \mid \boldsymbol{Z}_s, \xi_s)$ is the posterior probability of $\boldsymbol{\theta}$ and A. $p(\boldsymbol{Z}_s \mid \xi_s, \boldsymbol{\theta}, A)$ denotes the likelihood function. $p(\boldsymbol{\theta}, A)$ is the prior probability of $\boldsymbol{\theta}$ and A. $p(\boldsymbol{Z}_s \mid \xi_s)$ denotes the evidence.

The optimization of $\boldsymbol{\theta}$ and A is equivalent to maximizing $p(\boldsymbol{\theta}, A \mid \boldsymbol{Z}_s, \xi_s)$, i.e., maximum likelihood estimation. Since $p(\boldsymbol{Z}_s \mid \xi_s)$ is fixed when $\boldsymbol{Z}_s$ and ξ_s are given, and $p(\boldsymbol{\theta}, A)$ is known in advance, $p(\boldsymbol{\theta}, A \mid \boldsymbol{Z}_s, \xi_s)$ is proportional to $p(\boldsymbol{Z}_s \mid \xi_s, \boldsymbol{\theta}, A)$. For the convenience of calculation, the optimization objective $\mathcal{L}$ is transformed into minimizing the $-\log \mathcal{p}(\boldsymbol{Z}_s \mid \boldsymbol{\xi}_s, \boldsymbol{\theta}, \boldsymbol{A})$ as

$$\begin{aligned}
\mathcal{L} &= -\log \mathcal{p}(\boldsymbol{Z}_s \mid \boldsymbol{\xi}_s, \boldsymbol{\theta}, \boldsymbol{A}) \\
&= \boldsymbol{Z}_s^T (\boldsymbol{A}\boldsymbol{A}^T \otimes \boldsymbol{\mathcal{K}}_{ee} + \sigma_\varepsilon^2 \boldsymbol{I}) \boldsymbol{Z}_s / 2 \\
&\quad + \log | \boldsymbol{A}\boldsymbol{A}^T \otimes \boldsymbol{\mathcal{K}}_{ee} + \sigma_\varepsilon^2 \boldsymbol{I} | /2 + N_s \log 2\pi / 2
\end{aligned} \tag{3.28}$$

where N_s is the number of sampling points $\boldsymbol{\xi}_s$.

In summary, MOGPR $\boldsymbol{\mathcal{M}}(\boldsymbol{\xi}; \boldsymbol{\theta}, \boldsymbol{A})$ approximates the relationship between uncertainties and frequency stability indices with the sampling points of uncertainties as inputs and those of frequency stability indices as outputs in the form of (3.25), which is a regression task. To calculate the undetermined coefficients $\boldsymbol{\theta}$ and $\boldsymbol{A}$ in (3.25), maximum likelihood estimation is adopted, which can be transformed into minimizing (3.28). After $\boldsymbol{\theta}$ and $\boldsymbol{A}$ are calculated, MOGPR can be used to estimate frequency stability indices corresponding to the points of uncertainties to be analyzed $\boldsymbol{\xi}_e$, which are $\boldsymbol{\mathcal{M}}(\boldsymbol{\xi}_e; \boldsymbol{\theta}, \boldsymbol{A})$ with the highest probabilities, i.e., $\boldsymbol{m}_{pe}$, in the form of (3.26). Additionally, in this paper, L-BFGS is used to solve (3.28). And to improve the sampling efficiency, LHS [103] is applied to acquire $\boldsymbol{\xi}_s$.

3.3.2 Probabilistic Frequency Stability Analysis

In PFSA, the PDFs of frequency stability indices are primarily concerned. RoCoF FSI_R and FN/FV FSI_F are typical frequency stability indices, which are considered in this chapter as the example indices. And after the MOGPR is constructed, the data of estimated frequency stability indices $\boldsymbol{m}_{pe}$ when the system is under the sampling points of uncertainties $\boldsymbol{\xi}_s$ can be directly calculated according to (3.26). Then, to estimate the closed-form PDFs of frequency stability indices based on the data $\boldsymbol{m}_{pe}$, KDE [103] is adopted, which is a nonparametric method using the kernels corresponding to data as components to form PDFs and can be formulated as

$$p_{\hat{z}_b}(\hat{z}_b) = \sum_{r=1}^{N_e} p_K[(\hat{z}_b - m_{pebr}) / \delta_{Kb}] / (N_e \delta_{Kb}) \tag{3.29}$$

where N_e is the number of data $\boldsymbol{\xi}_e$. m_{pebr} denotes the r-th sampling point of $\boldsymbol{m}_{pe}$ corresponding to b-th output. $p_K[.]$ denotes the kernel function of KDE, which is selected as the Gaussian kernel, i.e., $p_K[(\hat{z}_b - m_{pebr}) / \delta_{Kb}] = e^{-(\hat{z}_b - m_{pebr})^2 / (2\delta_{Kb}^2)}$. δ_{Kb} is the bandwidth of kernels.

Moreover, apart from PDFs, the RAM [21] is also concerned in PFSA, which is used to assess the occurrence probability of the frequency instability risk. In this chapter, frequency stability risk regions are partitioned as 'Low Risk' marked in green, 'Medium Risk' marked in yellow, and 'High Risk' marked in red, according to the industry standard [140]. Based on the derived PDFs, the probability of the system in different risk regions $\Pr(.)$ can be estimated as

$$\Pr(\vartheta_{m\min} \le \hat{z}_b \le \vartheta_{m\max}) = \int_{\vartheta_{m\min}}^{\vartheta_{m\max}} p_{\hat{z}_b}(\hat{z}_b) d\hat{z}_b \tag{3.30}$$

where $\vartheta_{m\min}$ and $\vartheta_{m\max}$ are the upper and lower bounds of m-th risk region, respectively.

According to Chapter 3.2 and Chapter 3.3, the proposed PFSA method considering WEs of WFs can be summarized in Fig. 3.3.

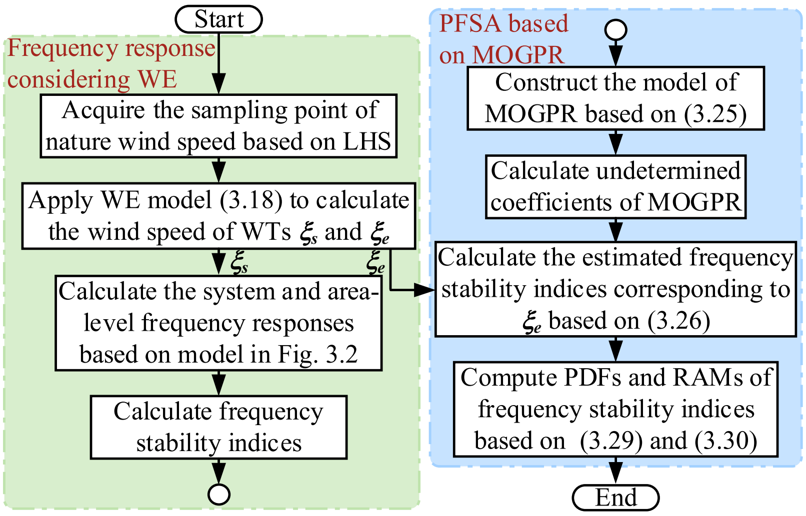

Fig. 3.3 Procedure of the proposed PFSA method considering WEs of WFs.

3.4 Case Study

3.4.1 Case 1: IEEE 68-Bus Benchmark System

1) Example System

Case 1 is conducted in the IEEE 68-bus benchmark system [22], where the power system dynamic models [33, 143], as presented in Fig. 2, are used. WTs are not equipped with additional frequency regulation control in Case 1 to show the obvious impact of WPG uncertainties on probabilistic frequency stability. Three WFs are integrated into the system, as illustrated in Fig. 3.4. 20 WTs are in each WF. The layout of WTs is set as 4×5 with the interval of 200m at the height of 50m. The wind direction is consistent with the positive direction of the x-axis of the geographical coordinate system. The initial nature wind speeds of WFs are 8m/s. The nature wind speeds change at 0.1s randomly [23]. AGC starts after 30s [145]. The uncertainties of the changed nature wind speeds obey the following probabilistic distribution: The nature wind speed of WF1 follows *Weibull*(2, 5, 3.5); Those of WF2 and WF3 follow *Weibull*(2.5, 4.5, 4) with the correlation coefficient of 0.7. The rest of the parameters are set as: WE parameters: C_T=0.42 , k_w=0.042 , h_d=50 m , $D_w = 40$ m , $\gamma = 0.143$; WT parameters (p.u.): $C_p = 10$, $X_{pf} = 0.02$, $X_{pd} = 0.2$, $X_{pq} = 0.2$, $I_{psdref} = 0$, $V_{dcref} = 1$; frequency regulation parameters (p.u.): $R_{\cdot} = 0.05$, $\beta = 0.416$, $T_{ij} = 0.2$, $K_{Pa} = 1$, $K_{Ia} = 0.5$. It should be noted that the proposed WE model and PFSA method are generic and suitable for both short-term and long-term studies. In this chapter, the widely-used Weibull function is selected for demonstration, which is usually used to quantify the uncertainty of the nature wind speed in long-term planning [22].

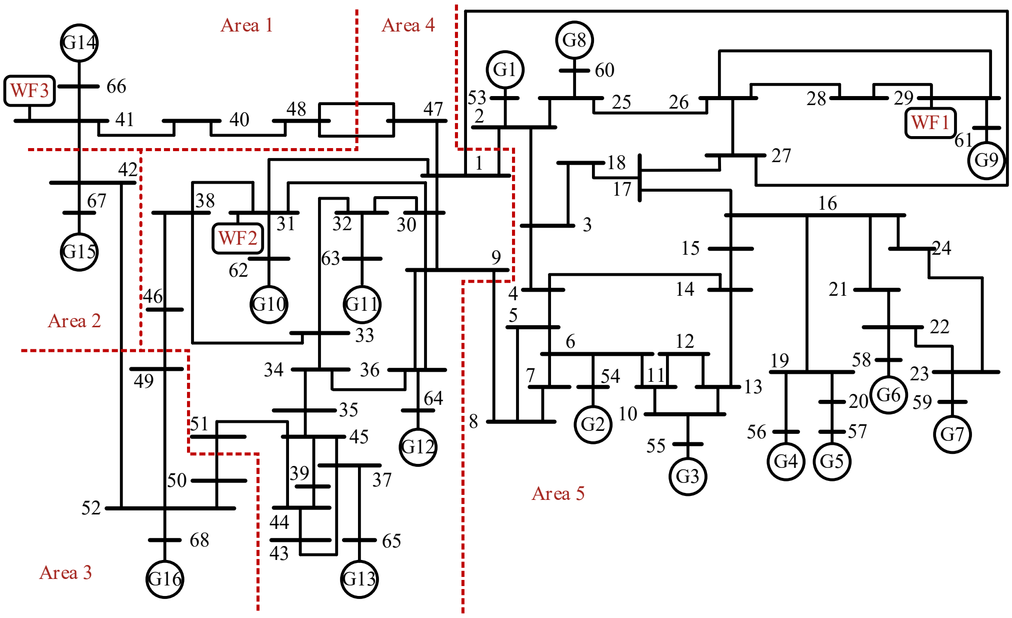

Fig. 3.4 IEEE 68-bus system integrated with three WFs.

2) Validation of Multiple Output Gaussian Process Regression for Probabilistic Frequency Stability Analysis Considering Wake Effects of Wind Farms

Firstly, the accuracy of the proposed WE model is verified by comparing it with the measurements, CFD, and Jensen and Gaussian analytical WE models presented in

Fig. 3.5, where the measurements and results of CFD are from [146].

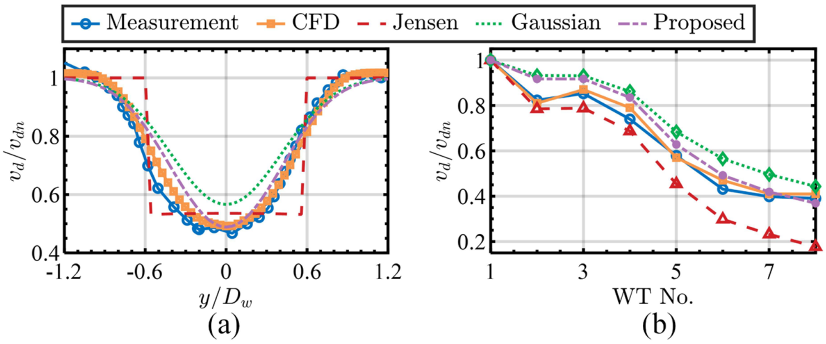

Fig. 3.5 Calculation results of WEs in the scenarios of [146]: (a) Single WT in Wieringermeer East; (b) WTs in Lillgrund WF.

From Fig. 3.5, compared with other analytical WE models, the results of the proposed model are closer to measurements, which demonstrates the accuracy of the proposed model. Although the results of the proposed model are less accurate than those of CFD, CFD is not suitable for PFSA since its simulation time is much greater than that of power systems. Additionally, it can be seen in Fig. 3.5(b) that the calculation errors of the proposed model associated with WTs located further along the wind direction are lower than those of WTs located closer. This observation does not mean that the proposed model has the higher accuracy for further WTs. And it is just caused by the possible occurrence of positive and negative error offset since there are both positive errors and negative errors when the proposed model is used to calculate the WE of one WT. For example, as shown in Fig. 3.5(a), positive error at $y/D_w = 1$ and negative error at $y/D_w = -0.4$. And the wind speed of the downstream WT is affected by WEs of all upstream WTs. Thus, calculation errors are accumulated. When errors with the opposite nature happen to be accumulated, the overall error may be very small.

To verify the effectiveness of the proposed MOGPR, MCS considering the WEs of WFs (denoted as MCS-WE) is conducted 5000 times [21], the results of which are regarded as the baseline. Also, MCS ignoring the WEs of WFs (denoted as MCS-NWE) [21] is carried out to demonstrate the impact of the WEs on probabilistic frequency stability. Moreover, the performance of the proposed MOGPR is compared with GPR. The Gaussian kernel is selected as the covariance kernel function, and the number of sampling data is chosen as 400 [103]. It should be noted that it is the first time to apply the GPR-based method in PFSA. Thus, both GPR and MOGPR are novel methods in PFSA. The time of frequency response simulation t_S, WE calculation time t_W, execution time of UPA methods t_M, and total time t_T are illustrated in Table 3.1.

Table 3.1 Time cost in analyzing FN/FV and RoCoF in Case 1

Time cost	t_S (s)	t_W (s)	t_M (s)	t_T (s)
MCS-NWE	191173.94	-	-	191173.94
MCS-WE	202927.13	257.28	-	203184.41
GPR	16233.77	20.70	26.63	16281.10
MOGPR	16234.42	20.54	8.32	16263.28

From Table 3.1, t_W is significantly less than t_S, which means that the proposed WE model only brings a slight rise of the computational time in PFSA and thus is suitable for PFSA. Also, MCS-based methods are quite time-consuming. By comparison, t_S of GPR-based methods is greatly shorter than that of MCS-based methods. Furthermore, since MOGPR can calculate the frequency stability indices of different areas simultaneously, t_M of MOGPR is shorter than that of GPR, which indicates the advantage of MOGPR in improving efficiency. Additionally, since the efficient scenario-based methods for analyzing the worst-case scenarios of power system frequency stability considering WPG uncertainties and WE are lacking, the worst-case scenarios need to be found from a large quantity of possible scenarios. Thus, the time cost of worst scenario (WS) selection nearly equals that of MCS.

Moreover, the PDFs of FN/FV and RoCoF are shown in Fig. 3.6 to verify the accuracy of the proposed method, where WSs are also drawn. To save space, only the results of Area1, Area2, and the system are presented.

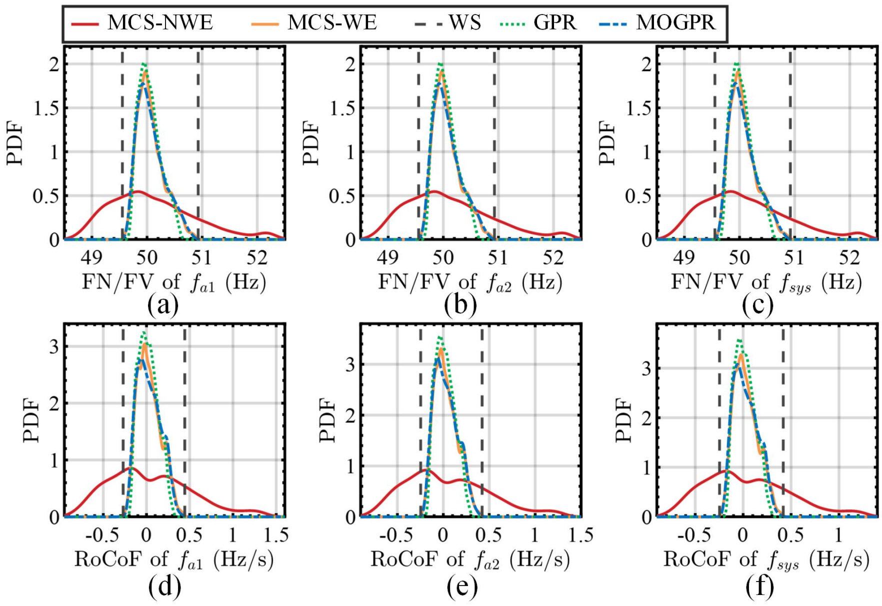

Fig. 3.6 PDF of FN/FV and RoCoF in Case 1: (a) FN/FV of Area 1; (b) FN/FV of Area 2; (c) FN/FV of system; (d) RoCoF of Area 1; (e) RoCoF of Area 2; (f) RoCoF of system.

As shown in Fig. 3.6, there are significant differences between the results from MCS-NWE and those from MCS-WE in both FN/FV and RoCoF, which indicates that ignoring the WEs of WFs in PFSA is inaccurate. The PDFs of FN/FV and RoCoF from MCS-NWE have fatter tails, which means FN/FV and RoCoF are more separated when ignoring the WEs of WFs, leading to a higher probability of frequency instability. To further illustrate the differences between considering and ignoring WEs, the wind speed of WF considering WEs and frequency responses when all nature wind speeds change to 7m/s as an example are drawn in Fig. 3.7.

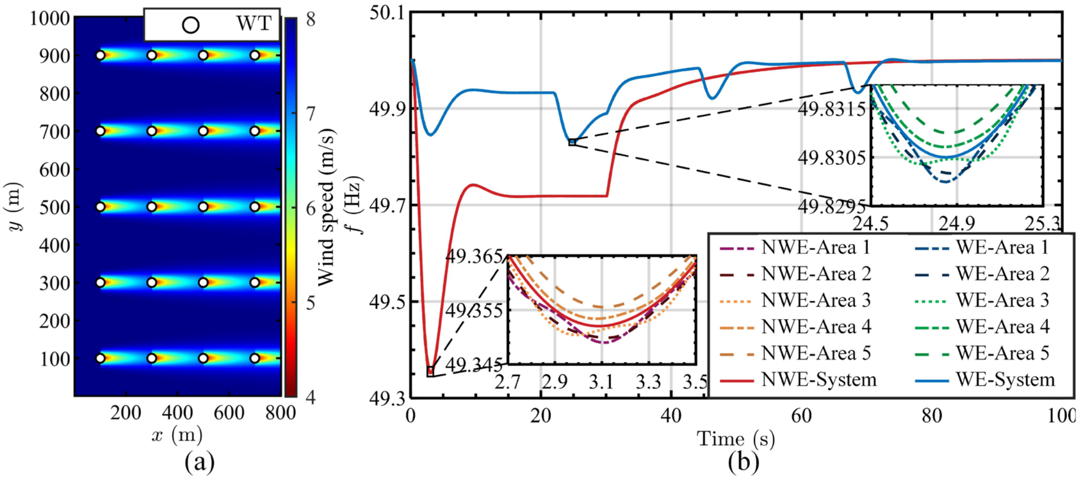

(a) (b)

Fig. 3.7 (a) Wind speed of WFs considering WEs; (b) Frequency trajectories affected by wind speed change.

From Fig. 3.7(a), there are wind speed deficits at downstream WTs when considering WEs, which results in smaller power fluctuations under the same changes of wind speed compared with those ignoring WEs. This contributes to a smaller frequency fluctuation, making the PDFs of FN/FV and RoCoF more concentrated. Moreover, from Fig. 3.7(b), due to the time delay of WEs, the change time points of wind speed of WTs at different positions are different, which also leads to PDFs of RoCoF being more concentrated. Thus, the results illustrate the significant impact of WEs on probabilistic frequency stability and demonstrate the necessity of considering the WEs of WFs in PFSA.

Moreover, to quantify the accuracy of different methods in calculating the PDFs of FN/FV and RoCoF presented in Fig. 3.6, the PDF shape difference $s_{\cdot}$ is introduced. It is defined as the Euclidean distance between the actual PDF $p_z(z)$ and the estimated PDF $p_{\hat{z}}(\hat{z})$, i.e., $\|p_z(z)-p_{\hat{z}}(\hat{z})\|$, as shown in Table 3.2. The subscript of $s_{\cdot}$ is the frequency stability index of the system and areas. For example, the FN/FV and RoCoF of frequency of Area a /system are denoted as F_{Aa}/F_{sys} and R_{Aa}/R_{sys}, respectively.

Table 3.2 Shape difference of PDFs of FN/FV and RoCoF in Case 1

Shape difference	$s_{F_{A1}}$	$s_{F_{A2}}$	$s_{F_{sys}}$	$s_{R_{A1}}$	$s_{R_{A2}}$	$s_{R_{sys}}$
GPR	2.02	2.01	2.01	4.08	4.18	4.18
MOGPR	1.01	1.02	1.02	2.14	1.72	2.23

From Table 3.2, the PDFs from MOGPR have the higher similarity with the PDFs from MCS-WE in both FN/FV and RoCoF, compared with those from GPR. The results indicate the high accuracy merit of the proposed MOGPR in calculating the PDFs of frequency stability indices. Moreover, from Fig. 3.6, although scenario-based WS selection gives the boundaries of frequency stability indices, it cannot reflect the probability of WSs, which is also concerned in probabilistic frequency stability, since preparing excessively for frequency violation scenarios with very low occurrence probabilities will greatly increase unnecessary reserve costs. By comparison, GPR and MOGPR use limited sampling points, i.e., scenarios, to build the corresponding models, thereby analyzing frequency stability of power systems in all possible scenarios. Also, the RAM can be formed based on the results in Fig. 3.6, as shown in Table 3.3, where ‘Green’, ‘Yellow’, and ‘Red’ regions denote ‘Low Risk’, ‘Medium Risk’, and ‘High Risk’, respectively. Results presented in the row of ‘MCS-WE’ are the risk occurrence probability of frequency. Results shown in the row of rest methods are the AEs between the risk occurrence probability from different methods and that from MCS-WE. To show the overall accuracy, the MAEs are listed in the last column. The units of results in Table 3.3 are %.

Table 3.3 RAM of FN/FV and RoCoF in Case 1

FN/FV (Hz)		<49.5	49.5~49.8	49.8~50.2	50.2~50.5	>50.5	MAE
Area 1	MCS-WE	0.00	11.05	62.23	19.38	7.33	-
	GPR	0.00	2.32	6.06	0.96	4.70	2.80
	MOGPR	0.00	0.83	2.12	0.66	0.63	0.85
Area 2	MCS-WE	0.00	11.02	62.27	19.37	7.34	-
	GPR	0.00	2.31	6.05	0.96	4.69	2.80
	MOGPR	0.00	0.83	2.12	0.67	0.62	0.84
System	MCS-WE	0.00	10.97	62.36	19.37	7.30	-
	GPR	0.00	2.21	6.14	0.90	4.68	2.80
	MOGPR	0.00	0.82	2.13	0.70	0.62	0.85
RoCoF (Hz/s)		<-0.5	-0.5~-0.4	-0.4~0.4	0.4~0.5	>0.5	MAE
Area 1	MCS-WE	0.00	0.00	99.70	0.30	0.00	-
	GPR	0.00	0.00	0.30	0.30	0.00	0.12
	MOGPR	0.00	0.00	0.13	0.13	0.00	0.05
Area 2	MCS-WE	0.00	0.00	99.86	0.14	0.00	-
	GPR	0.00	0.00	0.14	0.14	0.00	0.06
	MOGPR	0.00	0.00	0.04	0.04	0.00	0.02
System	MCS-WE	0.00	0.00	99.89	0.11	0.00	-
	GPR	0.00	0.00	0.11	0.11	0.00	0.04
	MOGPR	0.00	0.00	0.04	0.04	0.00	0.01

In Table 3.3, the risk occurrence probability of FN/FV is mainly concentrated in the low and medium-risk regions. The occurrence probability of high-risk regions is relatively low. The maximal AE of RAM of FN/FV from GPR is 6.14%, while that from MOGPR is 2.13%. And the maximal MAE of RAM of FN/FV from GPR is 2.80%, while that from MOGPR is 0.85%. The results indicate that the accuracy of MOGPR in analyzing the RAM of FN/FV is better than that of GPR. For RAM of RoCoF, the risk occurrence probability is mainly concentrated in the low-risk region, rarely in the medium-risk regions. The maximal AE from GPR is 0.30%, while that from MOGPR is 0.13%. And the maximal MAE from GPR is 0.12%, while that from MOGPR is 0.05%. Thus, the results demonstrate the high accuracy merit of the proposed MOGPR in analyzing the RAMs of frequency stability indices compared with GPR.

3) Impact of Different Factors on Probabilistic Frequency Stability

(1) Wind Direction

The angle between the wind direction and the positive direction of the x-axis is set as 30°, 45°, and 90°, respectively, to investigate the impact of wind direction on probabilistic frequency stability. Firstly, the accuracy of different methods in calculating PDFs of FN/FV and RoCoF and analyzing the RAM are shown in Table 3.4.

Table 3.4 Performance in analyzing FN/FV and RoCoF affected by wind direction

Shape difference		$s_{F_{A1}}$	$s_{F_{A2}}$	$s_{F_{sys}}$	$s_{R_{A1}}$	$s_{R_{A2}}$	$s_{R_{sys}}$
θ_{xy}=30°	GPR	2.58	2.58	2.57	8.18	7.91	8.22
	MOGPR	1.98	1.98	1.98	4.25	4.62	4.67
θ_{xy}=45°	GPR	2.85	2.83	2.81	5.47	5.47	5.67
	MOGPR	1.68	1.71	1.65	2.14	2.02	2.29
θ_{xy}=90°	GPR	2.33	2.32	2.32	4.76	4.94	4.82
	MOGPR	1.18	1.19	1.19	2.33	1.87	2.45
MAE		$e_{F_{A1}}$	$e_{F_{A2}}$	$e_{F_{sys}}$	$e_{R_{A1}}$	$e_{R_{A2}}$	$e_{R_{sys}}$
θ_{xy}=30°	GPR	2.17	2.17	2.17	0.00	0.00	0.00
	MOGPR	1.01	1.01	1.02	0.00	0.00	0.00
θ_{xy}=45°	GPR	3.03	3.02	3.01	0.00	0.00	0.00
	MOGPR	0.45	0.38	0.44	0.00	0.00	0.00
θ_{xy}=90°	GPR	1.89	1.89	2.88	0.00	0.00	0.00
	MOGPR	0.63	0.63	0.63	0.00	0.00	0.00

As shown in Table 3.4, the maximal PDF shape difference of FN/FV and RoCoF from GPR is 8.22, while that from MOGPR is 4.67. For the RAM results, the maximal MAE of FN/FV from GPR is 3.03%, while that from MOGPR is 1.02%. And the maximal MAE of RoCoF from both GPR and MOGPR is 0.00%, since the risk occurrence probability of the low-risk region is 100.00%. The results verify the accuracy of the proposed MOGPR in PFSA.

Moreover, the wind speed of WF at the height of 50m and RAM results are presented in Fig. 3.8 and Fig. 3.9 to show the impact of wind direction on probabilistic frequency stability. Since the risk probability of RoCoF in the low-risk region is 100.00%, only the RAMs of FN/FV are drawn in Fig. 3.9 to save space.

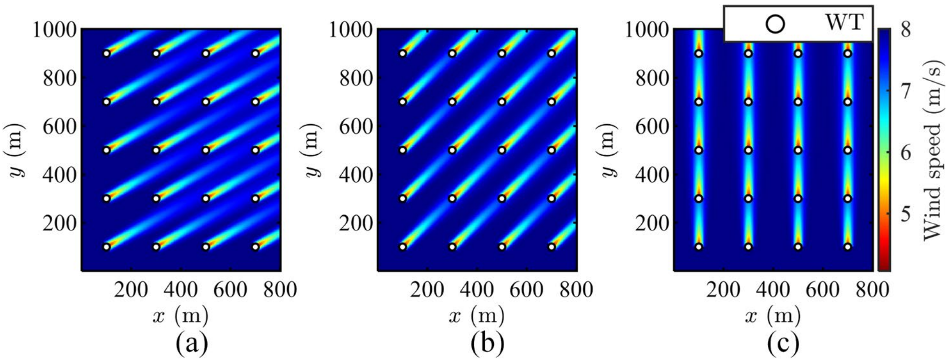

Fig. 3.8 WEs of WFs at different wind directions: (a) 30°; (b) 45°; (c) 90°.

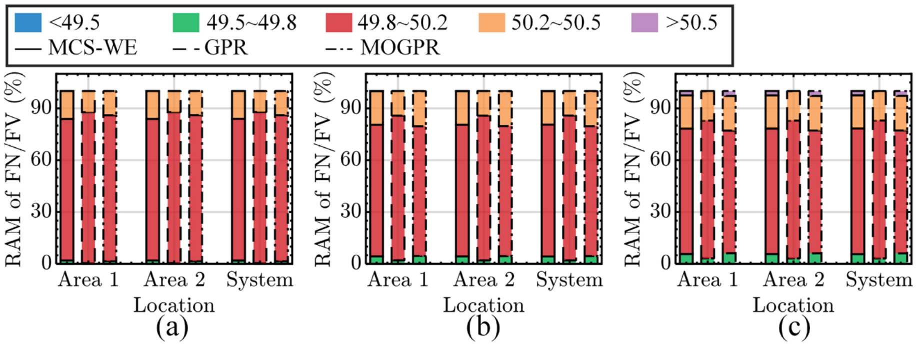

Fig. 3.9 RAM of FN/FV at different wind directions: (a) 30°; (b) 45°; (c) 90°.

From Fig. 3.8 and Fig. 3.9, the change of wind direction leads to the distance change of WTs in the wind direction. Taking the WT at the position (100, 100, 50) as an example, the nearest WTs directly below in the wind direction are the WT at (500, 300, 50) (approximately below when θ_{xy}=30°), the WT at (300, 300, 50) (when θ_{xy}=45°), and the WT at (300, 300, 50) (when θ_{xy}=90°), respectively. The streamwise distances are 446.41m, 282.84m, and 200m, separately. The wind speed deficit will increase with the rise of wind direction due to the rise of the WE strength. Under the same change of nature wind speed, before AGC starts, the number of WTs experiencing power fluctuations is most when θ_{xy}=90°, while that is least when θ_{xy}=30°. Thus, the risk occurrence probability of FN/FV is mainly in the low-risk region when θ_{xy}=30°. When θ_{xy}=45°, the probability in the low-risk region reduces, and the probability in medium-risk regions rises. And when θ_{xy}=90°, the risk occurrence probability of FN/FV is more separated, and there is the probability of being in the high-risk region.

(2) Terrain

The ridge, the circular hill, and the rolling terrain are involved in the case studies to study the impact of different terrains on probabilistic frequency stability. The terrain parameters of height and length are set as 50m and 150m. The accuracy of different methods, the wind speed of WF, and the RAM results are illustrated in Table 3.5, Fig. 3.10, and Fig. 3.11, separately.

Table 3.5 Performance in analyzing FN/FV and RoCoF affected by terrain

Shape difference		$s_{F_{A1}}$	$s_{F_{A2}}$	$s_{F_{sys}}$	$s_{R_{A1}}$	$s_{R_{A2}}$	$s_{R_{sys}}$
Ridge	GPR	2.99	2.99	2.99	5.22	5.36	5.46
	MOGPR	1.42	1.42	1.42	2.40	2.60	2.63
Circular hill	GPR	2.19	2.19	2.19	4.27	4.38	4.64
	MOGPR	0.70	0.71	0.71	1.70	1.65	1.77
Rolling terrain	GPR	2.29	2.29	2.29	4.65	4.70	4.88
	MOGPR	0.95	0.96	0.96	1.15	1.21	1.26
MAE		$e_{F_{A1}}$	$e_{F_{A2}}$	$e_{F_{sys}}$	$e_{R_{A1}}$	$e_{R_{A2}}$	$e_{R_{sys}}$
Ridge	GPR	4.19	4.18	4.17	0.79	0.36	0.32
	MOGPR	0.53	0.53	0.52	0.06	0.11	0.11
Circular hill	GPR	2.33	2.32	2.31	0.02	0.00	0.00
	MOGPR	1.08	1.08	1.08	0.01	0.00	0.00
Rolling terrain	GPR	2.79	2.78	2.77	0.00	0.00	0.00
	MOGPR	1.11	1.11	1.11	0.00	0.00	0.00

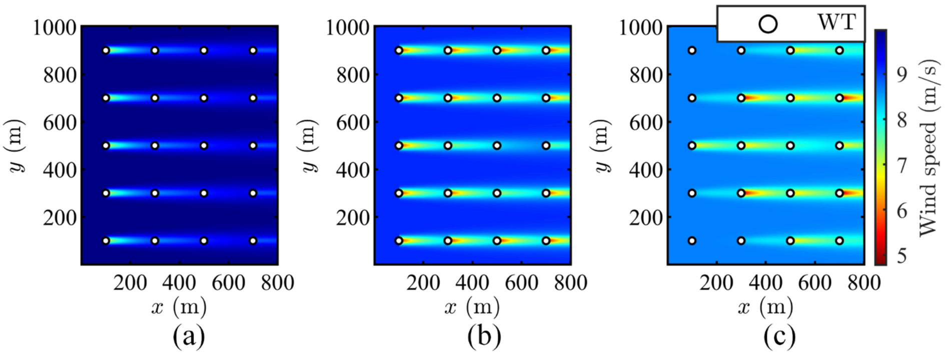

Fig. 3.10 WEs of WFs at different terrains: (a) Ridge; (b) Circular hill; (c) Rolling terrain.

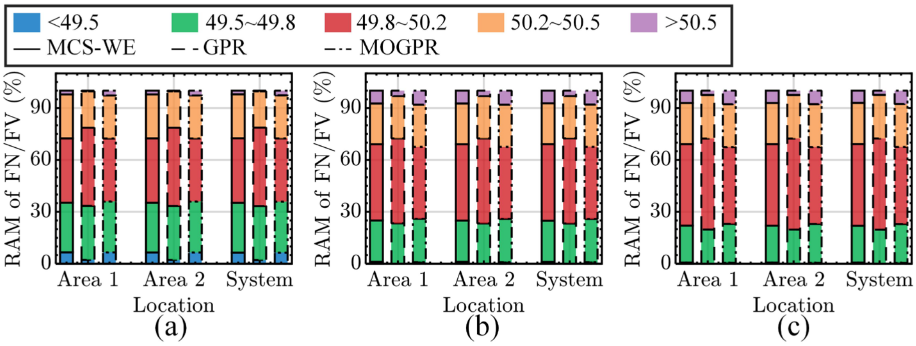

Fig. 3.11 RAM of FN/FV at different terrains: (a) Ridge; (b) Circular hill; (c) Rolling terrain.

According to Table 3.5, the PDF shape differences and the MAEs of RAM from MOGPR are lower than those from GPR, which indicates that the accuracy of MOGPR is higher than that of GPR. From Fig. 3.10 and Fig. 3.11, after considering different terrains, the level of nature wind speed and the WE strength are affected. In case studies, the wind speed deficit at the ridge is the smallest. And the level of nature wind speed at the ridge is the highest, while those at the circular hill and the rolling terrain are relatively low, which can be regarded as the difference of wind power penetration. Thus, when the wind speed changes, the power fluctuations of WTs are most obvious at the ridge. As a result, the risk occurrence probability of FN/FV is separated in different risk regions at the ridge. At the circular hill and the rolling terrain, the probability in high-risk and medium-risk regions reduces, and the probability in the low-risk region rises.

(3) Wind Turbine Layout

The position of WTs in every WF is changed to 2×10, 5×4, and the optimized layout with the objective of minimizing the unit generation cost [147], respectively, to demonstrate the impact of layout on probabilistic frequency stability. The accuracy of different methods, the wind speed of WF, and the RAM results are presented in Table 3.6, Fig. 3.12, and Fig. 3.13, separately.

Table 3.6 Performance in analyzing FN/FV and RoCoF affected by wind turbine layout

Shape difference		$s_{F_{A1}}$	$s_{F_{A2}}$	$s_{F_{sys}}$	$s_{R_{A1}}$	$s_{R_{A2}}$	$s_{R_{sys}}$
2×10	GPR	3.98	3.97	3.97	7.06	6.93	6.79
	MOGPR	1.99	2.00	2.00	3.08	3.15	3.21
5×4	GPR	2.33	2.32	2.32	4.76	4.94	4.82
	MOGPR	1.18	1.19	1.19	2.33	1.87	2.45
Optimized layout	GPR	2.26	2.26	2.24	5.95	6.06	6.52
	MOGPR	1.64	1.66	1.65	2.52	2.66	2.68
MAE		$e_{F_{A1}}$	$e_{F_{A2}}$	$e_{F_{sys}}$	$e_{R_{A1}}$	$e_{R_{A2}}$	$e_{R_{sys}}$
2×10	GPR	0.97	0.97	0.97	0.00	0.00	0.00
	MOGPR	0.59	0.68	0.59	0.00	0.00	0.00
5×4	GPR	2.89	2.89	2.88	0.00	0.00	0.00
	MOGPR	0.63	0.63	0.63	0.00	0.00	0.00
Optimized layout	GPR	2.14	2.14	2.12	0.00	0.00	0.00
	MOGPR	0.81	0.83	0.81	0.00	0.00	0.00

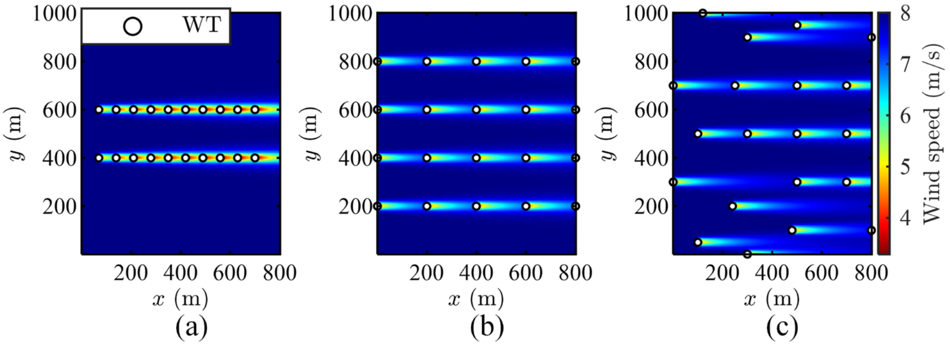

Fig. 3.12 WEs of WFs with different layouts: (a) 2×10; (b) 5×4; (c) Optimized layout.

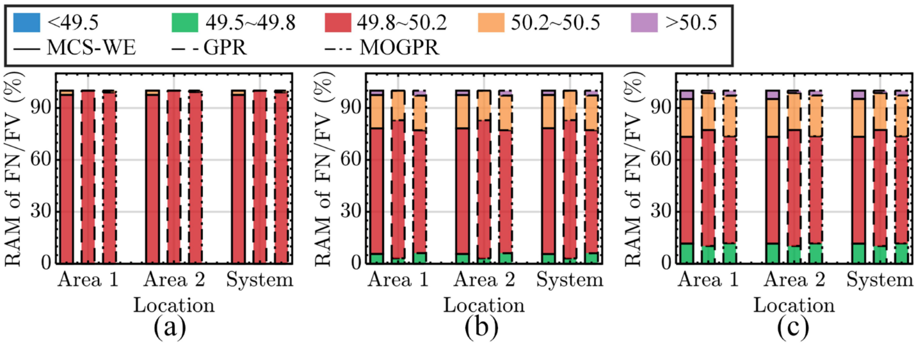

Fig. 3.13 RAM of FN/FV with different layouts: (a) 2×10; (b) 5×4; (c) Optimized layout.

Results in Table 3.6 show that both the PDF shape differences and the MAEs of RAM from MOGPR are lower than those from GPR. Based on Fig. 3.12 and Fig. 3.13, different layouts change the relative position of WTs, thereby changing the strength of the WEs in WFs, which results in more wind speed deficits, as illustrated in Fig. 3.12, and less conspicuous power fluctuations of WTs with a narrower layout. Thus, the risk occurrence probability of FN/FV is almost all in the low-risk region with 2×10 layout due to the high WE strength. When the layout is separated, since the WE strength is low, the probability in the low-risk region reduces, that in medium-risk regions increases, and even that in high-risk regions occurs.

It should be noted that though the wind direction, terrain, and WT layout are independent factors with different properties, i.e., meteorological, geographical, and operational planning factors, respectively, their impacts on WEs and probabilistic frequency stability are not independent. The reason is that the relative distance between WTs directly affects WEs and then probabilistic frequency stability. And any one of these three factors can affect the relative distance. Thus, though the change of one factor will not contribute to the change of another factor, it will affect the impact of another factor on WEs and probabilistic frequency stability. Since their impacts on WEs and probabilistic frequency stability are interwoven with each other, the impact analysis of individual factors is beneficial for revealing the general patterns of their impacts.

3.4.2 Case 2: Industrial Provincial Large-Scale Power System

1) Example System

Case 2 is conducted in a large-scale power system modified based on the realistic two-area system in East China, including 1958 buses and 56 generators, to demonstrate the scalability of the proposed method. Five WFs are integrated into the system, as presented in Fig. 14, where WF1, WF2, and WF5 are onshore. And WF3 and WF4 are offshore. The nature wind speeds of WF1 and WF2 follow *Weibull*(2.5, 4.5, 4) with the correlation coefficient of 0.7. Those of WF3, WF4, and WF5 follow *Weibull*(2, 5, 3.5), *Weibull*(1.5, 2, 4), and *Weibull*(1.5, 3.5, 5), respectively. The rest settings of WFs, MCS, GPR, and MOGPR are the same as those in Case 1.

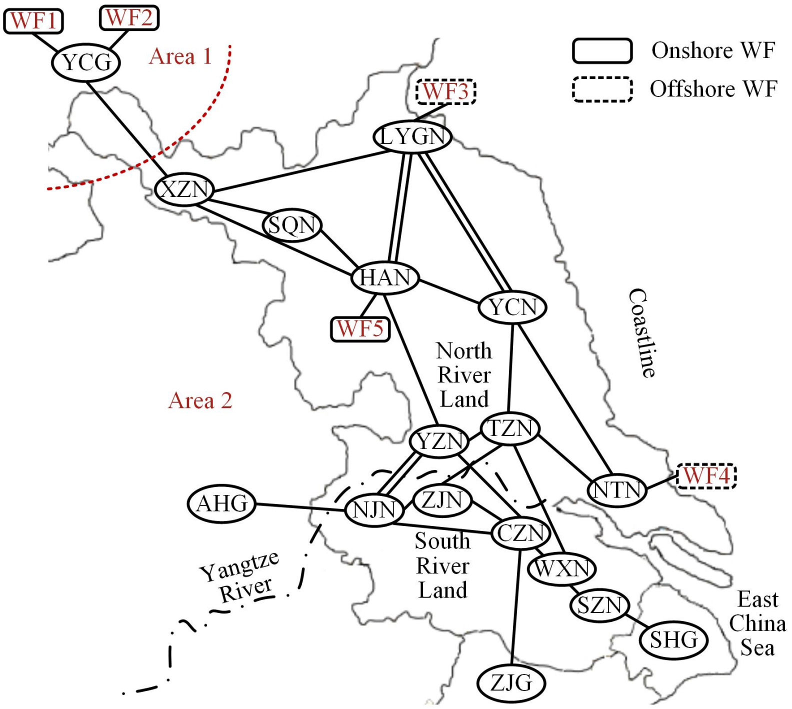

Fig. 3.14 Large-scale power system integrated with five WFs.

2) Scenario 1: Probabilistic Frequency Stability Analysis Considering Wake Effects of Wind Farms Without Additional Frequency Regulation Control

Firstly, the case study is carried out under the scenario that WFs are not equipped with additional frequency regulation control. And the time costs of different methods in conducting PFSA are listed in Table 3.7.

Table 3.7 Time cost in analyzing FN/FV and RoCoF in Scenario 1 Case 2

Time cost	t_S (s)	t_W (s)	t_M (s)	t_T (s)
MCS	692876.29	430.71	-	693307.00
GPR	55428.08	34.55	13.35	55475.98
MOGPR	55428.73	34.64	3.89	55467.26

From Table 3.7, similar observations as those in Case 1 can be obtained, i.e., the total time costs of GPR and MOGPR are significantly lower than that of MCS, and the execution time of MOGPR is shorter than that of GPR due to the multi-output structure.

Also, since the system in Case 1 has 5 areas, whereas that in Case 2 has 2 areas, the number of analyzed frequency stability indices in Case 2 is fewer than that in Case 1. Thus, the execution time of GPR and MOGPR in Case 2 is shorter than that in Case 1.

Next, the PDFs of frequency stability indices calculated based on different methods are presented in Fig. 3.15, where WSs are also drawn. And the shape differences of PDFs are computed to assess the accuracy of different methods in calculating PDFs, as illustrated in Table 3.8. Also, RAM derived from the results shown in Fig. 3.15 are listed in Table 3.9. Since the probability of RoCoF in the low-risk region is 100%, and all methods obtain the same results, only the RAM results of FN/FV are presented for saving space.

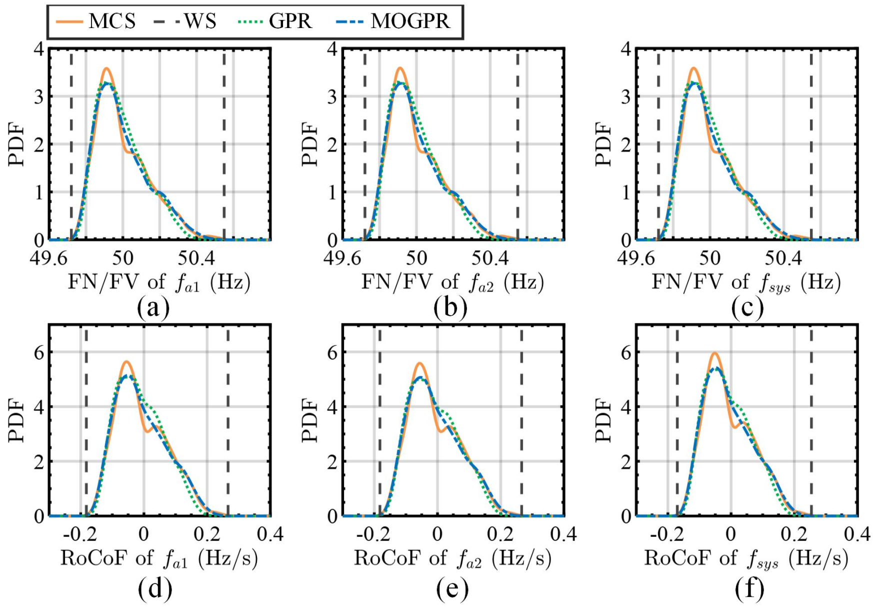

Fig. 3.15 PDF of FN/FV and RoCoF in Scenario 1 Case 2: (a) FN/FV of Area 1; (b) FN/FV of Area 2; (c) FN/FV of system; (d) RoCoF of Area 1; (e) RoCoF of Area 2; (f) RoCoF of system.

Table 3.8 Shape difference of PDFs of FN/FV and RoCoF in Scenario 1 Case 2

Shape difference	$s_{F_{A1}}$	$s_{F_{A2}}$	$s_{F_{sys}}$	$s_{R_{A1}}$	$s_{R_{A2}}$	$s_{R_{sys}}$
GPR	2.38	2.39	2.39	4.04	3.31	3.58
MOGPR	1.58	1.59	1.59	2.52	2.52	2.59

Table 3.9 RAM of FN/FV in Scenario 1 Case 2

FN/FV (Hz)		<49.5	49.5~49.8	49.8~50.2	50.2~50.5	>50.5	MAE
Area 1	MCS-WE	0.00	3.27	85.72	10.79	0.22	-
	GPR	0.00	1.04	3.84	2.61	0.19	1.53
	MOGPR	0.00	0.15	0.46	0.77	0.15	0.30
Area 2	MCS-WE	0.00	3.22	85.85	10.72	0.21	-
	GPR	0.00	1.03	3.83	2.62	0.19	1.54
	MOGPR	0.00	0.15	0.45	0.75	0.15	0.31
System	MCS-WE	0.00	3.22	85.81	10.75	0.22	-
	GPR	0.00	1.04	3.84	2.61	0.19	1.53
	MOGPR	0.00	0.15	0.46	0.76	0.15	0.30

By comparing the results in Table 3.8 with those in Table 3.2, though the system in Case 2 is much larger than those in Case 1 and with more uncertainties, the accuracy of the proposed method in calculating the PDFs of frequency stability indices in Case 2 is close to that in Case 1. Moreover, the RAM results in Case 2, as illustrated in Table 3.9, also demonstrate the high accuracy of MOGPR, with 0.31% maximal MAE. These results indicate the scalability of MOGPR in analyzing large-scale power systems with more uncertainties considering both onshore and offshore WFs and WEs.

3) Scenario 2: Probabilistic Frequency Stability Analysis Considering Wake Effects of Wind Farms with Additional Frequency Regulation Control

It can be seen in Table 3.9 that FN/FV has the probability to be in the medium-risk and even high-risk regions when there is no frequency regulation control in WFs. Thus, to improve the probabilistic frequency stability of the system, additional frequency regulation control is equipped in Scenario 2. And different methods are adopted to conduct PFSA in this scenario. The comparison of time costs, FN/FV PDFs, shape difference of FN/FV PDFs, and the RAM of FN/FV among different methods are presented in Table 3.10, Fig. 3.16, Table 3.11, and

Table 3.12, separately.

Table 3.10 Time cost in analyzing FN/FV and RoCoF in Scenario 2 Case 2

Time cost	t_S (s)	t_W (s)	t_M (s)	t_T (s)
MCS	692897.42	431.03	-	693328.45
GPR	55430.76	34.62	13.30	55478.68
MOGPR	55431.28	34.59	3.91	55469.78

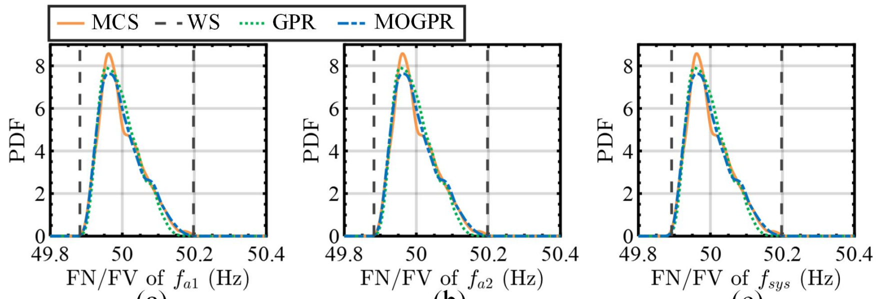

(a) (b) (c)

Fig. 3.16 PDF of FN/FV and RoCoF in Scenario 2 Case 2: (a) FN/FV of Area 1; (b) FN/FV of Area 2; (c) FN/FV of system.

Table 3.11 Shape difference of FN/FV PDFs in Scenario 2 Case 2

Shape difference	$s_{F_{A1}}$	$s_{F_{A2}}$	$s_{F_{sys}}$
GPR	3.67	3.69	3.69
MOGPR	2.55	2.56	2.56

Table 3.12 RAM of FN/FV in Scenario 2 Case 2

FN/FV (Hz)		<49.5	49.5~49.8	49.8~50.2	50.2~50.5	>50.5	MAE
Area 1/ Area 2/ System	MCS-WE	0.00	0.00	100.00	0.00	0.00	-
	GPR	0.00	0.00	0.00	0.00	0.00	0.00
	MOGPR	0.00	0.00	0.00	0.00	0.00	0.00

According to the results, the time costs and errors of MOGPR are close to those in Scenario 1, which demonstrates MOGPR is applicable for PFSA of power systems integrated with WFs with additional frequency regulation control. Moreover, by comparing Table 3.9 with

Table 3.12, after applying additional frequency regulation control, the probability of FN/FV in the medium-risk and high-risk regions is greatly reduced to 0%, and FN/FV only exists in the low-risk region. The results illustrate that applying additional frequency regulation control in WFs can effectively enhance the probabilistic frequency stability of power systems affected by WPG uncertainties.

3.5 Summary

This chapter proposes a method of PFSA considering the WEs of WFs based on the proposed WE model. Firstly, an analytical WE model suitable for PFSA is proposed. The proposed time-saving WE model can be easily integrated into the frequency response model of power systems and comprehensively considers multiple types of terrain, wind direction, and time delay of wind flow, reflecting the WEs of WFs more realistically. Then, for analyzing the system frequency and the area-level frequency simultaneously and considering the implicit relationship between them, the MOGPR is proposed to improve efficiency and accuracy. The results of case studies verify the effectiveness of the proposed method and demonstrate the necessity of considering the WEs of WFs in PFSA. And the impact of wind direction, terrain, and layout on probabilistic frequency stability is also investigated.

Chapter 4 Probabilistic Frequency Stability Analysis Aiming at Frequency Response Trajectories

4.1 Introduction

Existing PCE-based PFSA methods aiming at system dynamic responses require that joint probability distributions of uncertainties can be accurately characterized or approximated by existing Copula functions when dealing with correlated uncertainties. Also, since existing PCE-based PFSA methods have only one output, they can only estimate the frequency response at each time point separately. However, PFSA for power system frequency responses focuses on the frequency response trajectories at all time points during the concerned period of time. This means that massive PCE models need to be constructed, which is cumbersome. Thus, they are time-consuming and have limited accuracy. In view of this background, this chapter proposes a generic correlation transformation method for uncertainties with complicated correlations and GMPCE to quantify the system frequency response at each time point simultaneously.

4.2 Generic Multi-Output Polynomial Chaos Expansion for Probabilistic Frequency Stability Analysis Aiming at Frequency Response Trajectories

The proposed GMPCE utilizes weight summation of orthogonal polynomials to approximate the relationship $\boldsymbol{M}(\boldsymbol{\xi})$ between independent uncertainties $\boldsymbol{\xi}$ and the system response $\boldsymbol{y} = [y(\Delta t), \cdots, y(i\Delta t), \cdots, y(T_d)]^T$, which can be expressed as

$$\begin{aligned} \boldsymbol{y} &= \boldsymbol{M}(\boldsymbol{\xi}) \approx \hat{\boldsymbol{y}} = \hat{\boldsymbol{M}}(\boldsymbol{\xi}) = \boldsymbol{W}\boldsymbol{\varphi}(\boldsymbol{\xi}) \\ &= [\sum_{j=1}^{N_g} \boldsymbol{\omega}_{1j}\varphi_j(\boldsymbol{\xi}), \cdots, \sum_{j=1}^{N_g} \boldsymbol{\omega}_{ij}\varphi_j(\boldsymbol{\xi}), \cdots, \sum_{j=1}^{N_g} \boldsymbol{\omega}_{N_y j}\varphi_j(\boldsymbol{\xi})]^T \end{aligned} \tag{4.1}$$

where T_d denotes the concerned system response duration. Δt is the step length. N_g is the number of expansion items. $N_y = T_d / \Delta t$ is the number of GMPCE outputs $\boldsymbol{y}$. Superscript ^ represents the approximation derived from GMPCE. $\varphi_j(\boldsymbol{\xi})$ is the *j*-th item of $\boldsymbol{\varphi}(\boldsymbol{\xi})$, which denotes the polynomial and is arranged in ascending order. $\boldsymbol{\omega}_{ij}$ is the entry in *i*-th row and *j*-th column of the weight coefficient matrix $\boldsymbol{W}$.

From (4.1), one of the major differences between the form of GMPCE and that of existing PCE is that GMPCE has multiple outputs, while existing PCE has one output. Also, according to (4.1), the main tasks of deriving the GMPCE model can be summarized as: 1) Transformation of correlated uncertainties into independent ones $\boldsymbol{\xi}$; 2) Construction of polynomials $\boldsymbol{\varphi}(\boldsymbol{\xi})$; 3) Calculation of weight coefficients $\boldsymbol{W}$. It should be noted that $\boldsymbol{W}$ is directly derived in GMPCE as a whole rather than calculating $\boldsymbol{\omega}_{i.}$ separately and combining them into $\boldsymbol{W}$. Otherwise (4.1) is only a combination of existing PCE models.

4.2.1 Generic Transformation for Correlated Uncertainties

There are similarities between uncertainty transformation and blind source separation. In detail, correlated uncertainties are similar to the observed and mixed signals in blind source separation. And transforming correlated uncertainties into independent ones is similar to restoring the observed signals to the original signals. Thus, methods of blind source separation have the potential to be used in uncertainty transformation. And the basic idea of independent component analysis (ICA) that can effectively separate mixed signals into not only uncorrelated but also independent signals is applied in this chapter.

For a set of correlated uncertainties $\boldsymbol{\varsigma}=[\varsigma_1, \varsigma_2, \cdots, \varsigma_{N_c}]$, where N_c denotes the number of correlated uncertainties, the N_s sampling data of $\boldsymbol{\varsigma}$ is expressed as $\boldsymbol{\varsigma}^{(1\sim N_s)}$. Firstly, whitening processing is conducted to transform the correlated uncertainties into uncorrelated ones $\tilde{\boldsymbol{\varsigma}}$ with unit variance based on eigenvalue decomposition, which can be formulated as

$$\tilde{\boldsymbol{\varsigma}}^{(1\sim N_s)} = \boldsymbol{U}\boldsymbol{S}^{-1/2}\boldsymbol{U}^T\boldsymbol{\varsigma}^{(1\sim N_s)} \tag{4.2}$$

where $\boldsymbol{U}$ is the right eigenvector of $\boldsymbol{\varsigma}^{(1\sim N_s)}[\boldsymbol{\varsigma}^{(1\sim N_s)}]^T$. The diagonal entries of $\boldsymbol{S}$ are the eigenvalues of $\boldsymbol{\varsigma}^{(1\sim N_s)}[\boldsymbol{\varsigma}^{(1\sim N_s)}]^T$.

Then, based on ICA, the transformation from uncorrelated uncertainties into independent ones can be regarded as finding a transformation matrix $\boldsymbol{B}=[\boldsymbol{b}_1, \boldsymbol{b}_2, \cdots, \boldsymbol{b}_{N_c}]^T$ that can maximize the non-Gaussianity [148], which can be formulated as

$$\begin{aligned} &\max_{\boldsymbol{B}} \sum_{n=1}^{N_c} \{\mathbf{E}[G(\boldsymbol{b}_n^T \tilde{\boldsymbol{\varsigma}}^{(1\sim N_s)})] - \mathbf{E}[G(\upsilon)]\}^2 \\ &s.t.\ \mathbf{E}[(\boldsymbol{b}_{n'}^T \tilde{\boldsymbol{\varsigma}}^{(1\sim N_s)}) \circ (\boldsymbol{b}_{n''}^T \tilde{\boldsymbol{\varsigma}}^{(1\sim N_s)})] = \begin{cases} 1, n' = n'' \\ 0, n' \neq n'' \end{cases} \end{aligned} \tag{4.3}$$

where υ is an uncertainty following the standard Gaussian distribution. $G(\cdot)$ is the contrast function, which can be chosen as logcosh. $\circ$ is the Hadamard product operator.

To solve (4.3), the fixed-point algorithm [149], as presented in (4.4), is used to update $\boldsymbol{b}_n$ iteratively until it converges so that the fast ICA can be implemented.

$$\begin{cases} \boldsymbol{b}_{nv'} = \mathbf{E}[\tilde{\boldsymbol{\varsigma}}^{(1\sim N_s)} \circ \dot{G}(\boldsymbol{b}_{n(v-1)}^T \tilde{\boldsymbol{\varsigma}}^{(1\sim N_s)})] - \mathbf{E}[\ddot{G}(\boldsymbol{b}_{n(v-1)}^T \tilde{\boldsymbol{\varsigma}}^{(1\sim N_s)})]\boldsymbol{b}_{n(v-1)} \\ \boldsymbol{b}_{nv} = \boldsymbol{b}_{nv'} / \|\boldsymbol{b}_{nv'}\|_2 \end{cases} \tag{4.4}$$

where $\dot{G}(\cdot)$ and $\ddot{G}(\cdot)$ are the first and second order derivatives of $G(\cdot)$. $\boldsymbol{b}_{nv}$ and $\boldsymbol{b}_{nv'}$ are the updated $\boldsymbol{b}_n$ at v-th iteration with and without normalization, respectively. $\|\cdot\|_2$ is the ℓ_2 norm.

After $\boldsymbol{B}$ is calculated, the transformation from correlated uncertainties $\boldsymbol{\varsigma}$ to independent ones $\boldsymbol{\xi}$ can be derived as

$$\boldsymbol{\xi} = \boldsymbol{BUS}^{-1/2}\boldsymbol{U}^T\boldsymbol{\varsigma}. \tag{4.5}$$

4.2.2 Polynomial Construction for Uncertainties with Arbitrary Probability Distributions

Polynomials are formed by orthogonal bases. For the orthogonal basis $\psi^{[j_m]}(\xi_m)$ with respect to ξ_m with the order of j_m, it can be expressed as

$$\psi^{[j_m]}(\xi_m) = \sum_{n=0}^{j_m} \kappa_n \xi_m^n,\ \kappa_{j_m} = 1 \tag{4.6}$$

where κ_n is the coefficient of ξ_m^n.

To construct bases applicable to uncertainties with arbitrary probability distributions, the orthogonality is used, which is

$$\sum_{h=1}^{N_s} \psi^{[j_m]}(\xi_m^{(h)})\psi^{[j_q]}(\xi_m^{(h)})\xi_m^{(h)} / N_s = 0,\ 0 \le j_q < j_m. \tag{4.7}$$

By substituting $j_q = 0, 1, \cdots, j_m - 1$ into (4.7) in turns, $\kappa_0, \kappa_1, \cdots, \kappa_{j_m-1}$ can be derived, which can be formulated as

$$[\kappa_0, \kappa_1, \cdots, \kappa_{j_m-1}]^T = \boldsymbol{\Theta}^{-1}[\chi_1, \chi_2, \cdots, \chi_{j_m}]^T \tag{4.8}$$

where $\chi_{j_u} = \sum_{h=1}^{N_s} \xi_m^{j_u+j_m-1,(h)} / N_s, 1 \le j_u \le j_m$. $\boldsymbol{\Theta} = (\theta_{j_u j_q})_{j_m \times j_m}$.

$\theta_{j_u j_q} = -\sum_{h=1}^{N_s} \xi_m^{j_u+j_q-2,(h)} / N_s, 1 \le j_u, j_q \le j_m$.

After determining orthogonal bases according to (4.6) and (4.8), polynomials can be constructed. And to alleviate the curse of dimensionality, the hyperbolic truncation is introduced. Thus, $\varphi_j(\boldsymbol{\xi})$ can be formed as

$$\begin{gathered}\varphi_j(\boldsymbol{\xi}) = \psi^{[j_1]}(\xi_1) \circ \cdots \psi^{[j_m]}(\xi_m) \cdots \circ \psi^{[j_{N_c}]}(\xi_{N_c}) \\ \| j_m \|_{c_r} = (\sum_{m=1}^{N_c} j_m^{c_r})^{1/c_r} \le N_o\end{gathered} \tag{4.9}$$

where N_o expresses the order of GMPCE. c_r is the hyperbolic truncation coefficient.

4.2.3 Weight Coefficient Calculation

The calculation of $\boldsymbol{W}$ as a whole in (4.1) can be regarded as the multiple linear regression (MLR), where the sampling data of system response $\boldsymbol{y}^{(1\sim N_s)}$ and polynomials $\boldsymbol{\varphi}(\boldsymbol{\xi})^{(1\sim N_s)}$ have already been derived. To avoid overfitting and reduce the complexity of $\boldsymbol{W}$, the form of multi-task Elastic Net [150] is introduced in calculating $\boldsymbol{W}$, which can be formulated as the following optimization problem

$$\min_{\boldsymbol{W}} \| \boldsymbol{y}^{(1\sim N_s)} - \boldsymbol{W}\boldsymbol{\varphi}(\boldsymbol{\xi})^{(1\sim N_s)} \|_{\mathrm{F}}^2 / 2N_s + \lambda\rho \| \boldsymbol{W} \|_{21} + \lambda(1-\rho) \| \boldsymbol{W} \|_{\mathrm{F}} / 2 \tag{4.10}$$

where λ is the penalty factor of the complexity of $\boldsymbol{W}$. ρ denotes the weight coefficient of different norms. $\|\cdot\|_F$ and $\|\cdot\|_{21}$ are Frobenius norm and $\ell_1\ell_2$ norm, respectively, which are expressed as

$$\| \boldsymbol{A} \|_F = \sqrt{\sum_{k,l} a_{kl}^2}, \| \boldsymbol{A} \|_{21} = \sum_k \sqrt{\sum_l a_{kl}^2} = \sum_k \| a_{k\cdot} \|_2 \tag{4.11}$$

where a_{kl} is the entry in k-th row and l-th column of the indicated matrix $\boldsymbol{A}$.

To solve (4.10), the coordinate descent algorithm can be used. And the introduction of $\| \boldsymbol{W} \|_{\mathrm{F}}$ in (4.10) is for avoiding overfitting. The introduction of $\| \boldsymbol{W} \|_{21}$ in (4.10) is for reducing the ℓ_2 norm of $\boldsymbol{A}$ in every row, which restricts the complexity of $\boldsymbol{W}$ in every row, i.e., ensuring the sparse structure of GMPCE, thereby avoiding the curse of dimensionality.

4.2.4 Probabilistic Analysis of GMPCE Outputs

After deriving the GMPCE model in (4.1), the mean μ_i and variance σ_i^2 of $y(i\Delta t)$ can be estimated based on GMPCE as

$$\hat{\mu}_i = \sum_{h=1}^{N_p} \hat{y}(i\Delta t)^{(h)} / N_p, \hat{\sigma}_i^2 = \sum_{h=1}^{N_p} [\hat{y}(i\Delta t)^{(h)}]^2 / N_p - \hat{\mu}_i^2 \tag{4.12}$$

where N_p is the number of sampling data derived from GMPCE.

Based on KDE, the PDF $p(\cdot)$ of $y(i\Delta t)$ can be estimated as

$$\hat{p}(\hat{y}(i\Delta t)) = \sum_{h=1}^{N_K} \Phi[(\hat{y}(i\Delta t) - \hat{y}(i\Delta t)^{(h)}) / \delta_i] / (N_K \delta_i) \tag{4.13}$$

where $\Phi[\cdot]$ is the kernel function of KDE. N_K is the number of KDE sampling data derived from GMPCE. δ_i is the bandwidth of KDE with respect to $y(i\Delta t)$, which can be chosen as $1.06\hat{\sigma}_i N_K^{-0.2}$ [98].

4.3 Case Study

4.3.1 Case 1: IEEE 68-Bus Benchmark System

1) Example System

Case 1 is conducted in the IEEE 68-bus benchmark system. 3 WPGs, 3 PVs, and 3 loads with realistic uncertainties based on measurements in [151] are connected at Bus 29, 31, 41, Bus 6, 10, 36, and 27, 47, 48, respectively, as presented in Fig. 4.1. The frequency response $f(t)$ of the system with the trip of the largest infeed generator at 0.1s is analyzed, where $T_d = 10\text{s}$, $\Delta t = 0.01\text{s}$.

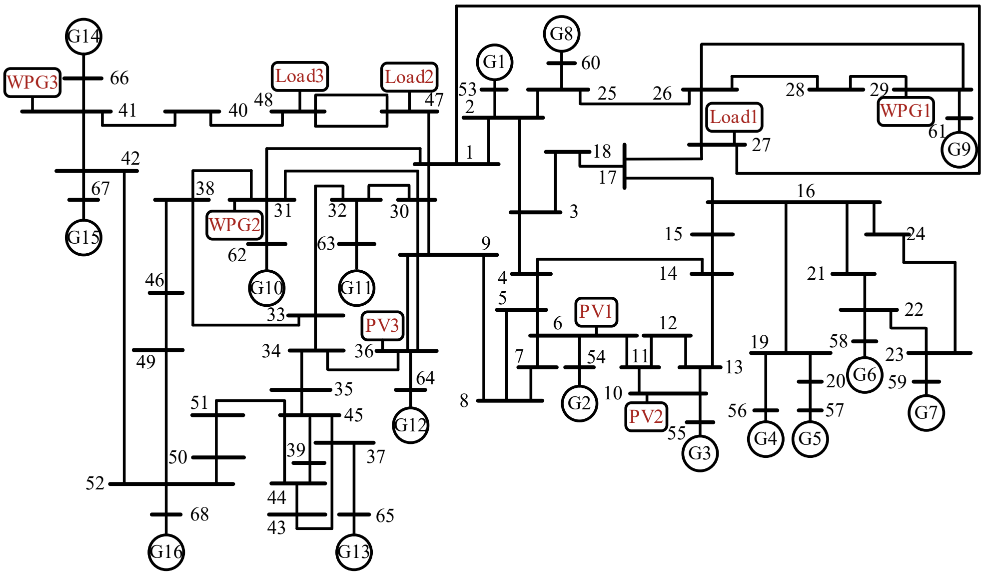

Fig. 4.1 IEEE 68-bus system with uncertainties of WPGs, PVs, and loads.

Moreover, to illustrate the probability distributions and the correlations among uncertainties, their PDFs after normalization are drawn in Fig. 4.2, and the correlation coefficients of pairwise uncertainties are listed in the upper triangular units of Table 4.1. The correlation coefficients and the independence hypothesis test results of uncertainties after conducting the proposed uncertainty transformation are listed in the lower triangular units of Table 4.1 to show the performance of the uncertainty transformation. In Table 4.1, “0/Y” denotes that the correlation coefficient is 0, and the independence hypothesis is accepted at a 5% level of significance.

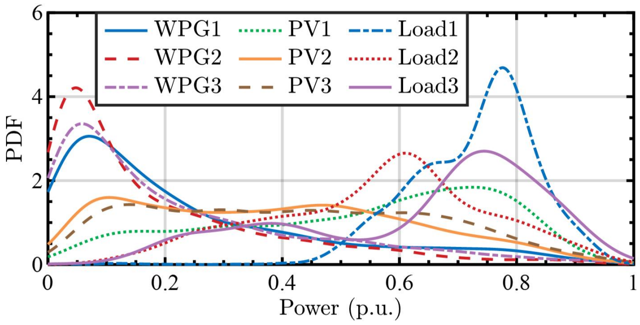

Fig. 4.2 PDFs of uncertainties.

Table 4.1 Correlations and independence among uncertainties before and after transformation

	U1	U2	U3	U4	U5	U6	U7	U8	U9
U1	-	0.01	0.02	-0.24	-0.08	-0.06	0.04	0.16	0.08
U2	0/Y	-	0.54	-0.03	-0.22	-0.25	0.08	0.17	0.09
U3	0/Y	0/Y	-	0.01	-0.30	-0.29	0.15	0.07	0.12
U4	0/Y	0/Y	0/Y	-	0.40	0.41	-0.07	-0.33	-0.14
U5	0/Y	0/Y	0/Y	0/Y	-	0.89	-0.09	-0.47	-0.23
U6	0/Y	0/Y	0/Y	0/Y	0/Y	-	-0.10	-0.48	-0.23
U7	0/Y	0/Y	0/Y	0/Y	0/Y	0/Y	-	0.53	0.82
U8	0/Y	0/Y	0/Y	0/Y	0/Y	0/Y	0/Y	-	0.81
U9	0/Y	0/Y	0/Y	0/Y	0/Y	0/Y	0/Y	0/Y	-

From Fig. 4.2, the PDFs of realistic uncertainties are complicated, especially PV3 and Load 3, the shapes of which are quite different from the standard PDFs. And in Table 4.1, the correlation coefficients between different pairwise uncertainties are various. By comparison, after uncertainty transformation, all correlation coefficients among uncertainties are close to 0, and all independence hypothesis tests are passed. The results demonstrate the effectiveness of the proposed uncertainty transformation in transforming the correlated uncertainty into independent ones.

2) Validation of Generic Multi-Output Polynomial Chaos Expansion for Probabilistic Frequency Stability Analysis Aiming at Frequency Response Trajectories

The results of 5000 MCSs are regarded as the baselines. The performance of the proposed GMPCE in efficiency and accuracy is compared with those of SPCE and LRA [100] with the setting as: $N_s = 200$, $N_o = 4$, $\lambda = 1/(2N_s)$, $\rho = 0.5$. The selection of λ and ρ is to equally consider the sparsity and generalization. And SPCE is chosen as the comparison method since the conventional PCE is infeasible with the above setting due to the curse of dimensionality.

Firstly, the efficiency of different methods is compared, as illustrated in Table 4.2. From Table 4.2, since SPCE, LRA, and GMPCE only require 200 simulations, whereas MCS requires 5000 simulations, the simulation time needed for SPCE, LRA, and GMPCE is significantly shorter than that needed for MCS. Moreover, the efficiency of GMPCE is greatly superior to that of SPCE and LRA. The method execution time of GMPCE is more than 40 times shorter than that of SPCE and LRA. The reason is that SPCE and LRA models only have one output. To analyze $f(t)$ at each time point, $N_y = T_d / \Delta t = 1000$ models are required to be constructed separately. By comparison, GMPCE has multiple outputs, and the number of the constructed GMPCE model is only one, indicating the time-saving merit.

Table 4.2 Efficiency comparison of different methods in Case 1

Method	Simulation time (s)	Method execution time (s)	Total time (s)
MCS	9852.744	-	9852.744
SPCE	391.659	110.944	502.603
LRA		101.016	492.675
GMPCE		2.320	393.979

Moreover, the accuracy of methods in estimating the moments, i.e., mean and standard deviation (Std.), of $f(t)$ is compared, as shown in Fig. 4.3. According to Fig. 4.3(a) and Fig. 4.3(b), the overlapping degree between the moment curves derived from MCS and those from GMCPE are higher than those from SPCE and LRA. Moreover, from Fig. 4.3(b), the Std. curve from GMCPE is smoother since each time point corresponds to one SPCE or LRA model, $\boldsymbol{\omega}_i$ of which are calculated separately. By comparison, $\boldsymbol{W}$ of GMPCE is calculated as a whole.

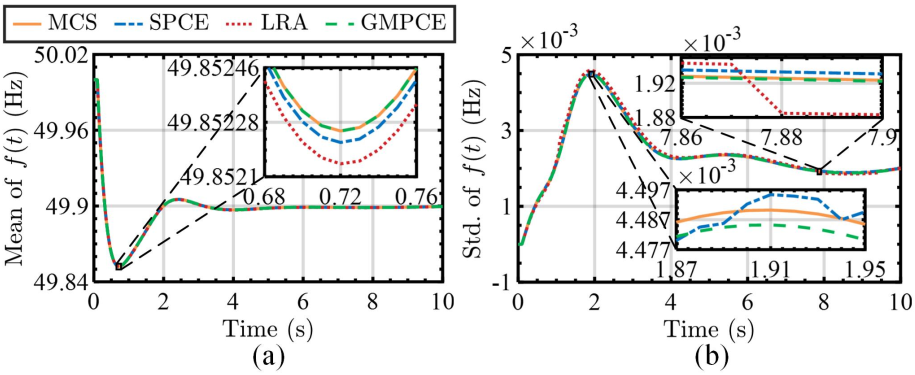

Fig. 4.3 Accuracy comparison of $f(t)$ moment estimation: (a) Mean; (b) Std..

To quantify and compare the overall accuracy of different methods, PDFs of AEs of moments are introduced and presented in Fig. 4.4. As seen in Fig. 4.4(a) and Fig. 4.4(b), the AE PDFs from GMCPE have higher peaks and thinner tails, the peaks of which are closer to 0. The results indicate that GMCPE has higher accuracy in estimating moments of system responses. And the reason is that the complicated correlations among realistic uncertainties cannot be transformed accurately in SPCE and LRA, which decreases their estimation accuracy.

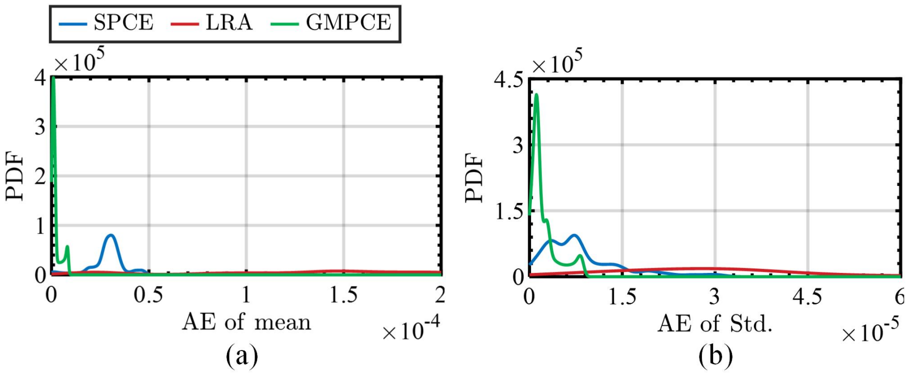

Fig. 4.4 PDF comparison of moment AEs in Case 1: (a) Mean; (b) Std..

Also, to assess the accuracy of methods in estimating $f(t)$ PDFs at each time point, AEs of PDFs are presented in Fig. 4.5.

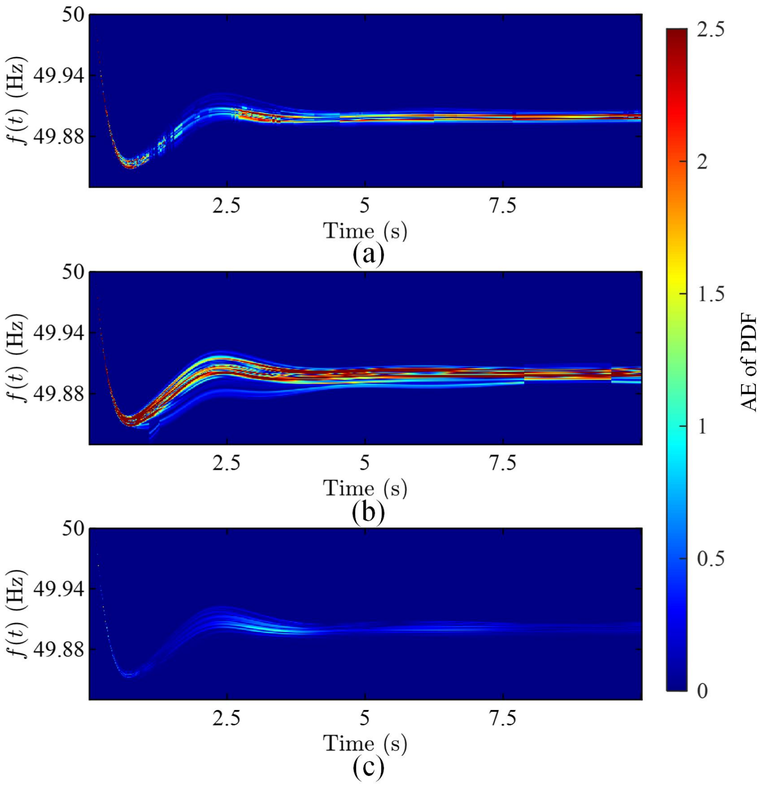

Fig. 4.5 AE of PDF of $f(t)$ from (a) SPCE; (b) LRA; (c) GMPCE.

From Fig. 4.5, the PDF AE of $f(t)$ from GMPCE is much smaller than those from SPCE and LRA, indicating its higher accuracy at different time points, which can be observed more clearly when the results at only one time point are shown, as drawn in Fig. 4.6. It can be seen in Fig. 4.6 that the overlapping degree between the PDF from MCS and the PDF from GMPCE is higher than those from SPCE and LRA.

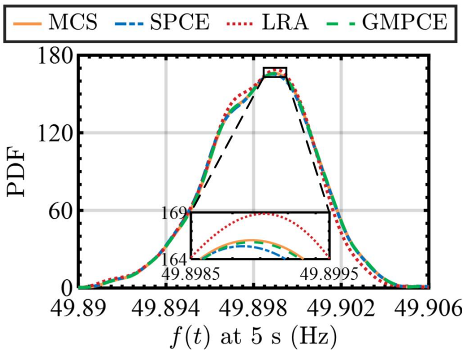

Fig. 4.6 PDFs of $f(t)$ at $t = 5\text{s}$.

Furthermore, to quantify and compare the overall accuracy of methods in calculating the PDFs of $f(t)$, the shape difference of PDFs ε, i.e., $\varepsilon = \| p(f(t)) - \hat{p}(\hat{f}(t)) \|_2$, is introduced, the PDFs of which are drawn in Fig. 4.7. From Fig. 4.7, the PDF of ε from GMCPE is with higher peaks closer to 0 and thinner tails, showing higher overall accuracy of GMPCE in calculating the PDFs of $f(t)$.

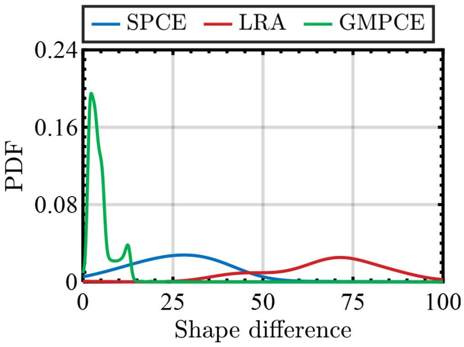

Fig. 4.7 PDF of the shape difference of PDFs in Case 1.

4.3.2 Case 2: 240-Bus WECC System

To verify the scalability and applicability of GMPCE in the larger power system with numerous uncertainties, case studies implemented in the 240-bus WECC system are conducted, where 37 RPGs are integrated [152]. Also, the top 13 loads with the highest active power are selected as uncertainties as examples. Thus, the total uncertainty quantity of RPGs and loads in the system is 50. These uncertainties are based on the measurements in [153]. PFSA is conducted by using GMPCE to analyze the system frequency response $f_{Wsys}(t)$ and area-level frequency response in Area 1 $f_{Wa1}(t)$ of the system with the trip of the largest infeed generator at 0.1s. Firstly, the efficiency comparison among different methods is presented in Table 4.3. Compared with the time cost shown in Table 4.2, the simulation time rises around 4.5 times with the increase of the analyzed system scale. And since GMPCE, as a nonintrusive method, only needs the data of uncertainties and data of system dynamic responses as inputs and outputs to determine its structure and calculate the coefficients, the method execution time of GMPCE rises around 3.5 times with the increase of uncertainty quantity rather than that of analyzed system scale. Moreover, similar time cost increases can be found in other methods, and the increase of method execution time of GMPCE is limited compared with other methods. Thus, these results demonstrate that GMPCE possesses the time-saving merit in UPA of the large-scale power system with numerous uncertainties.

Table 4.3 Efficiency comparison of different methods in Case 2

Method	Simulation time (s)	Method execution time (s)	Total time (s)
MCS	43932.563	-	43932.563
SPCE	1750.381	308.453	2058.834
LRA		236.691	1987.072
GMPCE		8.179	1758.560

Then, the accuracy of methods in estimating the moments and PDFs of frequency responses are compared and drawn in Fig. 4.8, Fig. 4.9 and Fig. 4.10, Fig. 4.11, respectively. From Fig. 4.8(a), Fig. 4.8(c), for mean of frequency responses, all mean curves derived from different methods are very close to the curves from MCS, which illustrates their high accuracy in estimating the mean of frequency responses. Moreover, from Fig. 4.9(a) and Fig. 4.9(c), though the peaks of AE PDFs from LRA are closer to 0 than those from GMPCE, the values of their peaks are lower than those from GMPCE, and the tails of AE PDFs from LRA are fatter. This means that the errors of LRA in estimating the mean of frequency responses will fluctuate in a relatively large range compared with GMPCE. And for Std. of frequency responses presented in Fig. 4.9(b) and Fig. 4.9(d), the peaks of AE PDFs from GMPCE are much higher and closer to 0 compared with those from SPCE and LRA, which means that the Std. curves from GMPCE are closer to those from MCS, as drawn in Fig. 4.8(b) and Fig. 4.8(d). Moreover, for PDFs of frequency responses, it can be clearly observed that AEs of frequency response PDFs from GMPCE are much smaller than those from SPCE and LRA, as presented in Fig. 4.10, and the shape differences of frequency response PDFs from GMPCE are also smaller, as illustrated in Fig. 4.11(b) and Fig. 4.11(d). These results indicate the high accuracy of GMPCE in estimating the moments and PDFs of frequency responses of the large-scale power system with numerous uncertainties.

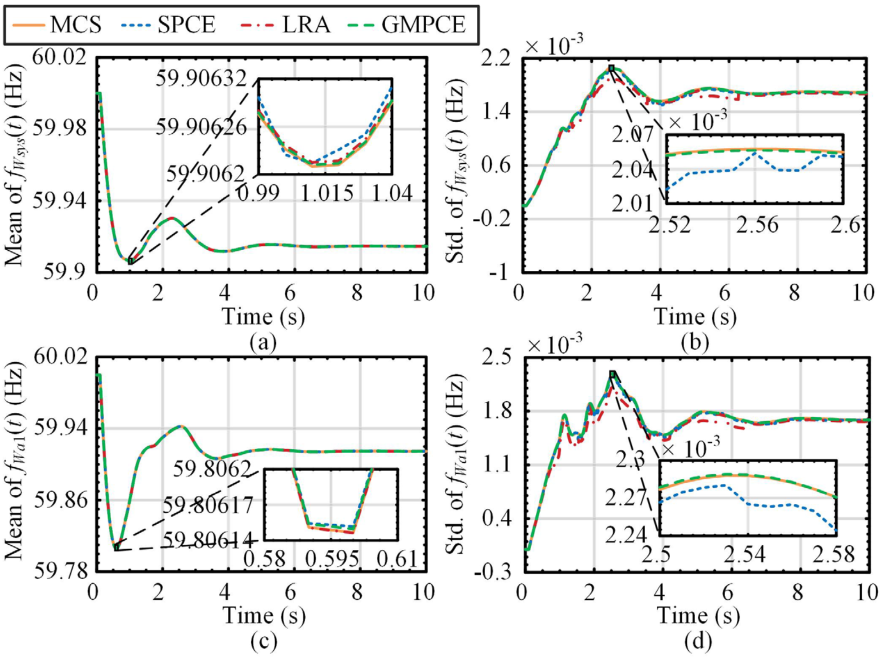

Fig. 4.8 (a) Mean of $f_{Wsys}(t)$; (b) Std. of $f_{Wsys}(t)$; (c) Mean of $f_{Wa1}(t)$; (d) Std. of $f_{Wa1}(t)$.

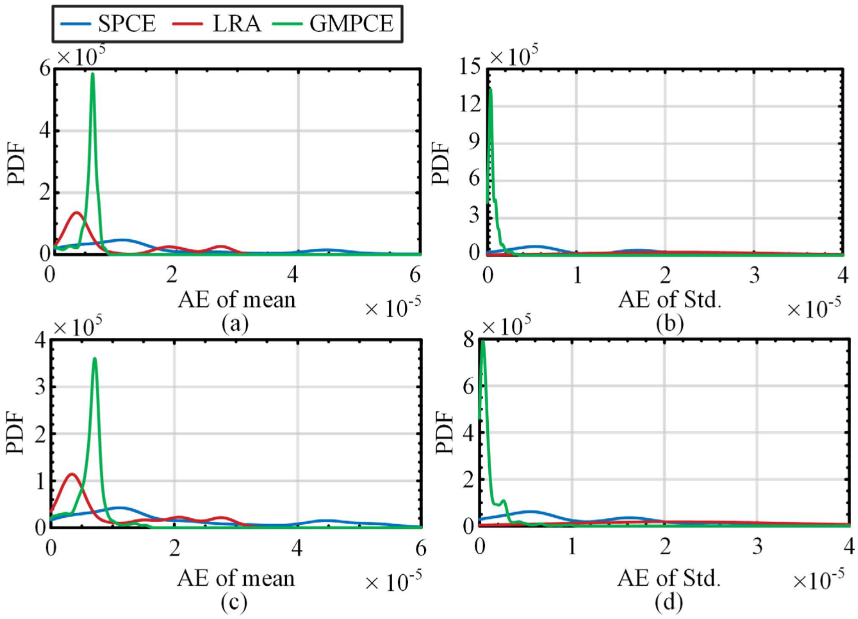

Fig. 4.9 (a) AE PDF of $f_{Wsys}(t)$ mean; (b) AE PDF of $f_{Wsys}(t)$ Std.; (c) AE PDF of $f_{Wa1}(t)$ mean; (d) AE PDF of $f_{Wa1}(t)$ Std..

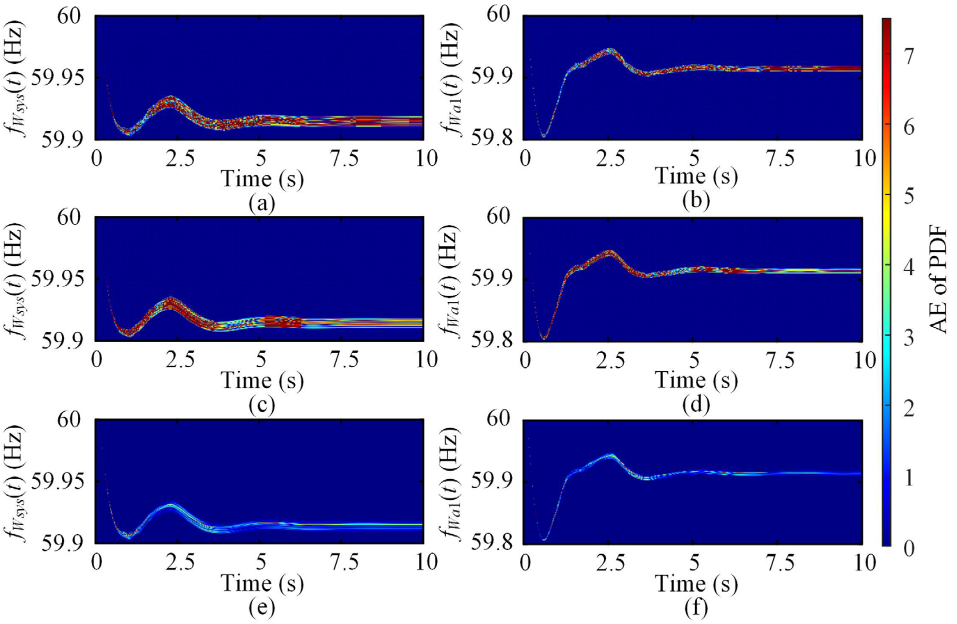

Fig. 4.10 AE of $f_{Wsys}(t)$ PDF from (a) SPCE; (c) LRA; (e) GMPCE; AE of $f_{Wa1}(t)$ PDF from (b) SPCE; (d) LRA; (f) GMPCE.

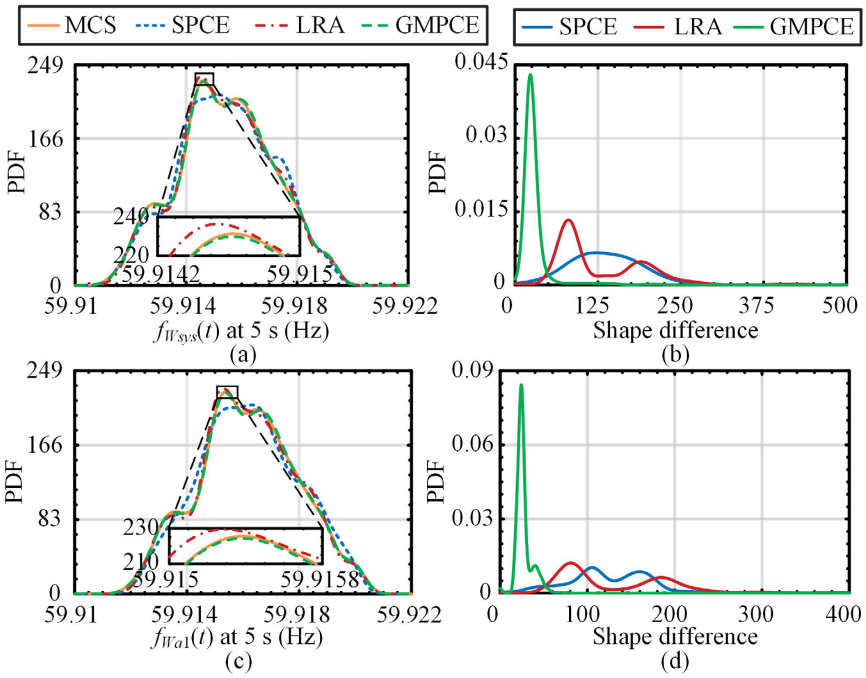

Fig. 4.11 (a) PDF of $f_{Wsys}(t)$ at $t = 5\text{s}$; (b) PDF of ε of $f_{Wsys}(t)$; (c) PDF of $f_{Wa1}(t)$ at $t = 5\text{s}$; (d) PDF of ε of $f_{Wa1}(t)$.

4.4 Summary

In this chapter, firstly, a generic transformation based on ICA is proposed to transform uncertainties with complicated correlations into independent ones. Secondly, GMPCE is proposed to quantify the system frequency response in an efficient manner, the polynomial construction of which is suitable for uncertainties with arbitrary probability distributions. And GMPCE has the sparse structure and thus avoids the curse of dimensionality, thereby being capable of tackling large-scale uncertainties. The results of case studies demonstrated the superiority of the proposed method in accuracy and efficiency.

Chapter 5 Comprehensive Uncertainty Quantification for Frequency Stability Considering Different Timescale Characterizations of Uncertainties

5.1 Introduction

Chapter 2-Chapter 4 focus on PFSA, i.e., the impact of STCUs on power system frequency stability, which is also the concerned issue in most existing studies on UQ for frequency stability of power systems. However, the specific choice of the timescale characterization of uncertainties is based on focused tasks and nature of uncertainty sources. FTCUs may be used in UQ of power system stability, which need to be considered together with STCUs simultaneously to ensure accurate UQ results. And there is a lack of an effective method capable of addressing STCUs and FTCUs, which is in a pressing need. To fill the research gap, this chapter proposes a comprehensive UQ method for frequency stability considering STCUs and FTCUs.

5.2 Different Timescale Characterizations of Uncertainties and Their Transformations

5.2.1 Slow Timescale Characterizations of Uncertainties

STCUs refer to the randomness of steady-state operating points of uncertain sources varying with time slowly and infrequently, the values of which are considered to be constant in the dynamic response during a short time generally. Thus, STCUs can also be regarded as the randomness of initial values. Normally, STCUs can be treated as random variables. For the independent random variable ξ_{vg}, PDF $p_{\xi_{vg}}(\xi_{vg})$ can be adopted to characterize the probability of them. Also, some STCUs may be correlated, for example, wind speeds of wind power generations with close spatial distance [27]. The PDF $p_{Cop\xi_{c1-G}}(\xi_{c1}, \xi_{c2}, \cdots, \xi_{cG})$ of correlated random variables $\xi_{c1}, \xi_{c2}, \cdots, \xi_{cG}$ with correlation matrix $\boldsymbol{\rho}_{\xi_{c1-G}}$ can be modeled by the Copula function as [109]

$$\begin{aligned} & p_{Cop\xi_{c1-G}}(\xi_{c1}, \xi_{c2}, \cdots, \xi_{cG}) \\ & = \frac{\partial^G \varphi_{\rho_{\xi_{c1-G}}}(\varphi^{-1}(\xi_{c1}), \varphi^{-1}(\xi_{c2}), \cdots, \varphi^{-1}(\xi_{cG}))}{\partial P_{\xi_{c1}}(\xi_{c1}) \partial P_{\xi_{c2}}(\xi_{c2}) \cdots \partial P_{\xi_{cG}}(\xi_{cG})} \prod_{g=1}^{G} p_{\xi_{cg}}(\xi_{cg}) \end{aligned} \tag{5.1}$$

where $p.(\cdot)$ is the marginal PDF. $P.(\cdot)$ denotes the integral of $p.(\cdot)$. φ represents the Gaussian generator function of Copula. G is the number of correlated random variables.

Since only the independent random variables are acceptable for the PCE-based UPA method, the correlated random variables $\boldsymbol{\xi}_c$ should be transformed into the independent ones $\boldsymbol{\xi}_v$, where Cholesky decomposition is applied [109] to obtain the transformation matrix $\boldsymbol{C}_{\xi_c}$ as

$$\boldsymbol{\rho}_{\xi_c} = \boldsymbol{C}_{\xi_c} \boldsymbol{C}_{\xi_c}^T \tag{5.2}$$

where $\boldsymbol{\rho}_{\xi_c}$ is the correlation matrix of $\boldsymbol{\xi}_c$.

$\boldsymbol{\xi}_v$ can be derived as

$$\boldsymbol{\xi}_v = \boldsymbol{C}_{\xi_c}^{-1} \boldsymbol{\xi}_c. \tag{5.3}$$

5.2.2 Fast Timescale Characterizations of Uncertainties

FTCUs focus on the time-varying characteristics of uncertain sources varying rapidly and frequently during a short time. In power systems, it is usually modeled as the SDE with standard stochastic processes [125].

$$dS_s = \mu_{S_s}(S_s)dt + \sigma_{S_s}(S_s)dS_t \tag{5.4}$$

where S_s is the dynamic stochastic process. $\mu.(\cdot)$ and $\sigma.(\cdot)$ are drift and diffusion terms, separately. S_t is the typical stochastic process. When S_s is a continuous FTCU, S_t is often selected as the Winner process W_t, which can be used to model the fluctuation of RPG [112], error in measurement, and noise in communication [127]. When S_s is a discrete jump FTCU, S_t can be described by the compound Poisson process C_t [114]

$$C_t = \sum_{k=1}^{N_t} \varsigma_k \tag{5.5}$$

where N_t is the Poisson process, ς_k denotes the independent identically distributed random variable.

5.2.3 Transformation of Fast Timescale Characterizations of Uncertainties to Slow Timescale Characterizations of Uncertainties

The modeling form in (5.4) cannot directly match the PCE-based UPA method. Taking uncertainty modeled by the Winner process as an example, W_t has the characteristic that the values in the current time and those in the historical time follow a Gaussian probability distribution. In every time step, a new random variable will be introduced. If PCE-based methods are directly adopted to approximate the system response, the number of random variables to be considered equals the concerned system response duration divided by the step length. This will result in the curse of dimensionality, leading to the failure to obtain the expected results in a limited time. Thus, if we want to retain the time-saving advantage of the PCE-based UPA method, S_t should be transformed into the form expressed by the limited number of independent random variables.

It has been proved that the continuous Winner process W_t, can be transformed as (5.6) [99, 154]. And the approximation of W_t can be derived by taking the first I_W terms of (5.6).

$$W_t = \sum_{n=1}^{\infty} \xi_{Wn} \frac{\sqrt{2T}}{(n-1/2)\pi} \sin[\frac{(n-1/2)\pi t}{T}] \tag{5.6}$$

where $t \in [0, T]$. T is the concerned period of system dynamics. ξ_{Wn} is the independent identically distributed random variable.

Thus, the main work in the following is to transform the compound Poisson process C_t into the superposition of random variables.

According to Karhunen-Loève expansion (KLE) and Mercer's Theorem [155], if a stochastic process $r(t)$ on the interval $t \in (0, T)$ with a mean $\mu_r(t)$, a bounded variance $\sigma_r(t)$, and a bounded, symmetric, and positive definite covariance function $K_r(s, t)$, $r(t)$ can be obtained as

$$r(t) = \mu_r(t) + \sum_{n=1}^{\infty} \xi_{vn} \sqrt{\lambda_n} e_n(t) \tag{5.7}$$

where $\lambda_{\cdot}$ is the nonnegative eigenvalue of eigenfunction $e_{\cdot}(t)$, and items are arranged in descending order according to the value of $\lambda_{\cdot}$. ξ_{vn} is the independent random variable.

Additionally, the variables and functions in (5.7) satisfy the following relationship.

$$\begin{cases} \int_0^T K_r(s,t)e_n(s)ds = \lambda_n e_n(t) \\ \int_0^T e_n^2(s)ds = 1 \\ \xi_{vn} = \dfrac{1}{\sqrt{\lambda_n}}\int_0^T [r(t)-\mu_r(t)]e_n(t)dt \end{cases}. \tag{5.8}$$

Assume that the mean and the variance of ς_k are μ_ς and σ_ς, and the parameter of Poisson process N_t is σ_N. For the compound Poisson process C_t, the mean $\mu_C(t)$ and variance $\sigma_C(t)$ can be derived according to the double expectation theorem:

$$\mu_C(t) = \mu_\varsigma \sigma_N t, \sigma_C(t) = (\mu_\varsigma^2 + \sigma_\varsigma^2)\sigma_N t. \tag{5.9}$$

Equation (5.9) indicates the existence of $\mu_C(t)$ and $\sigma_C(t)$. Also, due to $t \in (0,T)$, $\sigma_C(t)$ is bounded. Moreover, according to (5.9), the covariance function $K_C(s,t)$ can be derived as

$$K_C(s,t) = (\mu_\varsigma^2 + \sigma_\varsigma^2)\sigma_N \min\{s,t\} + \mu_\varsigma^2 \sigma_N^2 st. \tag{5.10}$$

Due to $s,t \in (0,T)$ and $\sigma_N > 0$, $K_C(s,t)$ is bounded, symmetric, and positive definite. Thus, (5.9) and (5.10) indicate that compound Poisson process C_t can be expanded as the form of (5.7).

Substituting (5.10) into the first equation of (5.8), it can be transformed as

$$\begin{aligned} &(\mu_\varsigma^2 + \sigma_\varsigma^2)\sigma_N \int_0^t s e_n(s)ds \\ &+(\mu_\varsigma^2 + \sigma_\varsigma^2)\sigma_N t\int_t^T e_n(s)ds + \mu_\varsigma^2\sigma_N^2 t\int_0^T s e_n(s)ds = \lambda_n e_n(t). \end{aligned} \tag{5.11}$$

The derivation of (5.11) with respect to t can be obtained by

$$(\mu_\varsigma^2 + \sigma_\varsigma^2)\sigma_N \int_t^T e_n(s)ds + \mu_\varsigma^2\sigma_N^2 \int_0^T s e_n(s)ds = \lambda_n de_n(t)/dt. \tag{5.12}$$

The derivation of (5.12) with respect to t can be computed as

$$\lambda_n d^2 e_n(t)/dt + (\mu_\varsigma^2 + \sigma_\varsigma^2)\sigma_N e_n(t) = 0. \tag{5.13}$$

The general solution of (5.13) can be derived as

$$e_n(t) = c_{1n} \sin[\sqrt{\frac{(\mu_\varsigma^2 + \sigma_\varsigma^2)\sigma_N}{\lambda_n}} t] + c_{2n} \cos[\sqrt{\frac{(\mu_\varsigma^2 + \sigma_\varsigma^2)\sigma_N}{\lambda_n}} t]. \tag{5.14}$$

where c_{1n} and c_{2n} are undetermined coefficients.

According to (5.11) and (5.12), the boundary conditions can be calculated as

$$\begin{cases} e_n(0) = 0 \\ de_n(T)/dt = \mu_\varsigma^2 \sigma_N^2 \int_0^T s e_n(s) ds / \lambda_n \end{cases}. \tag{5.15}$$

Substituting (5.15) into (5.14), c_{2n} and λ_n are derived as

$$\begin{cases} c_{2n} = 0 \\ \begin{cases} \tan[\sqrt{\frac{(\mu_\varsigma^2 + \sigma_\varsigma^2)\sigma_N}{\lambda_n}} T] \\ -\sqrt{\frac{(\mu_\varsigma^2 + \sigma_\varsigma^2)\sigma_N}{\lambda_n}} (T + \frac{\mu_\varsigma^2 + \sigma_\varsigma^2}{\mu_\varsigma^2 \sigma_N}) = 0,\ \mu_\varsigma \neq 0 \\ \lambda_n = \sigma_N \left[\frac{\sigma_\varsigma T}{(n-1/2)\pi} \right]^2,\ \mu_\varsigma = 0 \end{cases} \end{cases}. \tag{5.16}$$

Substituting (5.14) and (5.16) into the second equation of (5.8), c_{1n} is computed as

$$c_{1n} = \begin{cases} \frac{2}{\sqrt{2T - \sqrt{\frac{\lambda_n}{(\mu_\varsigma^2 + \sigma_\varsigma^2)\sigma_N}} \sin(2\sqrt{\frac{(\mu_\varsigma^2 + \sigma_\varsigma^2)\sigma_N}{\lambda_n}} T)}},\ \mu_\varsigma \neq 0 \\ \sqrt{\frac{2}{T}},\ \mu_\varsigma = 0 \end{cases}. \tag{5.17}$$

Thus, C_t has the following transformation form as

$$C_t = \begin{cases} \mu_\varsigma \sigma_N t + \sum_{n=1}^{\infty} \xi_{Cn} \sqrt{\lambda_n} c_{1n} \sin[\sqrt{\frac{(\mu_\varsigma^2 + \sigma_\varsigma^2)\sigma_N}{\lambda_n}} t],\ \mu_\varsigma \neq 0 \\ \sum_{n=1}^{\infty} \xi_{Cn} \frac{\sigma_\varsigma \sqrt{2\sigma_N T}}{(n-1/2)\pi} \sin[\frac{(n-1/2)\pi t}{T}],\ \mu_\varsigma = 0 \end{cases} \tag{5.18}$$

where the distribution of independent random variable ξ_{Cn} can be derived according to the third equation of (5.8).

The approximation of C_t can be derived by taking the first I_C terms of (5.18). After substituting the truncated (5.6) and (5.18) into (5.4), the number of the introduced random variables will not increase with the number of simulation steps, which can alleviate the curse of dimensionality when applying the PCE-based UPA method.

5.3 Uncertainty Propagation Analysis with Different Timescale Characterizations Based on Scalable Polynomial Chaos Expansion

Due to the time-saving advantage of the PCE, the UPA in this chapter is based on the PCE. PCE-based UPA adopts a truncated series of orthogonal polynomials associated with the probability distribution of $\boldsymbol{\xi}$ to approximate the relationship $q(\cdot)$ between the independent random variables $\boldsymbol{\xi} = [\xi_1, \xi_2, \cdots, \xi_{N_\xi}]$ (short for $\boldsymbol{\xi_v} = [\xi_{v1}, \xi_{v2}, \cdots, \xi_{vN_{\xi_v}}]$), where N_ξ is the number of independent random variables, and the concerned system outputs z. z can be chosen as the system responses or the stability indices. The PCE model can be derived as

$$z = q(\boldsymbol{\xi}) = \sum_{i=0}^{\infty} a_i \psi_i(\boldsymbol{\xi}) \approx \hat{z} = \hat{q}(\boldsymbol{\xi}) = \sum_{i=0}^{N_p - 1} a_i \psi_i(\boldsymbol{\xi}) \tag{5.19}$$

where N_p is the truncated number. a_i denotes the undetermined coefficient. Polynomial $\psi_i(\boldsymbol{\xi})$ is the tensor product $\otimes$ of polynomial chaos basis $\phi_i(\xi_\cdot)$

$$\psi_i(\boldsymbol{\xi}) = \phi_i(\xi_1) \otimes \phi_i(\xi_2) \otimes \cdots \otimes \phi_i(\xi_{N_\xi}). \tag{5.20}$$

Thus, the design of the PCE-based uncertainty propagation analysis method is to determine polynomial chaos basis $\phi_i(\xi)$ and coefficient a_i.

5.3.1 Construction of Polynomial Chaos Bases for Arbitrary Distributions

The forms of polynomial chaos bases are determined by the probability distributions of random variables. The conventional construction of polynomial chaos bases is only suitable for some typical probability distributions listed in the Askey scheme [156]. However, there are still some typical probability distributions not included in the Askey scheme, for example, the Weibull distribution. Moreover, after KLE or the transformation of correlated random variables into independent ones, random variables may not follow any typical probability distributions. And the actual data of random variables can be complicated and cannot be characterized by existing probability distributions accurately. Thus, the Askey scheme is not applicable to these random variables. To tackle the above situation, a generic construction principle of polynomial chaos basis associated with the independent random variable ξ, PDF of which is $p_\xi(\xi)$, is given as follows.

The *j*-th order orthogonal polynomial $\phi_{i,j}(\xi)$ can be expressed as

$$\phi_{i,j}(\xi) = \alpha_0 + \alpha_1\xi + \alpha_2\xi^2 + \cdots + \alpha_{j-1}\xi^{j-1} + \xi^j. \tag{5.21}$$

According to orthogonality, there is

$$\int \phi_{i,j}(\xi)\phi_{i,l}(\xi)p_\xi(\xi)d\xi = 0,\ 0 \le l < j. \tag{5.22}$$

Substituting $l = 0, 1, 2, \cdots, j-1$ in turns into (5.22), $\alpha_0, \alpha_1, \cdots, \alpha_{j-1}$ can be derived sequentially.

The above computation procedure can be summarized as

$$[\alpha_0, \alpha_1, \cdots, \alpha_{j-1}]^T = \boldsymbol{B}^{-1}[\gamma_1, \gamma_2, \cdots, \gamma_j]^T \tag{5.23}$$

where $\boldsymbol{B} = (\beta_{kl})_{j \times j}$. $\beta_{kl} = \int p_\xi(\xi)\xi^{k+l-2}d\xi, 1 \le k, l \le j$. $\gamma_k = -\int p_\xi(\xi)\xi^{k+j-1}d\xi, 1 \le k \le j$.

In the actual conditions, the sampled historical data of ξ may be available, not PDF $p_\xi(\xi)$. Then, the expression of β_{kl} and γ_k will be the summation form of sampled data.

5.3.2 Scale Reduction of Polynomial Chaos Expansion and Computation of Coefficients of Polynomial Chaos

According to (5.19) and (5.20), the number of undetermined coefficients of the full-order PCE is

$$N_p = (N_\xi + N_o)!/(N_\xi!N_o!) \tag{5.24}$$

where N_o denotes the order number of expansion.

According to (5.24) and [97], if the normal method for calculating coefficients is applied, N_p samples are required at least to obtain a PCE model with acceptable accuracy. However, N_p will increase rapidly with the rise of N_ξ. Moreover, when FTCUs are considered, multiple random variables will be introduced based on KLE. Thus, the number of undetermined coefficients is required to reduce to avoid the curse of dimensionality under the premise of ensuring the accuracy of the UQ method.

Since the low-order interactions of inputs usually lead to the main effects compared with the high-order interactions [157], hyperbolic truncation is applied to remove the items of high-order interactions.

$$\| v_{i,l} \|_{c_h} = \left(\sum_{l=1}^{N_\xi} v_{i,l}^{c_h}\right)^{\frac{1}{c_h}} \le N_o \tag{5.25}$$

where $v_{i,l}$ is the order of random variable ξ_l in $\phi_i(\xi_l)$. c_h denotes the truncation coefficient. When $c_h = 1$, (5.25) has the same expression of the full-order PCE.

After the preliminary truncation, the orthogonal polynomials $\psi_i(\boldsymbol{\xi})$ with the relatively main effect on the output are selected. To further reduce the number of undetermined coefficients, least angle regression (LAR) [158] is applied. Before the selection of $\psi_i(\boldsymbol{\xi})$, random variables are sampled based on LHS [103] to improve the sampling efficiency, forming the sampled dataset $\boldsymbol{\xi}_{(N_s)}$, where N_s is the number of sampled data. The procedure of selecting $\psi_i(\boldsymbol{\xi})$ based on LAR can be summarized as follows.

1) Initialize $a_0, a_1, \cdots, a_{N_p-1} = 0$, and define the initial candidate set Γ_c as $\{\psi_0(\boldsymbol{\xi}), \psi_1(\boldsymbol{\xi}), \cdots, \psi_{N_p-1}(\boldsymbol{\xi})\}$ and the initial selected set Γ_s as $\varnothing$.

2) Calculate the correlation function $C_f(\boldsymbol{\psi}(\boldsymbol{\xi})) = \boldsymbol{\psi}^T(z - \hat{z})$ and move $\psi_i(\boldsymbol{\xi})$ with largest C_f from Γ_c to Γ_s.

3) Diagonally move coefficients of orthogonal polynomials in Γ_s until there is an orthogonal polynomial $\psi_i(\boldsymbol{\xi})$ in Γ_c, the correlation function of which equals to the sum of the correlation function in Γ_s. And move $\psi_i(\boldsymbol{\xi})$ from Γ_c to Γ_s.

4) Compute the LOO error ε_{LOO} of $\hat{z}$. The LOO error can be obtained as [141]

$$\varepsilon_{LOO} = \sum_{m=1}^{N_s} \left(\frac{z_{(m)} - \hat{z}_{(m)}}{1 - d_m}\right)^2 / \sum_{m=1}^{N_s} \left(z_{(m)} - \frac{1}{N_s}\sum_{k=1}^{N_s} z_{(k)}\right)^2 \tag{5.26}$$

where d_m is the m-th element in $\boldsymbol{d} = diag(\boldsymbol{\psi}(\boldsymbol{\psi}^T\boldsymbol{\psi})^{-1}\boldsymbol{\psi}^T)$.

5) Repeat Step 3)-Step 4) until the number of orthogonal polynomials in Γ_s equals to $\min\{N_p, N_s - 1\}$. Then, select Γ_s with the lowest ε_{LOO} as the selected

orthogonal polynomials.

After conducting the $\psi_i(\xi)$ selection procedure, the number of undetermined coefficients has been reduced, which will not continuously increase with the number of STCUs and FTCUs. Thus, the curse of dimensionality is avoided, thereby indicating that the proposed method can be feasible when the number of STCUs and FTCUs is large. And the undetermined coefficients can be calculated by minimizing the estimation error of the PCE $\sum_{m=1}^{N_s}(z_{(m)}-\hat{z}_{(m)})^2$.

After calculating coefficients, the mean $\mu_{\hat{z}}$ and the variance $\sigma_{\hat{z}}^2$ of $\hat{z}$ can be determined as follows:

$$\mu_{\hat{z}} = a_0, \sigma_{\hat{z}}^2 = \sum_{i=1}^{N_p-1} a_i^2 \mathbf{E}[\psi_i^2(\xi)]. \tag{5.27}$$

Moreover, the estimated PDF $\hat{p}_{\hat{z}}(\hat{z})$ of $\hat{z}$ can be derived based on KDE as

$$\hat{p}_{\hat{z}}(\hat{z}) = \sum_{m=1}^{N_K} p_K[(\hat{z}-\hat{z}_{(m)})/b_K]/(N_K b_K) \tag{5.28}$$

where N_K is the sample number of KDE. p_K denotes the kernel function, which is selected as the Gaussian kernel. b_K represents the bandwidth, which can be determined via $1.06\sigma_{\hat{z}}N_K^{-0.2}$ [98].

5.4 Uncertainty Sensitivity Analysis with Different Timescale Characterizations Based on Analysis of Variance

Sensitivity analysis of power system dynamics under STCUs and FTCUs aims to quantify the impact of uncertainties on system stability indices and identify the critical uncertainties. In this thesis, frequency stability is considered as an example, where FN and RoCoF are selected as the frequency stability indices, but the proposed method is not limited to the frequency stability issues.

ANOVA is applied to conduct sensitivity analysis. For random variables $\boldsymbol{\xi} = [\xi_l, \boldsymbol{\xi}_{\bar{l}}]$, where $\boldsymbol{\xi}_{\bar{l}}$ are the rest of the random variables of $\boldsymbol{\xi}$ apart from ξ_l. The total variance $\mathbf{D}_z(z)$ of z can be derived as [159]

$$\mathbf{D}_z(z) = \mathbf{D}_{\xi_l}[\mathbf{E}_{\boldsymbol{\xi}_{\bar{l}}}(z \mid \xi_l)] + \mathbf{E}_{\xi_l}[\mathbf{D}_{\boldsymbol{\xi}_{\bar{l}}}(z \mid \xi_l)]. \tag{5.29}$$

Equation (5.29) can be transformed into

$$1 = \mathbf{D}_{\xi_l}[\mathbf{D}_{\boldsymbol{\xi}_{\bar{l}}}(z \mid \xi_l)] / \mathbf{D}_z(z) + \mathbf{E}_{\xi_l}[\mathbf{D}_{\boldsymbol{\xi}_{\bar{l}}}(z \mid \xi_l)] / \mathbf{D}_z(z). \tag{5.30}$$

The first item of (5.30) is the first-order sensitivity index (FSI) S_{ξ_l} of ξ_l. The second item of (5.30) is known as the total SI of $\boldsymbol{\xi}_{\bar{l}}$. S_{ξ_l} indicates the impact of ξ_l on z. Normally, S_{ξ_l} is calculated based on the time-consuming MCS [109, 160]. To save calculation time, the proposed PCE-based UPA method in Chapter 5.3 is applied to estimate S_{ξ_l}. Assuming that $\boldsymbol{\xi}^{(\boldsymbol{G_1})} = [\xi_l^{(G_1)}, \boldsymbol{\xi}_{\bar{l}}^{(\boldsymbol{G_1})}]$ and $\boldsymbol{\xi}^{(\boldsymbol{G_2})} = [\xi_l^{(G_2)}, \boldsymbol{\xi}_{\bar{l}}^{(\boldsymbol{G_2})}]$ are two independently sampled data of random variables and the response are $z^{(G_1)}$ and $z^{(G_2)}$, respectively, the estimated FSI $\hat{S}_{\xi_l}$ can be calculated as follows.

$$\begin{cases} \hat{\mathbf{E}}_{\hat{z}}(\hat{z}) = \sum_{m=1}^{N_{SI}} \hat{q}[v(\boldsymbol{\xi}_{\boldsymbol{(m)}}^{(\boldsymbol{G_1})})] / N_{SI} \\ \hat{\mathbf{D}}_{\hat{z}}(\hat{z}) = \sum_{m=1}^{N_{SI}} \hat{q}^2[v(\boldsymbol{\xi}_{\boldsymbol{(m)}}^{(\boldsymbol{G_1})})] / N_{SI} - \hat{\mathbf{E}}_{\hat{z}}(\hat{z})^2 \\ \hat{\mathbf{D}}_{\xi_l}(\hat{z}) = \sum_{m=1}^{N_{SI}} \hat{q}[v(\boldsymbol{\xi}_{\boldsymbol{(m)}}^{(\boldsymbol{G_1})})] \hat{q}[v(\xi_{l,(m)}^{(G_1)}, \boldsymbol{\xi}_{\boldsymbol{\bar{l},(m)}}^{(\boldsymbol{G_2})})] / N_{SI} - \hat{\mathbf{E}}_{\hat{z}}(\hat{z})^2 \end{cases} \tag{5.31}$$

$$\hat{S}_{\xi_l} = \hat{\mathbf{D}}_{\xi_l}(\hat{z}) / \hat{\mathbf{D}}_{\hat{z}}(\hat{z}) \tag{5.32}$$

where N_{SI} is the number of sampled data in G_1 or G_2. $v(.)$ represents the transformation from independent random variables to the dependent presented in Chapter 5.2.1.

The overall procedure of the comprehensive UQ method for power system frequency stability considering STCUs and FTCUs proposed in Chapter 5.2-Chapter 5.4 is summarized in Fig. 5.1. From Fig. 5.1, the inputs of the proposed UQ method are uncertainties, as external excitations, which are not affected by the inner structure of power systems. Thus, the proposed method is nonintrusive, the complexity of which is not affected by the structure of power systems.

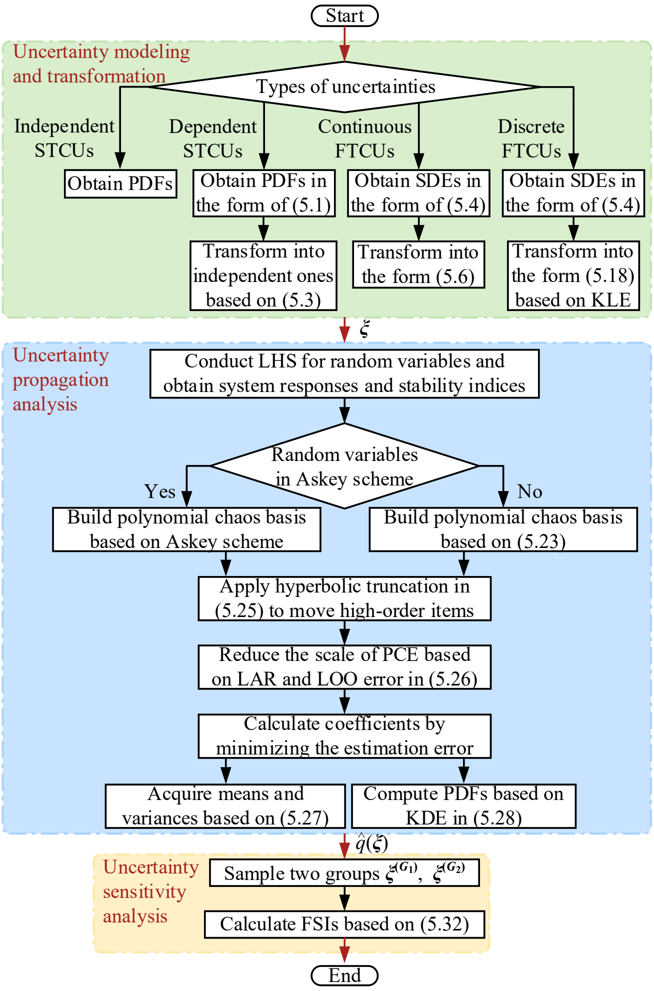

Fig. 5.1 Overall procedure of the comprehensive UQ method for power system frequency stability considering STCUs and FTCUs.

5.5 Case Study

5.5.1 Example System

Numerical results are conducted on the IEEE 39-bus benchmark system [21] to demonstrate the performance of the proposed UQ method. The simplified three-order synchronous generator model and first-order automatic voltage regulator model are utilized for simulations [30]. The concerned period of system dynamics is set as $T = 10$ s [97]. Eight STCUs and FTCUs of active power are injected. Ones at the buses with loads reflect uncertainties of loads, while others simulate the generation uncertainties. The uncertainties of PVs with slow and infrequent variations are modeled as STCUs formed by Beta distributions [103]. The uncertainties of WPGs with rapid and frequent fluctuations are modeled as FTCUs formed by SDEs with Wiener processes [112]. The uncertainties of loads with slow and infrequent variations are modeled as STCUs formed by Gaussian distributions [7], whereas those with rapid and frequent fluctuations are modeled as FTCUs formed by SDEs with compound Poisson processes [114]. The schematic and the detailed parameters are illustrated in Fig. 5.2 and Table 5.1, respectively.

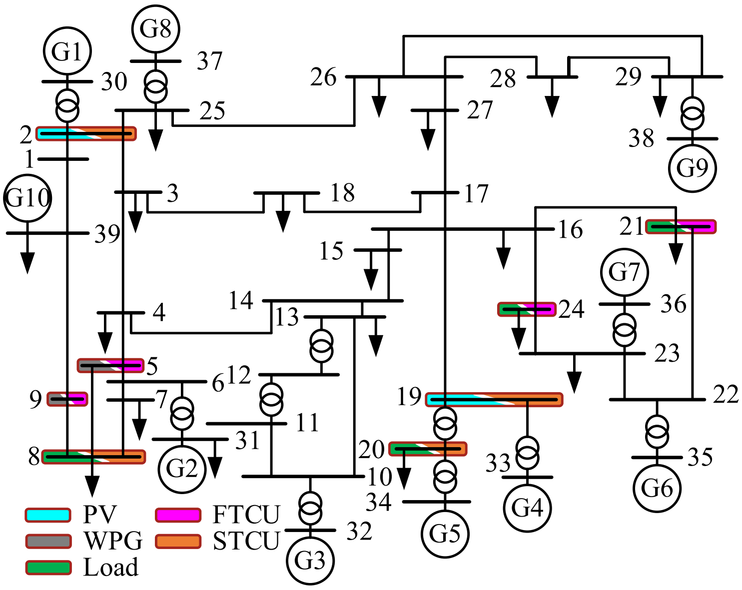

Fig. 5.2 Schematic of IEEE 39-bus system with STCUs.

Table 5.1 Parameters of uncertainties

Bus No.	Types	Uncertainty characteristics	Parameters
2, 19	PV	Independent STCU	$\xi_c \sim 2\times Beta(2, 3)$, $\rho_{\xi_c} = 0.7$
5, 9	WPG	Continuous FTCU	$\mu_{\xi_s} = -0.01$, $\sigma_{\xi_s} = 2$
8, 20	Load	Dependent STCU	$\xi_v \sim Gaussian(0, 1)$
21, 24	Load	Discrete FTCU	$\mu_{\xi_s} = 0$, $\sigma_{\xi_s} = 2$, $N_t \sim Poisson(0.6)$, $\varsigma \sim Gaussian(0,\ 0.2^2)$

5.5.2 Transformation Validation of Fast Timescale Characterizations of Uncertainties

Accurate transformation of FTCUs is the premise to ensure the effectiveness of UQ. Hence, the performance of FTCU transformation is verified firstly, where the root-mean square error (RMSE) [111] is introduced to compare the error of transformation.

The numerical results of the continuous Winner process W_t and discrete jump compound Poisson process C_t are presented in Fig. 5.3. As illustrated in Fig. 5.3(a) and Fig. 5.3(b), RMSEs keep reducing with the increase of the expansion order, which indicates that the higher the order of expansion is, the closer the transformation result is to the actual FTCUs.

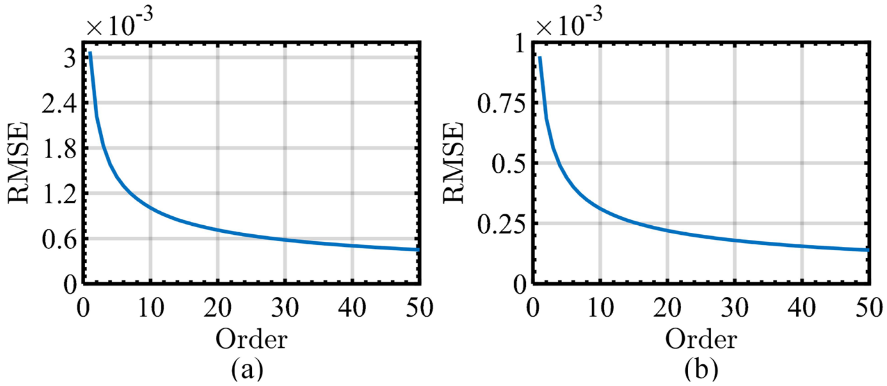

Fig. 5.3 (a) Change of RMSE with expansion order of W_t; (b) Change of RMSE with expansion order of C_t.

Moreover, to further quantify the errors of FTCU transformation, the PDFs of RMSE with different expansion orders are compared in Fig. 5.4. From Fig. 5.4(a) and Fig. 5.4(b), the PDF of RMSE with a higher expansion order has a thinner tail, which demonstrates a smaller variance. The decreasing variance and mean of RMSE with the increase of expansion order indicate the effectiveness of the proposed in the approximation of FTCUs.

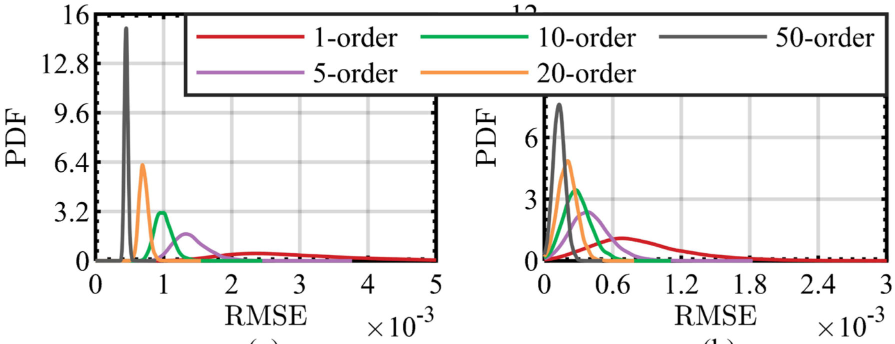

(a) (b)

Fig. 5.4 (a) PDF of expansion RMSE of W_t; (b) PDF of expansion RMSE of C_t.

Although using a high-order expansion will increase the accuracy, considering the computation time in the subsequent quantification, a relatively low-order expansion is more suitable under the premise of ensuring accuracy. From Fig. 5.5(a) and Fig. 5.5(b), 5-order and 10-order expansions are already close to the actual fluctuation of W_t and C_t, respectively. Thus, $I_W = 5$, $I_C = 10$ are chosen as the expansion order of W_t and C_t in the following calculation.

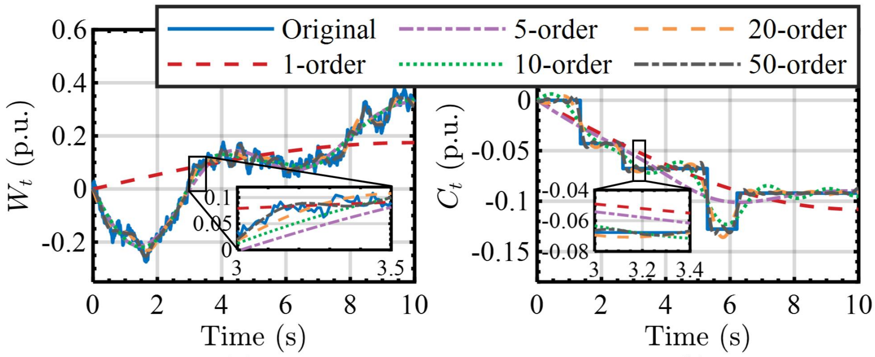

(a) (b)

Fig. 5.5 (a) Fitting results of W_t; (b) Fitting results of C_t.

5.5.3 Comprehensive Uncertainty Quantification Considering Different Timescale Characterizations of Uncertainties in Analyzing Frequency Stability

The proposed method is applied to conduct the frequency stability analysis where the generator with the largest output power is tripped from 0.1s. The results of 5000 times MCSs are considered as the baseline to present the performance of the proposed method [27]. The parameters are set as follows: $c_h = 0.8$, $N_o = 3$, $N_K = N_{SI} = 5000$, $N_s = 200$ [103]. Also, the results of Halton QMCS and Sobol QMCS are presented to compare with the proposed method, the sampled data number of which is selected as 500. The PDF results of FN and RoCoF are presented in Fig. 5.6, and the performance of the proposed method is listed in Table 5.2. From Table 5.2 and Fig. 5.6, the maximal error of e_μ and e_σ is 5.44%, whereas that of Halton and Sobol are 10.39% and 9.04%, respectively. Compared with Halton and Sobol, PDFs calculated by the proposed method have higher overlaps with the actual PDFs. And the computation time of the proposed method is shortened by more than 25 times than MCS and more than 2.5 times than Halton and Sobol, showing the accuracy of the proposed method in quantifying frequency stability indices affected by uncertainties and the time-saving merit.

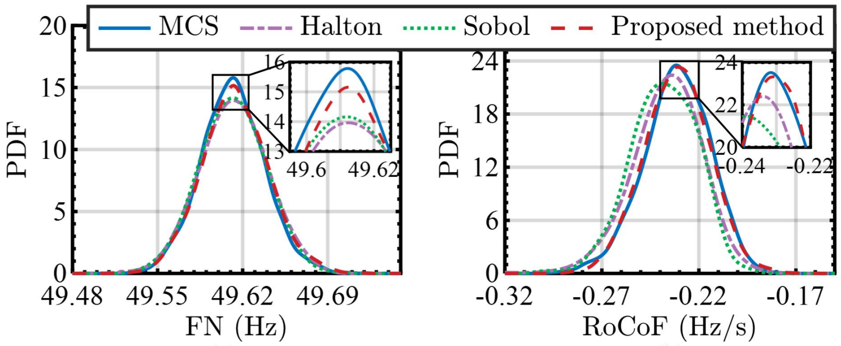

(a)

(b)

Fig. 5.6 PDF results of frequency stability indices: (a) PDF of FN; (b) PDF of RoCoF.

Table 5.2 Performance of different methods in the calculation of frequency stability indices

Method	e_{μ} ($\times 10^{-2}$%)	e_{σ} (%)	t_S (s)	t_M (s)	t_T (s)
MCS	–	–	4181.66	–	4181.66
Halton	2.34	10.39	413.66	0.31	413.97
Sobol	3.03	9.04	413.70	0.47	414.17
Proposed method	0.05	5.44	160.26	3.67	163.93

Similarly, quantification results of the dynamic response of f_{sys} affected by uncertainties are computed and shown in Fig. 5.7. From Fig. 5.7(a), the curve of the mean of f_{sys} calculated by the proposed method and that obtained from the MCS are nearly overlapped. Moreover, the MAPE PDF of the mean of f_{sys} derived from the proposed method has a thinner tail and taller peak close to 0 compared with those from Halton and Sobol. Although the MAPE PDF peaks of the Std. of f_{sys} from the proposed method, Halton, and Sobol are near, the PDF tail from the proposed method ends closer to 0. Thus, the proposed method presents a higher accuracy in quantifying the total trend of f_{sys}.

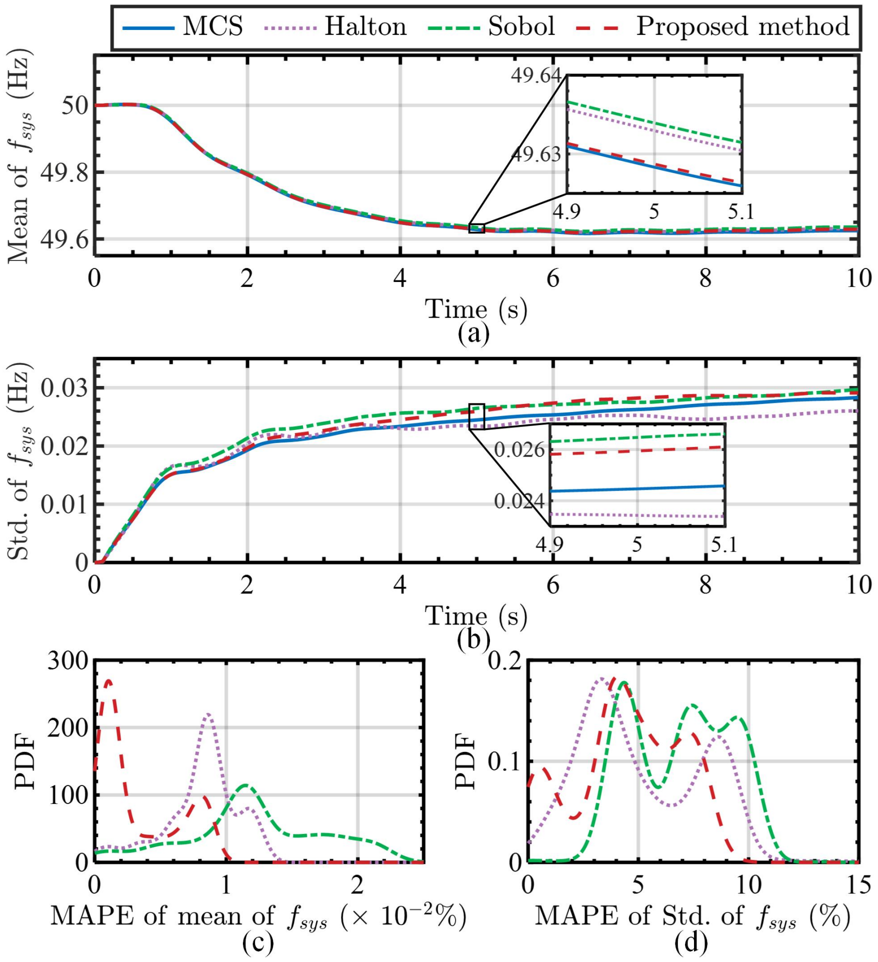

Fig. 5.7 Statistical results of frequency: (a) Mean of f_{sys}; (b) Std. of f_{sys}; (c) MAPE of mean of f_{sys}; (d) MAPE of Std. of f_{sys}.

Besides, the PDFs of f_{sys} are calculated based on the proposed method. For saving space, f_{sys} at $t = 3\text{s}$ and $t = 6\text{s}$ are presented in Fig. 5.8(a) and Fig. 5.8(b) as examples. From Fig. 5.8, the PDFs of f_{sys} at different time points from the proposed method also have a higher overlap than those from Halton and Sobol, indicating the good performance of the proposed method in quantifying f_{sys} at different time points.

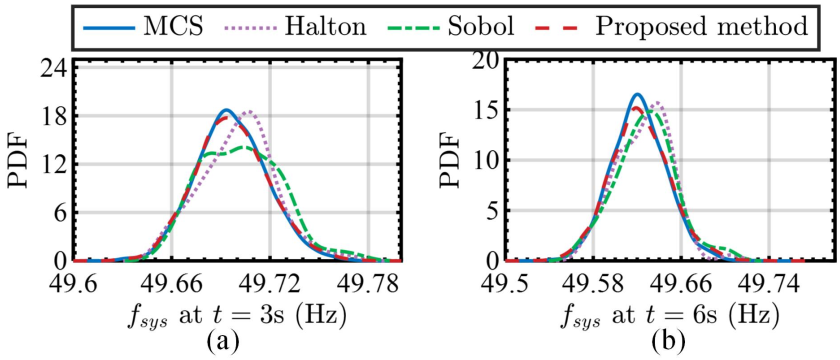

Fig. 5.8 (a) PDF of f_{sys} at 3s; (b) PDF of f_{sys} at 6s.

Finally, the sensitivities of FN and RoCoF with respect to uncertainties are calculated to quantify the impact of uncertainties on the frequency stability. Table 5.3 and Fig. 5.9 present the performance and results of the proposed method in calculating the FSI of FN and RoCoF separately.

Table 5.3 Performance of different methods in the FSI calculation of frequency stability indices

Method	e_{FSI} ($\times10^{-2}$)	t_T (s)
MCS	–	18834.11
Halton	13.11	1880.08
Sobol	17.69	1880.76
Proposed method	2.01	17.91

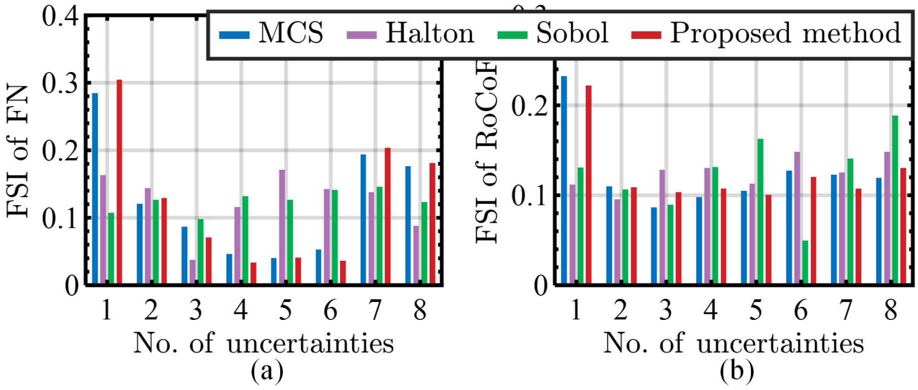

Fig. 5.9 FSI results of frequency stability indices: (a) FSI of FN; (b) FSI of RoCoF.

From Table 5.3, the calculation time of the proposed method is reduced by more than 1000 times compared to that of MCS and more than 100 times compared to that of Halton and Sobol. Although there is a deviation between the FSIs of STCU and FTCU in Bus 9 and 20 estimated by the proposed method and those based on the MCS in Fig. 5.9(a), since these FSIs are tiny, the same results can be obtained from the proposed method and the MCS, i.e., STCU and FTCU in Bus 9 and 20 have little effect on the FN. Besides, the maximal RMSE of frequency stability indices of the proposed method is 0.0201, which is much lower than those of Halton (0.1311) and Sobol (0.1769), illustrating the effectiveness of the proposed method in frequency stability analysis. Moreover, from Fig. 5.9, for FN, the STCU in Bus 2 has the highest FSI, and FSIs corresponding to FTCUs in Bus 21 and 24 also have relatively high values. Apart from them, STCU and FTCU in Bus 19 and 5 also affect FN, and the impact of others is limited. For RoCoF, all FSIs corresponding to STCUs and FTCUs have relatively remarkable values, which indicates that all STCUs and FTCUs affect RoCoF and frequency stability, and among them, the STCU in Bus 2 has the most serious impact. Thus, the results also reflect the limitation of only considering the STCUs or FTCUs in current research. Both the STCUs and FTCUs have a significant impact on system stability. Considering only one timescale characterization type of uncertainties is inaccurate and not in line with the actual operation state of power systems. Thus, it is necessary to consider STCUs and FTCUs in the dynamics of power systems.

5.6 Summary

In this chapter, firstly, STCUs are formulated by probability distribution methods. FTCUs formulated by stochastic processes are approximated by the superposition of the finite number of STCUs based on KLE so that STCUs and FTCUs are firstly transformed into a unified form modeled by probability distribution methods. Then, to effectively quantify the relationship between the power system frequency stability and STCUs and FTCUs, the scalable PCE is proposed. Moreover, sensitivity analysis is conducted to study the impact of STCUs and FTCUs on power system frequency stability. The results of case studies demonstrate the effectiveness of the proposed method and reveal the necessity of considering STCUs and FTCUs in UQ for power system frequency stability.

Chapter 6 Conclusions and Suggestions for Future Research

6.1 Conclusions

Since sustainable development has become a widespread concern recently, RPGs have been widely installed in power systems, which contributes to the high penetration of renewable energies in modern power systems. However, the uncertainties of RPGs and the decreasing inertia of power systems caused by the integration of large-scale RPGs degrade the power system frequency stability. And there is a pressing need to quantify the impact of RPG uncertainties on frequency stability. Therefore, this thesis proposes a series of UQ methods for frequency stability, the conclusions of which are drawn as follows.

1) Study on PFSA Considering Dynamics of RPGs with Different Control Strategies

(1) When considering different control strategies of RPGs in frequency response, the RPGs with VSG-based grid-forming control strategy can provide inertia to the system, while RPGs with conventional grid-following control strategy cannot, thereby changing the frequency response of the system. Thus, considering the different control strategies of RPGs is necessary for PFSA.

(2) When considering the dynamics of RPGs in frequency response, the explicit solution of FN/FV and RoCoF time of the SFR model no longer exists. Thus, the closed-form relationship between frequency stability indices and outputs of RPGs cannot be derived. The difficulty of analyzing probabilistic frequency stability increases, and a novel UPA method is required.

(3) The simulation results illustrate that two PDFs with the limited number of similar moments may have significant differences in shapes, while PDFs with similar shapes may also have great differences in their finite number of moments. Thus, even if the finite moments calculated by moment-based methods are within an acceptable error range, the accuracy of PDFs generated by moment-based methods cannot be guaranteed, which is the limitation of moment-based UPA methods. By comparison, the proposed MIS-MELRA is an approximation method, avoiding the limitations of moment-based methods.

(4) The proposed MIS-MELRA can effectively analyze the frequency stability considering the dynamics of RPGs. The utilization of LRA contributes to the proposed method being suitable for large-scale uncertainty analysis. The proposed MIS greatly reduces the simulation time, while the introduction of ME considers different trends of frequency response, thereby improving the accuracy of PFSA.

2) Study on PFSA Considering WEs of WFs

(1) Compared with the numerical uncertainty propagation analysis methods, the proposed MOGPR greatly improves the efficiency of PFSA. Compared with GPR, MOGPR can simultaneously analyze the probabilistic stability of system frequency and

area-level frequency and consider the relationship among them with higher efficiency and accuracy. Compared with other approximation methods, both MOGPR and GPR only require sampling data, which are more suitable for analyzing uncertainties with complicated correlations, including the WEs of WFs.

(2) Compared with conventional analytical WE models, the proposed WE model considers multiple factors, which can reflect the WEs of WFs more realistically and can be easily integrated into PFSA. Also, the time cost of the proposed model is greatly shorter than that of the frequency response simulation, which is suitable for PFSA.

(3) The impacts of multiple factors related to WEs on PFSA are studied. The results of case studies reveal that the change of the wind direction, the terrain, and the layout will contribute to the change of the WE strength. And a lower wind speed deficit and a higher level of nature wind speed will lead to higher WPG penetrations, more obvious power fluctuations of WTs, and more distributed PDFs of frequency stability indices, increasing the probability of frequency in high and medium-risk regions of instability.

(4) The necessity and significance of considering the WEs of WFs in PFSA are revealed based on case studies. The ignorance of the WEs of WFs in PFSA will result in a higher probability of frequency instability, which is inaccurate and leads to a conservative frequency regulation strategy and increased frequency reserve costs. To mitigate the degradation of probabilistic frequency stability caused by WPG uncertainties considering WEs, additional frequency regulation control for WTs can be adopted based on PFSA results.

3) Study on PFSA Aiming at Frequency Response Trajectories

(1) A generic transformation method for correlated uncertainties based on ICA is proposed, which can effectively transform uncertainties with complicated correlations into independent ones. Thus, it can be integrated into other PCE-based UPA methods, which require independent uncertainties as inputs.

(2) The proposed GMPCE has multiple outputs and thus can quantify the frequency response trajectory at different time points simultaneously, which greatly improves efficiency. Additionally, GMPCE possesses other merits, i.e., being applicable to uncertainties with arbitrary probability distributions and avoiding the curse of dimensionality. It can be expected that GMPCE can be applied not only in system dynamic response trajectory at multiple time points but also in multiple concerned system indicators.

4) Study on Comprehensive UQ for Frequency Stability Considering Different Timescale Characterizations of Uncertainties

(1) FTCUS formulated by stochastic processes can be approximated by the superposition of the limited number of STCUs formulated by probability distribution methods based on KLE. Thus, STCUs and FTCUs can be expressed by only applying probability distribution methods without stochastic process methods.

(2) The proposed UQ method is based on the scalable PCE, which is suitable for uncertainties with arbitrary distributions and can prevent the curse of dimensionality. Additionally, sensitivity analysis provides a reference for locating the uncertainties that significantly affect the system dynamics. The numerical results of case studies illustrate that the proposed method has high accuracy and significantly reduces the computation

time. Moreover, the results of sensitivity analysis indicate the necessity of considering the STCUs and FTCUs in the frequency stability of power systems.

(3) The proposed UQ method has wide applications in power system dynamics since most of the uncertainties in power systems can be formulated as STCUs or FTCUs. In addition, the frequency stability issue conducted in the case studies is just an example scenario of the proposed UQ method, which can be extended to other stability issues related to system dynamics.

6.2 Suggestions for Future Research

This thesis has proposed a series of UQ methods for frequency stability of renewable penetrated power systems. To enrich the current work, the following research topics are suggested and deserve to be investigated in the future.

1) Since the proposed methods are data-based methods, how to use less data to achieve accurate analysis needs to be studied. Also, the improvement of robustness to data quality and quantity, scalability to different types of uncertainties and system scale, and accuracy guarantee within an acceptable range in different scenarios deserve to be studied.

2) Apart from frequency stability, there are other stability issues of power systems that need to be concerned. It is necessary to investigate the impact of uncertainties on other stability issues and propose methods to quantify the impact on multi-stability simultaneously.

3) Studies in this thesis only focus on the frequency stability of AC transmission power systems. Thus, UQ for other types of power systems is also necessary, such as AC/DC systems, distribution systems, microgrids, and cyber physical power systems.

4) With the development of RPGs, apart from WPGs and PVs, novel forms of RPGs have been gradually integrated into modern power systems. Developing uncertainty modeling and quantification methods targeting these novel RPGs is one of the research topics in the future. Also, specific combined impacts of STCUs and FTCUs, as well as their separate impacts, deserve to be further studied since only the sensitivities associated with uncertainties are calculated in the thesis.

5) Studies in this thesis only give the impacts of uncertainties on frequency stability, which is not enough to provide guidance for the system operators to tackle these uncertainties. Hence, frequency stability enhancement strategies based on the results derived in this thesis need to be developed.

6) System planning considering the frequency stability affected by RPG uncertainties and the operational efficiency improvement of RPGs based on the proposed methods in this thesis deserve to be investigated, for example, RPG siting, sizing, and coordinated control.

7) Studies in this thesis only reveal the necessity of considering RPG dynamics in PFSA. Thus, the comprehensive comparison on the impact of different control strategies of RPGs on probabilistic frequency stability based on the proposed methods in this thesis is needed, which could provide guidance in selecting the optimal control strategy for enhancing probabilistic frequency stability.

8) Apart from existing frequency stability indices, including FN, FV, and RoCoF, inertia is one of the major factors affecting system stability and can provide additional information to indicate system states related to frequency. Thus, novel frequency stability indices associated with inertia deserve to be studied and designed to assist in analyzing probabilistic frequency stability.

References

[1] X. Yu and Y. Xue, “Smart grids: A cyber–physical systems perspective,” *Proceedings of the IEEE*, vol. 104, no. 5, pp. 1058-1070, May 2016.

[2] R. Jing, Y. Zhou, and J. Wu, “Empowering zero-carbon future-experience and development trends of electric power system transition in the UK,” *Automation of Electric Power Systems*, vol. 45, no. 16, pp. 87-98, Aug. 2021.

[3] H. Yang, B. Chen, S. Xiang, J. Liu, and E. Ackom, “Distributionally robust optimal dispatch modelling of renewable-dominated power system and implementation path for carbon peak,” *Computers & Industrial Engineering*, vol. 163, p. 107797, Jan. 2022.

[4] REN21, “Renewable 2024 global status report,” Paris, France, 2024.

[5] IEA, “Renewable energy market update outlook for 2023 and 2024,” Paris, France, 2023.

[6] R. Fatah Mochamad, R. Preece, and K. N. Hasan, “Probabilistic multi-stability operational boundaries in power systems with high penetration of power electronics,” *International Journal of Electrical Power & Energy Systems*, vol. 135, p. 107382, Feb. 2022.

[7] K. N. Hasan, R. Preece, and J. V. Milanović, “Existing approaches and trends in uncertainty modelling and probabilistic stability analysis of power systems with renewable generation,” *Renewable and Sustainable Energy Reviews*, vol. 101, pp. 168-180, Mar. 2019.

[8] L. Xiong, X. Liu, Y. Liu, and F. Zhuo, “Modeling and stability issues of voltage-source converter-dominated power systems: A review,” *CSEE Journal of Power and Energy Systems*, vol. 8, no. 6, pp. 1530-1549, Nov. 2022.

[9] P. Kundur et al., “Definition and classification of power system stability

IEEE/CIGRE joint task force on stability terms and definitions," *IEEE Transactions on Power Systems*, vol. 19, no. 3, pp. 1387-1401, May 2004.

[10] NESO, "Technical report on the events of 9 august 2019," 2019.

[11] J. Huang, Z. Yang, J. Yu, L. Xiong, and Y. Xu, "Frequency dynamics-constrained parameter design for fast frequency controller of wind turbine," *IEEE Transactions on Sustainable Energy*, vol. 13, no. 1, pp. 31-43, Jan. 2022.

[12] M. J. Sanjari and H. B. Gooi, "Probabilistic forecast of PV power generation based on higher order Markov chain," *IEEE Transactions on Power Systems*, vol. 32, no. 4, pp. 2942-2952, Jul. 2017.

[13] Y. Gao et al., "Analytical probabilistic power flow and global sensitivity analysis of distribution systems based on Gaussian mixture model of input-output variables," *IEEE Transactions on Power Systems*, vol. 3, no. 9, pp. 5283-5296, May 2024.

[14] M. Fan et al., "Uncertainty evaluation algorithm in power system dynamic analysis with correlated renewable energy sources," *IEEE Transactions on Power Systems*, vol. 36, no. 6, pp. 5602-5611, Nov. 2021.

[15] B. Qi, K. N. Hasan, and J. V. Milanović, "Identification of critical parameters affecting voltage and angular stability considering load-renewable generation correlations," *IEEE Transactions on Power Systems*, vol. 34, no. 4, pp. 2859-2869, Jan. 2019.

[16] Z. S. Zhang, Y. Z. Sun, D. W. Gao, J. Lin, and L. Cheng, "A versatile probability distribution model for wind power forecast errors and its application in economic dispatch," *IEEE Transactions on Power Systems*, vol. 28, no. 3, pp. 3114-3125, Mar. 2013.

[17] C. Tang et al., "Look-ahead economic dispatch with adjustable confidence interval based on a truncated versatile distribution model for wind power," *IEEE Transactions on Power Systems*, vol. 33, no. 2, pp. 1755-1767, Jun. 2018.

[18] M. Ebeed and S. H. E. A. Aleem, "Overview of uncertainties in modern power systems: Uncertainty models and methods," in *Uncertainties in modern power*

systems, Cambridge, Massachusetts, USA: Academic Press, 2021, pp. 3-7.

[19] B. R. Prusty and D. Jena, "A critical review on probabilistic load flow studies in uncertainty constrained power systems with photovoltaic generation and a new approach," *Renewable and Sustainable Energy Reviews*, vol. 69, pp. 1286-1302, Mar. 2017.

[20] G. Mavromatidis, K. Orehounig, and J. Carmeliet, "A review of uncertainty characterisation approaches for the optimal design of distributed energy systems," *Renewable and Sustainable Energy Reviews*, vol. 88, pp. 258-277, May 2018.

[21] S. Bu, J. Wen, and F. Li, "A generic framework for analytical probabilistic assessment of frequency stability in modern power system operational planning," *IEEE Transactions on Power Systems*, vol. 34, no. 5, pp. 3973-3976, Sept. 2019.

[22] J. Wen, S. Bu, F. Li, and P. Du, "Risk assessment and mitigation on area-level RoCoF for operational planning," *Energy*, vol. 228, p. 120632, Aug. 2021.

[23] J. Wen, S. Bu, and H. Xin, "Probabilistic assessment on area-level frequency nadir/vertex for operational planning," *IEEE Open Access Journal of Power and Energy*, vol. 8, pp. 341-351, Aug. 2021.

[24] J. Wen, S. Bu, B. Zhou, Q. Chen, and D. Yang, "A fast-algorithmic probabilistic evaluation on regional rate of change of frequency (RoCoF) for operational planning of high renewable penetrated power systems," *Energies*, vol. 13, no. 11, p. 2780, Jun. 2020.

[25] Q. Chen, S. Bu, and J. Wen, "Clustering-based two-stage probabilistic small-signal stability analysis of power systems with uncertainties," in *IEEE Power & Energy Society General Meeting*, Orlando, FL, USA, 2023, pp. 1-5.

[26] J. Wen, S. Bu, and F. Li, "Two-level ensemble methods for efficient assessment and region visualization of maximal frequency deviation risk," *IEEE Transactions on Power Systems*, vol. 38, no. 1, pp. 643-655, Mar. 2023.

[27] S. Q. Bu, W. Du, H. F. Wang, Z. Chen, L. Y. Xiao, and H. F. Li, "Probabilistic analysis of small-signal stability of large-scale power systems as affected by

penetration of wind generation," *IEEE Transactions on Power Systems*, vol. 27, no. 2, pp. 762-770, May 2012.

[28] S. Q. Bu, W. Du, and H. F. Wang, "Probabilistic analysis of small-signal rotor angle/voltage stability of large-scale AC/DC power systems as affected by grid-connected offshore wind generation," *IEEE Transactions on Power Systems*, vol. 28, no. 4, pp. 3712-3719, Nov. 2013.

[29] S. Q. Bu, W. Du, and H. F. Wang, "Investigation on probabilistic small-signal stability of power systems as affected by offshore wind generation," *IEEE Transactions on Power Systems*, vol. 30, no. 5, pp. 2479-2486, Sept. 2015.

[30] J. Luo, S. Bu, J. Zhu, and C. Y. Chung, "Modal shift evaluation and optimization for resonance mechanism investigation and mitigation of power systems integrated with FCWG," *IEEE Transactions on Power Systems*, vol. 35, no. 5, pp. 4046-4055, Sept. 2020.

[31] J. Luo, Y. Zou, S. Bu, and U. Karaagac, "Converter-driven stability analysis of power systems integrated with hybrid renewable energy sources," *Energies*, vol. 14, no. 14, p. 4290, Jul. 2021.

[32] J. Luo, S. Bu, and C. Y. Chung, "Design and comparison of auxiliary resonance controllers for mitigating modal resonance of power systems integrated with wind generation," *IEEE Transactions on Power Systems*, vol. 36, no. 4, pp. 3372-3383, Jan. 2021.

[33] W. Du, H. Wang, and S. Bu, "Linearized model of a power system with a grid-connected variable speed wind generator," in *Small-signal stability analysis of power systems integrated with variable speed wind generators*, Cham, Switzerland: Springer, 2018, pp. 27-40.

[34] H. Wu et al., "Small-signal modeling and parameters design for virtual synchronous generators," *IEEE Transactions on Industrial Electronics*, vol. 63, no. 7, pp. 4292-4303, Jul. 2016.

[35] H. Liu, D. Sun, P. Song, X. Cheng, F. Zhao, and Y. Tian, "Influence of virtual synchronous generators on low frequency oscillations," *CSEE Journal of Power*

and Energy Systems, vol. 8, no. 4, pp. 1029-1038, Jul. 2022.

[36] H. Fang and Z. Yu, “Improved virtual synchronous generator control for frequency regulation with a coordinated self-adaptive method,” *CSEE Journal of Power and Energy Systems*, vol. 10, no. 1, pp. 175-184, Jan. 2024.

[37] M. Chen, D. Zhou, and F. Blaabjerg, “High penetration of inverter-based power sources with VSG control impact on electromechanical oscillation of power system,” *International Journal of Electrical Power & Energy Systems*, vol. 142, p. 108370, Nov. 2022.

[38] Z. Shuai, C. Shen, X. Liu, Z. Li, and Z. J. Shen, “Transient angle stability of virtual synchronous generators using Lyapunov’s direct method,” *Transient Angle Stability of Virtual Synchronous Generators Using Lyapunov’s Direct Method*, vol. 10, no. 4, pp. 4648-4661, Jul. 2019.

[39] W. Du, W. Dong, Y. Wang, and H. Wang, “Small-disturbance stability of a wind farm with virtual synchronous generators under the condition of weak grid connection,” *IEEE Transactions on Power Systems*, vol. 36, no. 6, pp. 5500-5511, Nov. 2021.

[40] K. Shi, Y. Wang, Y. Sun, P. Xu, and F. Gao, “Frequency-coupled impedance modeling of virtual synchronous generators,” *IEEE Transactions on Power Systems*, vol. 36, no. 4, pp. 3692-3700, Jul. 2021.

[41] J. Xi, H. Geng, and X. Zou, “Decoupling scheme for virtual synchronous generator controlled wind farms participating in inertial response,” *Journal of Modern Power Systems and Clean Energy*, vol. 9, no. 2, pp. 347-355, Mar. 2021.

[42] J. Xi and H. Geng, “Decoupling control scheme for VSG-wpps to participate in grid frequency response,” *IEEE Transactions on Industry Applications*, vol. 55, no. 6, pp. 6368-6375, Nov./Dec. 2019.

[43] J. Wang, F. Li, H. Cui, and Q. Zhang, “Impacts of VSG control on frequency response in power systems with high-penetration renewables,” in *IEEE 5th Conference on Energy Internet and Energy System Integration*, Taiyuan, China, 2021, pp. 171-176.

[44] A. Fu et al., “Impact of virtual synchronous generators on power system frequency dynamics,” in *International Conference on Smart Energy Systems and Technologies*, Mugla, Turkiye, 2023, pp. 1-6.

[45] Z. Sun, D. Ma, and S. Li, “An oscillation damping method for frequency-detector-less virtual synchronous generators,” *Energy Reports*, vol. 7, pp. 1485-1494, Nov. 2021.

[46] T. T. Tran and D.-H. Kim, “A CFD study into the influence of unsteady aerodynamic interference on wind turbine surge motion,” *Renewable Energy*, vol. 90, pp. 204-228, May 2016.

[47] J. Thé and H. Yu, “A critical review on the simulations of wind turbine aerodynamics focusing on hybrid RANS-LES methods,” *Energy*, vol. 138, pp. 257-289, Nov. 2017.

[48] M. Ye, H.-C. Chen, and A. Koop, “High-fidelity CFD simulations for the wake characteristics of the NTNU BT1 wind turbine,” *Energy*, vol. 265, p. 126285, Feb. 2023.

[49] J. N. O., “A note on wind generator interaction,” Tech. Rep. Ris-M-2411, 1983.

[50] X. Han, Y. Qu, P. Wang, and J. Yang, “Four-dimensional wind speed model for adequacy assessment of power systems with wind farms,” *IEEE Transactions on Power Systems*, vol. 28, no. 3, pp. 2978-2985, Aug. 2013.

[51] X. Lyu, Y. Jia, and Z. Xu, “A novel control strategy for wind farm active power regulation considering wake interaction,” *IEEE Transactions on Sustainable Energy*, vol. 11, no. 2, pp. 618-628, Apr. 2020.

[52] S. Frandsen et al., “Analytical modelling of wind speed deficit in large offshore wind farms," *Wind Energy*, vol. 9, no. 1-2, pp. 39-53, Jan. 2006.

[53] M. Bastankhah and F. Porté-Agel, “A new analytical model for wind-turbine wakes,” *Renewable Energy*, vol. 70, pp. 116-123, Oct. 2014.

[54] W. Xiang, P. Zhou, L. Ban, M. Zhang, Z. Xiang, and R. Huang, “Equivalent modeling of wind farms considering wake effects and analysis of probability of sub-synchronous oscillations,” in *International Conference on Power System*

Technology, Haikou, China, 2021, pp. 91-98.

[55] M. H. Johnson and D. C. Aliprantis, "Analysis of series-DC offshore wind plants with aerodynamic wake effects," *IEEE Transactions on Sustainable Energy*, vol. 8, no. 4, pp. 1706-1714, Oct. 2017.

[56] A. P. Gupta, A. Mitra, A. Mohapatra, and S. N. Singh, "A multi-machine equivalent model of a wind farm considering LVRT characteristic and wake effect," *IEEE Transactions on Sustainable Energy*, vol. 13, no. 3, pp. 1396-1407, Jul. 2022.

[57] L. Xiong et al., "Optimal allocation of energy storage system in DFIG wind farms for frequency support considering wake effect," *IEEE Transactions on Power Systems*, vol. 37, no. 3, pp. 2097-2112, May 2022.

[58] M. Ali, I. S. Ilie, J. V. Milanovic, and G. Chicco, "Wind farm model aggregation using probabilistic clustering," *IEEE Transactions on Power Systems*, vol. 28, no. 1, pp. 309-316, Feb. 2013.

[59] Z. Xinyan and W. Weiqing, "Wind farm and wake effect modeling for simulation of a studied power system," in *IEEE/PES Power Systems Conference and Exposition*, Seattle, WA, USA, 2009, pp. 1-6.

[60] P. Wang, Z. Zhang, Q. Huang, N. Wang, X. Zhang, and W. J. Lee, "Improved wind farm aggregated modeling method for large-scale power system stability studies," *IEEE Transactions on Power Systems*, vol. 33, no. 6, pp. 6332-6342, Nov. 2018.

[61] M. Aien, A. Hajebrahimi, and M. Fotuhi-Firuzabad, "A comprehensive review on uncertainty modeling techniques in power system studies," *Renewable and Sustainable Energy Reviews*, vol. 57, pp. 1077-1089, May 2016.

[62] A. Ehsan and Q. Yang, "State-of-the-art techniques for modelling of uncertainties in active distribution network planning: A review," *Applied Energy*, vol. 239, pp. 1509-1523, Apr. 2019.

[63] A. M. Hakami, K. N. Hasan, M. Alzubaidi, and M. Datta, "A review of uncertainty modelling techniques for probabilistic stability analysis of

renewable-rich power systems," *Energies*, vol. 16, no. 1, p. 112, Dec. 2023.

[64] A. R. Jordehi, "How to deal with uncertainties in electric power systems? A review," *Renewable and Sustainable Energy Reviews*, vol. 96, pp. 145-155, Nov. 2018.

[65] V. Singh, T. Moger, and D. Jena, "Uncertainty handling techniques in power systems: A critical review," *Electric Power Systems Research*, vol. 203, p. 107633, Feb. 2022.

[66] U. H. Ramadhani, M. Shepero, J. Munkhammar, J. Widén, and N. Etherden, "Review of probabilistic load flow approaches for power distribution systems with photovoltaic generation and electric vehicle charging," *International Journal of Electrical Power & Energy Systems*, vol. 120, p. 106003, Sept. 2020.

[67] M. Aien, M. Rashidinejad, and M. Fotuhi-Firuzabad, "On possibilistic and probabilistic uncertainty assessment of power flow problem: A review and a new approach," *Renewable and Sustainable Energy Reviews*, vol. 37, pp. 883-895, Sept. 2014.

[68] R. H. A. Zubo, G. Mokryani, H.-S. Rajamani, J. Aghaei, T. Niknam, and P. Pillai, "Operation and planning of distribution networks with integration of renewable distributed generators considering uncertainties: A review," *Renewable and Sustainable Energy Reviews*, vol. 72, pp. 1177-1198, May 2017.

[69] X. Yue, S. Pye, J. DeCarolis, F. G. N. Li, F. Rogan, and B. Ó. Gallachóir, "A review of approaches to uncertainty assessment in energy system optimization models," *Energy Strategy Reviews*, vol. 21, pp. 204-217, Aug. 2018.

[70] M. A. Lasemi, A. Arabkoohsar, A. Hajizadeh, and B. Mohammadi-ivatloo, "A comprehensive review on optimization challenges of smart energy hubs under uncertainty factors," *Renewable and Sustainable Energy Reviews*, vol. 160, p. 112320, May 2022.

[71] W. Tian et al., "A review of uncertainty analysis in building energy assessment," *Renewable and Sustainable Energy Reviews*, vol. 93, pp. 285-301, Oct. 2018.

[72] H. Li et al., "A review of scenario analysis methods in planning and operation

of modern power systems: Methodologies, applications, and challenges," *Electric Power Systems Research*, vol. 205, p. 107722, Apr. 2022.

[73] T. M. Alabi et al., "A review on the integrated optimization techniques and machine learning approaches for modeling, prediction, and decision making on integrated energy systems," *Renewable Energy*, vol. 194, pp. 822-849, Jul. 2022.

[74] M. Aien, M. Rashidinejad, and M. F. Firuz-Abad, "Probabilistic optimal power flow in correlated hybrid wind-PV power systems: A review and a new approach," *Renewable and Sustainable Energy Reviews*, vol. 41, pp. 1437-1446, Jan. 2015.

[75] A. Zakaria, F. B. Ismail, M. S. H. Lipu, and M. A. Hannan, "Uncertainty models for stochastic optimization in renewable energy applications," *Renewable Energy*, vol. 145, pp. 1543-1571, Jan. 2020.

[76] J. Xu, P. K. Kanyingi, K. Wang, G. Li, B. Han, and X. Jiang, "Probabilistic small signal stability analysis with large scale integration of wind power considering dependence," *Renewable and Sustainable Energy Reviews*, vol. 69, pp. 1258-1270, Mar. 2017.

[77] D. Issicaba, J. A. P. Lopes, and M. A. d. Rosa, "Adequacy and security evaluation of distribution systems with distributed generation," *IEEE Transactions on Power Systems*, vol. 27, no. 3, pp. 1681-1689, Aug. 2012.

[78] K. Ye, J. Zhao, H. Zhang, and Y. Zhang, "Data-driven probabilistic voltage risk assessment of MiniWECC system with uncertain PVs and wind generations using realistic data," *IEEE Transactions on Power Systems*, vol. 37, no. 5, pp. 4121-4124, Sept. 2022.

[79] M. Aien, M. Fotuhi-Firuzabad, and F. Aminifar, "Probabilistic load flow in correlated uncertain environment using unscented transformation," *IEEE Transactions on Power Systems*, vol. 27, no. 4, pp. 2233-2241, Nov. 2012.

[80] R. Preece, K. Huang, and J. V. Milanović, "Probabilistic small-disturbance stability assessment of uncertain power systems using efficient estimation methods," *Probabilistic Small-Disturbance Stability Assessment of Uncertain*

Power Systems Using Efficient Estimation Methods, vol. 29, no. 5, pp. 2509-2517, Mar. 2014.

[81] X. Xu, T. Lin, and X. Zha, "Probabilistic analysis of small signal stability of microgrid using point estimate method," in *International Conference on Sustainable Power Generation and Supply*, Nanjing, China, 2009, pp. 1-6.

[82] L. Li, H. Jiang, P. Yang, P. Fan, P. Qi, and L. Kang, "Small signal stability analysis and optimize control of large-scale wind power collection system," *IEEE Access*, vol. 10, pp. 28842-28852, Mar. 2022.

[83] A. Schellenberg, W. Rosehart, and J. A. Aguado, "Cumulant-based stochastic nonlinear programming for variance constrained voltage stability analysis of power systems," *IEEE Transactions on Power Systems*, vol. 21, no. 2, pp. 579-585, May 2006.

[84] J. M. Morales and J. Perez-Ruiz, "Point estimate schemes to solve the probabilistic power flow," *IEEE Transactions on Power Systems*, vol. 22, no. 4, pp. 1594-1601, Nov. 2007.

[85] H. Wu, Y. Zhou, S. Dong, and Y. Song, "Probabilistic load flow based on generalized polynomial chaos," *IEEE Transactions on Power Systems*, vol. 32, no. 1, pp. 820-821, Jan. 2017.

[86] T. Mühlpfordt, L. Roald, V. Hagenmeyer, T. Faulwasser, and S. Misra, "Chance-constrained AC optimal power flow: A polynomial chaos approach," *IEEE Transactions on Power Systems*, vol. 34, no. 6, pp. 4806-4816, Nov. 2019.

[87] G. Wang, H. Xin, D. Wu, P. Ju, and X. Jiang, "Data-driven arbitrary polynomial chaos-based probabilistic load flow considering correlated uncertainties," *IEEE Transactions on Power Systems*, vol. 34, no. 4, pp. 3274-3276, Jul. 2019.

[88] J. Laowanitwattana and S. Uatrongjit, "Probabilistic power flow analysis based on partial least square and arbitrary polynomial chaos expansion," *IEEE Transactions on Power Systems*, vol. 37, no. 2, pp. 1461-1470, Mar. 2022.

[89] F. Ni, P. H. Nguyen, and J. F. G. Cobben, "Basis-adaptive sparse polynomial chaos expansion for probabilistic power flow," *IEEE Transactions on Power*

Systems, vol. 32, no. 1, pp. 694-704, Jan. 2017.

[90] Y. Xu, L. Mili, and J. Zhao, "Probabilistic power flow calculation and variance analysis based on hierarchical adaptive polynomial chaos-anova method," *IEEE Transactions on Power Systems*, vol. 34, no. 5, pp. 3316-3325, Sept. 2019.

[91] D. Shen, H. Wu, B. Xia, and D. Gan, "Arbitrarily sparse polynomial chaos expansion for high-dimensional parametric problems: Parametric and probabilistic power flow as an example," *IEEE Systems Journal*, vol. 16, no. 3, pp. 4950-4961, Sept. 2022.

[92] S. Ly, P. Pareek, and H. D. Nguyen, "Scalable probabilistic optimal power flow for high renewables using lite polynomial chaos expansion," *IEEE Systems Journal*, vol. 17, no. 2, pp. 2282-2293, Jun. 2023.

[93] Z. Ren, W. Li, R. Billinton, and W. Yan, "Probabilistic power flow analysis based on the stochastic response surface method," *IEEE Transactions on Power Systems*, vol. 31, no. 3, pp. 2307-2315, May 2016.

[94] Y. Xu, M. Korkali, L. Mili, X. Chen, and L. Min, "Risk assessment of rare events in probabilistic power flow via hybrid multi-surrogate method," *IEEE Transactions on Smart Grid*, vol. 11, no. 2, pp. 1593-1603, Mar. 2020.

[95] T. Mühlpfordt, T. Faulwasser, and V. Hagenmeyer, "Solving stochastic AC power flow via polynomial chaos expansion," in *IEEE Conference on Control Applications* Buenos Aires, Argentina, 2016, pp. 70-76.

[96] T. Mühlpfordt, T. Faulwasser, L. Roald, and V. Hagenmeyer, "Solving optimal power flow with non-Gaussian uncertainties via polynomial chaos expansion," in *Annual Conference on Decision and Control*, Melbourne, VIC, Australia, 2017, pp. 4490-4496.

[97] Y. Xu, L. Mili, A. Sandu, M. R. v. Spakovsky, and J. Zhao, "Propagating uncertainty in power system dynamic simulations using polynomial chaos," *IEEE Transactions on Power Systems*, vol. 34, no. 1, pp. 338-348, Jan. 2019.

[98] K. Ye, J. Zhao, N. Duan, and D. A. Maldonado, "Stochastic power system dynamic simulation and stability assessment considering dynamics from

correlated loads and PVs," *IEEE Transactions on Industry Applications*, vol. 58, no. 6, pp. 7764-7775, Nov./Dec. 2022.

[99] Y. Qiu, J. Lin, X. Chen, F. Liu, and Y. Song, "Nonintrusive uncertainty quantification of dynamic power systems subject to stochastic excitations," *IEEE Transactions on Power Systems*, vol. 36, no. 1, pp. 402-414, Jan. 2021.

[100] K. Konakli and B. Sudret, "Polynomial meta-models with canonical low-rank approximations: Numerical insights and comparison to sparse polynomial chaos expansions," *Journal of Computational Physics*, vol. 321, pp. 1144-1169, Sept. 2016.

[101] H. Sheng and X. Wang, "Probabilistic power flow calculation using non-intrusive low-rank approximation method," *IEEE Transactions on Power Systems*, vol. 34, no. 4, pp. 3014-3025, Jul. 2019.

[102] Y. Jiang, T. H. Ortmeyer, M. Fan, and X. Ai, "Data-driven low-rank tensor approximation for fast grid integration of commercial EV charging stations considering demand uncertainties," *IEEE Transactions on Smart Grid*, vol. 14, no. 1, pp. 517-529, Jan. 2023.

[103] K. Ye, J. Zhao, N. Duan, and Y. Zhang, "Physics-informed sparse Gaussian process for probabilistic stability analysis of large-scale power system with dynamic PVs and loads," *IEEE Transactions on Power Systems*, vol. 38, no. 3, pp. 2868-2879, Jul. 2023.

[104] Q. Chen, N. Lin, S. Bu, H. Wang, and B. Zhang, "Interpretable time-adaptive transient stability assessment based on dual-stage attention mechanism," *IEEE Transactions on Power Systems*, vol. 38, no. 3, pp. 2776-2790, May 2023.

[105] Q. Chen, S. Bu, H. Wang, and C. Lei, "Real-time multi-stability risk assessment and visualization of power systems: A graph neural network-based method," *IEEE Transactions on Power Systems*, pp. 1-14, 2024, Early access.

[106] G. Lu and S. Bu, "Advanced probabilistic transient stability assessment for operational planning: A physics-informed graphical learning approach," *IEEE Transactions on Power Systems*, vol. 40, no. 1, pp. 740-752, Jan. 2025.

[107] G. Lu and S. Bu, “Online dynamic security assessment: Using hybrid physics-guided deep learning models,” *IEEE Transactions on Industrial Informatics*, vol. 20, no. 11, pp. 13190-13200, Nov. 2024.

[108] F. B. Alhasawi and J. V. Milanovic, “Ranking the importance of synchronous generators for renewable energy integration,” *IEEE Transactions on Power Systems*, vol. 27, no. 1, pp. 416-423, Jun. 2012.

[109] X. Xu, Z. Yan, M. Shahidehpour, H. Wang, and S. Chen, “Power system voltage stability evaluation considering renewable energy with correlated variabilities,” *IEEE Transactions on Power Systems*, vol. 33, no. 3, pp. 3236-3245, May 2018.

[110] K. Ye, J. Zhao, F. Ding, R. Yang, X. Chen, and G. W. Dobbins, “Global sensitivity analysis of large distribution system with PVs using deep Gaussian process,” *IEEE Transactions on Power Systems*, vol. 36, no. 5, pp. 4888-4891, Sept. 2021.

[111] K. Ye, J. Zhao, C. Huang, N. Duan, Y. Zhang, and T. E. Field, “A data-driven global sensitivity analysis framework for three-phase distribution system with PVs,” *IEEE Transactions on Power Systems*, vol. 36, no. 5, pp. 4809-4819, Sept. 2021.

[112] B. Yuan, M. Zhou, G. Li, and X. P. Zhang, “Stochastic small-signal stability of power systems with wind power generation,” *IEEE Transactions on Power Systems*, vol. 30, no. 4, pp. 1680-1689, Sept. 2015.

[113] C. Chen, X. Zhang, M. Cui, K. Zhang, J. Zhao, and F. Li, “Stability assessment of secondary frequency control system with dynamic false data injection attacks,” *IEEE Transactions on Industrial Informatics*, vol. 18, no. 5, pp. 3224-3234, May 2022.

[114] F. M. Mele, R. Zárate-Miñano, and F. Milano, “Modeling load stochastic jumps for power systems dynamic analysis,” *IEEE Transactions on Power Systems*, vol. 34, no. 6, pp. 5087-5090, Nov. 2019.

[115] M. Adeen and F. Milano, “On the impact of auto-correlation of stochastic processes on the transient behavior of power systems,” *IEEE Transactions on*

Power Systems, vol. 36, no. 5, pp. 4832-4835, Sept. 2021.

[116] F. Milano and R. Zárate-Miñano, “A systematic method to model power systems as stochastic differential algebraic equations,” *IEEE Transactions on Power Systems*, vol. 28, no. 4, pp. 4537-4544, Nov. 2013.

[117] G. Ghanavati, P. D. H. Hines, and T. I. Lakoba, “Identifying useful statistical indicators of proximity to instability in stochastic power systems,” *IEEE Transactions on Power Systems*, vol. 31, no. 2, pp. 1360-1368, Mar. 2016.

[118] C. O. Nwankpa and S. M. Shahidehpour, “Stochastic model for power system planning studies,” *IEE Proceedings C (Generation, Transmission and Distribution)*, vol. 138, no. 4, Jul. 1991.

[119] X. Wang, H. D. Chiang, J. Wang, H. Liu, and T. Wang, “Long-term stability analysis of power systems with wind power based on stochastic differential equations: Model development and foundations,” *IEEE Transactions on Sustainable Energy*, vol. 6, no. 4, pp. 1534-1542, Oct. 2015.

[120] H. Mohammed and C. O. Nwankpa, “Stochastic analysis and simulation of grid-connected wind energy conversion system,” *IEEE Transactions on Energy Conversion*, vol. 15, no. 1, pp. 85-90, Mar. 2000.

[121] Y. Qin, H. Hua, and J. Cao, “Stochastic optimal control scheme for battery lifetime extension in islanded microgrid via a novel modeling approach,” *IEEE Transactions on Smart Grid*, vol. 10, no. 4, pp. 4467-4475, Jul. 2019.

[122] X. Chen, J. Lin, F. Liu, and Y. Song, “Optimal control of ders in adn under spatial and temporal correlated uncertainties,” *IEEE Transactions on Smart Grid*, vol. 11, no. 2, pp. 1216-1228, Mar. 2020.

[123] Y. Qiu, J. Lin, F. Liu, Y. Song, G. Chen, and L. Ding, “Stochastic online generation control of cascaded run-of-the-river hydropower for mitigating solar power volatility,” *IEEE Transactions on Power Systems*, vol. 35, no. 6, pp. 4709-4722, Nov. 2020.

[124] N. Yu and B. Foggo, “Stochastic valuation of energy storage in wholesale power markets,” *Energy Economics*, vol. 64, pp. 177-185, May 2017.

[125] Z. Y. Dong, J. H. Zhao, and D. J. Hill, “Numerical simulation for stochastic transient stability assessment,” *IEEE Transactions on Power Systems*, vol. 27, no. 4, pp. 1741-1749, Nov. 2012.

[126] G. M. Jónsdóttir, M. A. A. Murad, and F. Milano, “On the initialization of transient stability models of power systems with the inclusion of stochastic processes,” *IEEE Transactions on Power Systems*, vol. 35, no. 5, pp. 4112-4115, Sept. 2020.

[127] H. Li, P. Ju, C. Gan, S. You, F. Wu, and Y. Liu, “Analytic analysis for dynamic system frequency in power systems under uncertain variability,” *IEEE Transactions on Power Systems*, vol. 34, no. 2, pp. 982-993, Mar. 2019.

[128] Y. Li, Y. Gu, and T. C. Green, “Revisiting grid-forming and grid-following inverters: A duality theory,” *IEEE Transactions on Power Systems*, vol. 37, no. 6, pp. 4541-4554, Nov. 2022.

[129] F. Zhou, “Drive-train torsional vibration suppression of large scale PMSG-based WECS,” *Protection and Control of Modern Power Systems*, vol. 7, no. 1, p. 37, Sept. 2022.

[130] C. Huang, F. Li, and Z. Jin, “Maximum power point tracking strategy for large-scale wind generation systems considering wind turbine dynamics,” *IEEE Transactions on Industrial Electronics*, vol. 62, no. 4, pp. 2530-2539, Apr. 2015.

[131] P. M. Anderson and M. Mirheydar, “A low-order system frequency response model,” *IEEE transactions on power systems*, vol. 5, no. 3, pp. 720-729, Aug. 1990.

[132] Q. Shi, F. Li, and H. Cui, “Analytical method to aggregate multi-machine SFR model with applications in power system dynamic studies,” *IEEE Transactions on Power Systems*, vol. 33, no. 6, pp. 6355-6367, Nov. 2018.

[133] Z. Cheng, S. Hu, D. Yue, C. Dou, S. J. I. T. o. S. Shen, Man,, and C. Systems, “Resilient distributed coordination control of multiarea power systems under hybrid attacks,” *IEEE Transactions on Systems, Man, Cybernetics: Systems*, vol. 52, no. 1, pp. 7-18, Jan. 2021.

[134] Z. Zhang, E. Du, F. Teng, N. Zhang, and C. J. I. T. o. P. S. Kang, “Modeling frequency dynamics in unit commitment with a high share of renewable energy,” *IEEE Transactions on Power Systems*, vol. 35, no. 6, pp. 4383-4395, Nov. 2020.

[135] D. G. Castelain, L. O. Seman, A. Péres, S. L. Bertoli, and S. V. G. Oliveira, “Explicit solution for transcendental equation in power electronics applications,” in *IEEE/IAS International Conference on Industry Applications*, Fortaleza, Brazil, 2012, pp. 1-4.

[136] J. Dai, Y. Tang, and Y. Wang, “Aggregation frequency response modeling for wind farms with frequency support capabilities,” in *IEEE Power & Energy Society General Meeting*, Atlanta, GA, USA, 2019, pp. 1-5.

[137] Y. Yang, W. Wu, B. Wang, and M. J. I. T. o. P. S. Li, “Analytical reformulation for stochastic unit commitment considering wind power uncertainty with Gaussian mixture model,” *IEEE Transactions on Power Systems*, vol. 35, no. 4, pp. 2769-2782, Jul. 2019.

[138] B. Pal and B. Chaudhuri, “Test system model,” in *Robust control in power systems*, Cham, Switzerland: Springer, 2005, pp. 40-41.

[139] DTU Data, *Urbulence and turbine measurements from the Nordtank turbine*, 2025, Feb. 22. [Online]. Available: https://data.dtu.dk/articles/dataset/Turbulence_and_turbine_measurements_from_the_Nordtank_turbine/16782598?backTo=/collections/Wind_Turbine_load_measurements/5405406

[140] National Electricity Transmission System (NETS), *Security and quality of supply standard (SQSS)*, 2025, Feb. 22. [Online]. Available: https://www.nationalgrideso.com/industry-information/codes/security-and-quality-supply-standard-sqss

[141] G. Blatman and B. Sudret, “Adaptive sparse polynomial chaos expansion based on least angle regression,” *Journal of Computational Physics*, vol. 230, no. 6, pp. 2345-2367, Mar. 2011.

[142] W. Weng, P. A. Taylor, and J. L. Walmsley, “Guidelines for airflow over

complex terrain: Model developments," *Journal of Wind Engineering and Industrial Aerodynamics*, vol. 86, no. 2, pp. 169-186, Jun. 2000.

[143] P. Kundur, "Control of active power and reactive power," in *Power system stability and control*, New York, NY, USA: McGraw-Hill, 1994, pp. 581-626.

[144] M. A. Alvarez, L. Rosasco, and N. D. Lawrence, "Kernels for vector-valued functions: A review," *Foundations Trends in Machine Learning*, vol. 4, no. 3, pp. 195-266, Jun. 2012.

[145] J. H. Eto et al., "Use of frequency response metrics to assess the planning and operating requirements for reliable integration of variable renewable generation," Tech. Rep. LBNL-4142E, 2010.

[146] DTU Wind, *Pywake 2.5.0: An open-source wind farm simulation tool*, 2025, Feb. 22. [Online]. Available: https://gitlab.windenergy.dtu.dk/TOPFARM/PyWake

[147] G. Mosetti, C. Poloni, and B. Diviacco, "Optimization of wind turbine positioning in large windfarms by means of a genetic algorithm," *Journal of Wind Engineering and Industrial Aerodynamics*, vol. 51, no. 1, pp. 105-116, Jan. 1994.

[148] A. Hyvärinen and E. Oja, "Independent component analysis: Algorithms and applications," *Neural Networks*, vol. 13, no. 4, pp. 411-430, Jun. 2000.

[149] X. Xing et al., "Independent component analysis (ICA) based method for estimating the deformation of highways in permafrost region (HPICA)—a case study of maduo section of gongyu highway," *IEEE Journal of Selected Topics in Applied Earth Observations and Remote Sensing*, vol. 17, pp. 970-984, Dec. 2024.

[150] A. Akrami and H. Mohsenian-Rad, "Event-triggered distribution system state estimation: Sparse Kalman filtering with reinforced coupling," *IEEE Transactions on Smart Grid*, vol. 15, no. 1, pp. 627-640, Apr. 2024.

[151] Neon Neue Energieökonomik, Technical University of Berlin, ETH Zürich, DIW Berlin, *OPSD data packages*, 2025, Feb. 22. [Online]. Available:

https://open-power-system-data.org/

[152] H. Yuan, R. S. Biswas, J. Tan, and Y. Zhang, “Developing a reduced 240-bus WECC dynamic model for frequency response study of high renewable integration,” in *IEEE/PES Transmission and Distribution Conference and Exposition*, Chicago, IL, USA, 2020, pp. 1-5.

[153] California ISO, *Managing the evolving grid*, 2025, Feb. 22. [Online]. Available: https://www.caiso.com/about/our-business/managing-the-evolving-grid

[154] A. Papoulis and S. U. Pillai, “Spectral representation,” in *Probability random variables and stochastic processes*, 4th ed. New York, NY, USA: McGraw-Hill, 2002, pp. 509-513.

[155] K. K. Phoon, S. P. Huang, and S. T. Quek, “Simulation of second-order processes using Karhunen–Loeve expansion,” *Computers & Structures*, vol. 80, no. 12, pp. 1049-1060, May 2002.

[156] D. Xiu and G. E. Karniadakis, “Modeling uncertainty in flow simulations via generalized polynomial chaos,” *Journal of Computational Physics*, vol. 187, no. 1, pp. 137-167, May 2003.

[157] D. C. Montgomery, “The 2k factorial design,” in *Design and analysis of experiments*, 8th ed. Hoboken, NJ, USA: John Wiley & Sons, Inc., 2012, pp. 255-268.

[158] B. Efron, T. Hastie, L. Johnstone, and R. Tibshirani, “Least angle regression,” *The Annals of Statistics*, vol. 32, no. 2, pp. 407-499, Apr. 2004.

[159] S. Kucherenko, S. Tarantola, and P. Annoni, “Estimation of global sensitivity indices for models with dependent variables,” *Computer Physics Communications*, vol. 183, no. 4, pp. 937-946, Apr. 2012.

[160] I. M. Sobol′, "Global sensitivity indices for nonlinear mathematical models and their Monte Carlo estimates," *Mathematics and Computers in Simulation*, vol. 55, no. 1, pp. 271-280, Feb. 2001.